UNIVERSITY OF NAPLES FEDERICO II

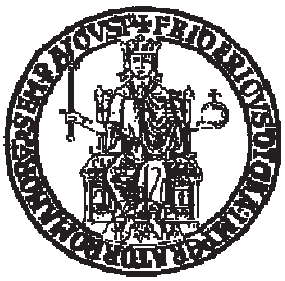

D.I.I. – DEPARTMENT OF INDUSTRIAL ENGINEERING

PH.D. DISSERTATION

DOCTORAL PROGRAM IN INDUSTRIAL ENGINEERING

XXXI Cycle

MULTI-PHYSICAL MODELLING AND PROTOTYPING OF AN ENERGY HARVESTING SYSTEM INTEGRATED IN A RAILWAY PNEUMATIC SUSPENSION

PH.D. CANDIDATE

ING. ANDREA GENOVESE

SUPERVISOR

PROF. ING. MICHELE RUSSO

CO-SUPERVISOR

PROF. ING. MARIO TERZO

REVIEWER

PROF. ING STEFANO BRUNI
(POLITECNICO DI MILANO)

PROF. ING MASSIMO SORLI
(POLITECNICO DI TORINO)

“Se sapessimo (esattamente) quel che stiamo facendo,

non si chiamerebbe ricerca.”

Albert Einstein

Abstract

The aim of this PhD thesis is the investigation of an energy harvesting system to be integrated in a railway pneumatic spring to recovery otherwise wasted energy source from suspension vibration. Exploiting the piezoelectric effect to convert the mechanical energy into an electrical one, the final scope consists on the use of this system to power supply one or more sensors that can give useful information for the monitoring and the diagnostics of vehicle or its subsystems.

Starting from the analysis of the energy sources, a multi-physical approach to the study of an energy harvesting system is proposed to take into account all physics involved in the phenomenon, to make the most of the otherwise wasted energy and to develop a suitable and affordable tool for the design.

The project of the energy harvesting device embedded in a railway pneumatic spring has been carried out by means of using a finite element technique and multi-physics modelling activity. The possibility to combine two energy extraction processes was investigated with the purpose of making the most of the characteristics of the system and maximize the energy recovering.

Exploiting commercial piezoelectric transducers, an experimental activity was conducted in two steps. A first mock-up was built and tested on a shaker to develop the device and to tune the numerical model against experimental evidence. In the second step a full-scale prototype of an air spring for metro application with the EH system was realized. In order to test the full-scale component, the design of a new test bench was carried out. Finally, the Air spring integrated with the EH device was tested and models validated.

Table of contents

Table of contents

List of figures

List of Tables

Notation

Symbol	Description	Unit
a	plate radius	[m]
AC	Auxiliary chamber	
A_e	Effective area	[m^2]
b	critical pressure ratio	[-]
BC	Bellow chamber	
C	Viscous damping coefficient	[Ns/m]
C_p	piezoelectric output capacitance	
D	sonic conductance	
DOF	Degree of freedom	
e	Orifice effective area	[m^2]
EH	Energy harvesitng	
F	force	[N]
f	frequency	[Hz]
FD	Flexible diaphragm	
G	Mass flow rate	[Kg/s]
i	current	[A]
IoT	Internet of Things	
K	stiffness	[N/m]
k	polytropic exponent	
M	mass	[Kg]
m	Air mass	[Kg]
MEMS	Micro Electro-Mechanical Systems	
NDE	Non-Destructive Evaluation	
P	Pressure	[Pa]
R	universal gas constant	[J/kgK]
R_L	Resistive load	
S	mechanical strain	[-]
SHM	Structural Health Monitoring	
T	temperature	[K]
t	time	[s]
V	volume	[m^3]
V_p	Piezoelectric voltage	[V]
V_T	Voltage generate by the transducer	[V]
W	power	[W]
WSNs	wireless sensor networks	
z_1	Absolute displacement of air spring lower plate	[m]
z_2	Absolute displacement of air spring upper plate	[m]
z_3	Absolute displacement of flexible diaphragm centre	[m]
z_r	Relative displacement of FD centre respect to air spring lower plate	[m]

Nomenclature

α, β and γ	electromechanical coupling coefficients of the transducer	
Γ	generalized electromechanical coupling factor	
ε	Mechanical elongation	[m]
ε_b	Elongation due to the bending	[m]
ε_t	Elongation due to the traction	[m]
ρ	density	[kg/m^3]
σ	mechanical stress	[Pa]
ω	radian frequency	[rad/s]
ξ	Damping ratio	

Subscripts	**Description**
0	Initial condition
ac	Auxiliary chamber
air	Air spring
atm	atmospheric
av	average
bc	Bellow chamber
bm	Base motion
el	electric
extr	extractable
FD	Flexible diaphragm
H	harvester
pl	Pressure load

Introduction

The activities described in this PhD thesis derive from the interest of *Applied Mechanics Research Group* of the *Department of Industrial Engineering* of *University of Naples Federico II* in starting a new research line in energy harvesting and its possible applications.

In the past decades, the research effort in energy harvesting from both academics and private sector has increased exponentially due to the plethora of possible applications. This increased interest is due to the convergence of different factors, with the most prominent being the enormous progress made in the field of semiconductors. It substantially reduced energy consumption and size of electronic devices leading to the invasion of Micro Electro-Mechanical Systems (MEMS). In turn, the development and widespread adoption of these low-powered systems led to the birth of the age of portable electronics, miniature sensors and actuators that have a wide range of applications. Portable devices, GPS system and biomedical devices are some of most known applications. In the industrial field, more specific use of these technologies regards Wireless Sensor Nodes (WSNs), Structural Health Monitoring (SHM), Non-Destructive Evaluation (NDE) and more recently the Internet of Things (IoT). These applications are based on the use of wireless self-powered sensors with the aim of measuring and transmitting extensive data for monitoring of objects or activities like industrial processes, structures, machines, vehicles, environment, healthcare and traffic.

In this context, the work presented here concerns a multi-physical approach to the study of an energy harvesting system. The focus is on exploiting otherwise wasted energy source of a specific environment to power supply a sensor. In particular, following the personal research background in railway [1]–[7], we propose an energy harvesting system to be integrated in a railway pneumatic spring that exploits the piezoelectric effect to convert the mechanical energy into an electrical one. The final vision is to create an autonomous and smart air spring capable of collecting information for the monitoring and diagnostics of the vehicle or its subsystems: to achieve this goal we designed this system, coupled with sensors, to be self-powered. The study presented in this thesis is based on the idea of harvesting energy by exploitation of existing components. The innovative vision is the integration of a generator, electronic and sensing system in the existing space available in the components, avoiding wire cablings.

Nowadays, the railway industry is moving forward at a fast pace and railway vehicles have changed from being an essentially mechanical system to one that increasingly

includes electronics, computer processing and sensors. These technologies play a fundamental role in train management, communication, monitoring and control for vehicle dynamics, leading to improvement in terms of safety, performance, comfort and reducing life-cycle cost.

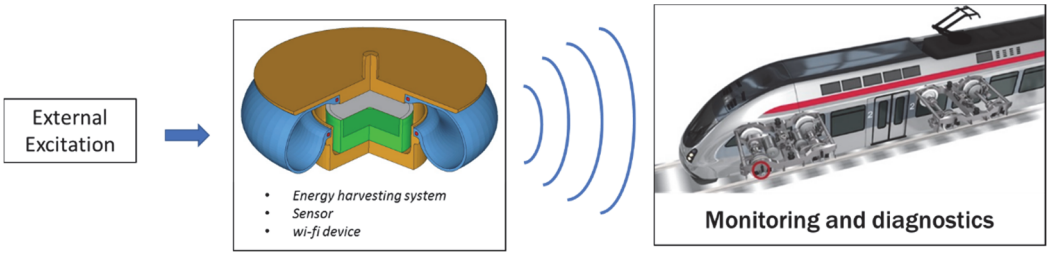

Figure 0.1 Illustration of vision of the research activity

The first step was to study the extended scenario related to the energy harvesting, analysing the different strategies and focusing to the kinetic energy harvesting techniques. This phase of study, descripted in the Chapter 1, motived the choice of a multi-physical approach.

In the Chapter 2 the railway system is analysed in the prospective of energy harvesting. After a brief a description of the railway system, the requirement of these system, which make this field of application particularly suitable for the energy harvesting, are pointed out. Then a literature review of the energy harvesting technologies targeted for railway systems is presented. The analysis of the source and mechanism of excitations, necessary for the device design, is then presented also by resorting to parametric mathematical models of vehicle dynamics.

The device layout integrated in the pneumatic spring is presented in Chapter 3 alongside a detailing of the system hardware and an explanation of the operation principle. To better understand the idea, first a pneumatic suspension system is analysed in details and an overview on the air spring modelling approach is presented, focussing on the multi-physics techniques.

Chapter 4 and 5 are dedicated to the modelling of energy harvesting devices integrated in the railway pneumatic spring. We propose an integrated modelling approach to accurately describe the phenomena building on the concept that the dynamic of the harvester is strictly influenced by the air spring type and working condition and, vice versa, the presence of the harvesting system modifies the geometry of the bellow. In particular, we first present in the 4th chapter a finite element model that was developed to preliminary study the dynamic behaviour of the assembly. Then in the 5th chapter we move to a multi-physical model adopting a strongly coupled approach that establishes

the assembly of different domains contributions into one set of coupled equations to be solved in the same environment by the same integrator.

In Chapter 6 the experimental activities are described. The piezoelectric energy harvesting system integrated in an air spring was designed, prototyped and experimentally tested. These activities were conducted in two steps. In the first one a mock-up was prototyped and tested on a shaker, considering just the base motion excitation mechanism. In the second step a full-scale prototype of an air spring with the EH system was built, a new test designed and several tests were carried out.

Finally, are summarised the outcomes of the thesis and future developments.

Chapter 1

Energy harvesting: a multi-physical approach

This chapter is intended to give the reader a brief and general view of the energy harvesting scenario, with a focus on the kinetic energy harvesting brand. It gives a comparison between the main energy sources and techniques for harvesting and a general review of the possible power conversion mechanisms. We then focus on motion-based energy harvesting, where the energy flow, the possible sources and comparison of the main transduction mechanism are analysed. Finally, the used approach to the topic is motivated.

1.1 Energy harvesting: definition and motivation

Many definitions can be found in literature under the header 'energy harvesting', one of the most common defines energy harvesting, or energy scavenging, as the recovery of energy from freely available environmental resources. Building on this definition, some consideration can be made. Referring to the amount of obtainable energy we speak about different EH scales. Strictly speaking, macro-scale EH technologies in the form of windmills, watermills and passive solar power systems have been around for centuries. Nowadays, with the global energy crisis and environmental concerns, many technologies have advanced considerably to include devices in large EH scale. The solar, wind, geothermal and hydraulic power plants or farms are such examples [8]. These are usually referred to as renewable energy devices and are fundamental in the effort to face the environmental and pollution issues. Vibration, given its ubiquitousness, has also became a good alternative energy source, it can be found almost everywhere: floors and walls, vehicles, jet engine housings, human motion, etc. It has received increasing attention in recent years for macro scale. These macro-scale harvesting technologies might differ

from each other in many ways but they all share the same task of feeding the power grid distribution system, alternatively or complementary to traditional sources.

Nevertheless, most of the current research activities on EH are focused on the small-scale, from the μW to the W, so much that in the literature, where not differently specified, the terms EH refers to the energy recovery from freely available environmental resources at that scale. This is due to different factors, with the most prominent one being the enormous progress made in the field of semiconductor in the past decades. It substantially reduced energy consumption and size of electronic devices leading to the invasion of Micro Electro-Mechanical Systems (MEMS).

The development of these low-power systems has revolutionized the market (figure 1.1) giving birth to the age of portable electronics, miniature sensors and actuators that have a wide range of applications ranging from portable mobiles and GPS system to more specific ones such as Wireless Sensor Nodes (WSNs), Structural Health Monitoring (SHM), Non-Destructive Evaluation (NDE) and Internet of Things (IoT).

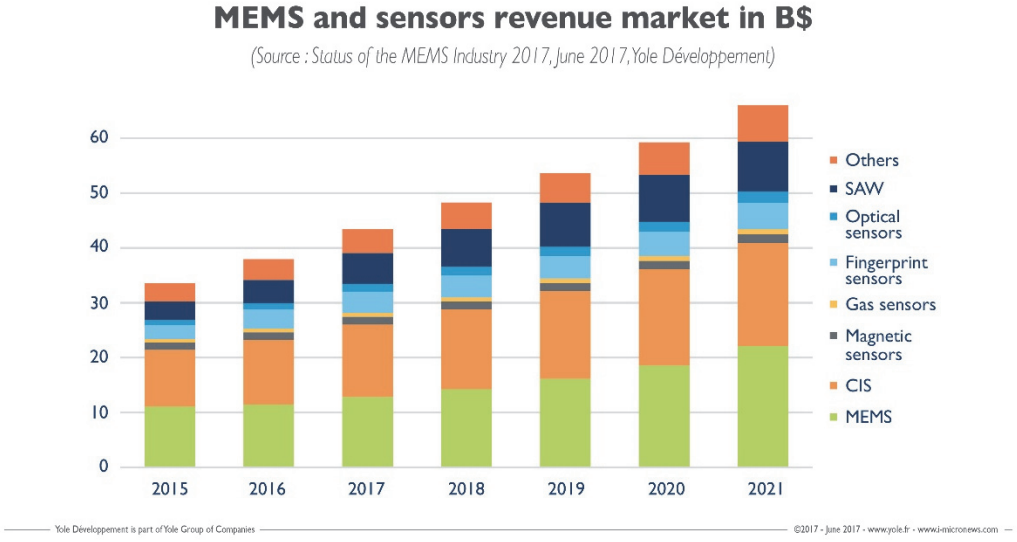

Figure 1.1 Mems and sensor market and forecast [9].

In many of these applications the microsystem is completely embedded in the structure, it has the need to be wireless with no physical connection to the outside world. The main issue with this is that a wireless device requires its own power supply. The traditional solution for power supply is the use batteries that have be included in the design of such devices. However, batteries present some undesirable aspects: they have a limited

lifespan, a limited amount of energy, tend to be quite bulky, present maintenance costs and contain chemicals whose disposal is problematics.

For example, consider a battery powered wireless sensor deployed in a remote and hostile environment: once the stored energy in the battery has been exhausted, to replace the power supply the device must be physically recovered, implying often a great inconvenience and significant costs [10]–[12].

The introduction of Low and Ultra-Low-Power electronics has led to a large reduction in consumption of wireless sensors [13]: the typical power need of mobile devices ranges between hundreds of milliwatts for MP3s, mobile phones and GPS applications to few micro-watts for wristwatches, RFID, MEMS sensors and actuators. Considering that usually these devices are in a sleep state up to 99.9% of their operation time, waking up only to transmit data for few milliseconds, their average power consumption is below 10µW. In order to compare energy demand and supply, a lithium battery can provide 30µW/cc for 1 year or 30mW/cc for just 10 hours, while a vibration-driven generator could last for at least 50 years with the same power level [14]. On this way the EH is a complementary or alternative solution to batteries, it offers a method for their autonomous recharging and in some situations even their elimination. Thus, these small-scale generators have turned harvesting into a small but growing contributor to the world's energy needs. This technology offers two main advantages over battery-powered solutions: virtually inexhaustible sources and little or no adverse environmental effects. Furthermore, the energy is recovered form otherwise waste sources or from sources that are not significantly influenced by this process.

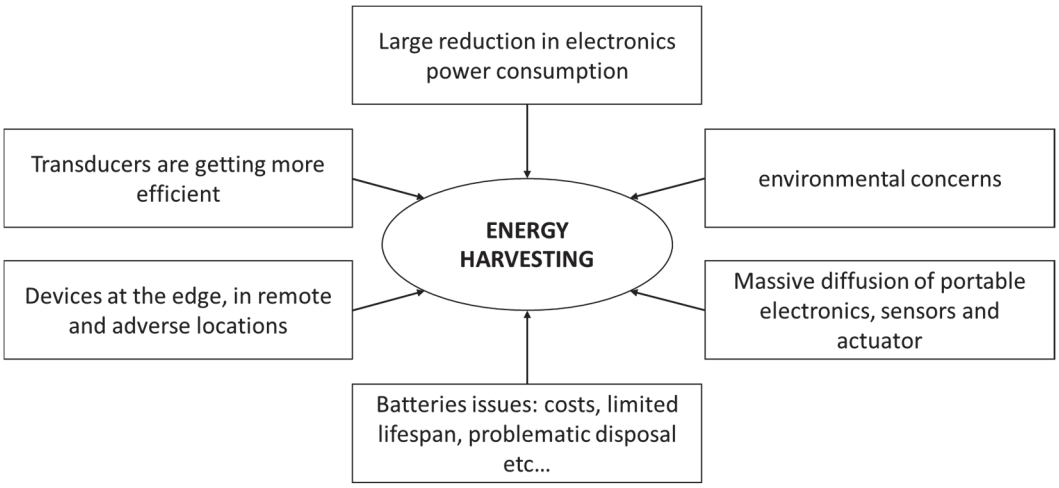

Figure 1.2 Motivations that push the interest to the energy harvesting

These motivations have led to an increasing research effort in energy harvesting (EH) from both academics and industrialist over the years as evident from the rising number of publications and product prototype, since the end of 90s to date (figure 1.2). In the figure 1.3 are reported the documents by year that use the term “energy harvesting” in the keywords or in the title, collected in the databases Scopus and Web of Science.

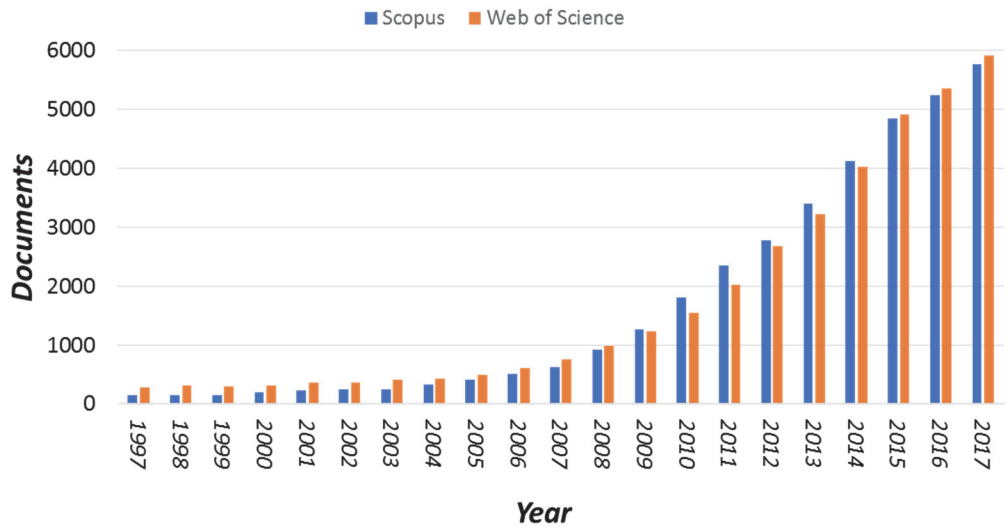

Figure 1.3 Documents whit Energy harvesting keywords in Scopus database over the years

1.2 Energy harvesting sources and techniques

The term EH, according to the definition given above, is ordinarily used to indicate the process of the extraction and conversion of otherwise wasted energy, available in the ambient, into electrical energy. The application scale is typically small and is linked to the supply of low-power electronic devices.

An EH system is composed by a *transducer,* that converts energy from one type to another, usually electricity, and by a target electronics that consumes or stores this energy. The target device can be driven synchronously, using the recovered energy directly, or asynchronously, recharging temporary storage systems such as capacitors or batteries. In any case the device that uses the energy needs to be designed to work with energy harvesting as the power source.

Starting with the concept of *ubiquitous energy*: the energy is everywhere in the environment that surrounds us and is present in different forms. These kinds of energies

are potential sources for the EH process by exploiting appropriate phenomena and materials. These sources have the great advantage of being essentially free and of not having pollution attributable to the conversion mechanisms.

EH systems classification can be made either by conversion methods or by sources.

There are five main methods for energy harvesting: piezoelectric, thermoelectric, photovoltaic, electromagnetic and electrostatic.

It is possible to classify EH sources in different ways. A first classification considers who or what provides the energy for conversion. In this classification scheme Mateu and Moll [15] distinguish two kinds of devices: devices that use part of the energy of the user of the electronic appliance and devices that get their energy from the environment. The user of first kind of devices is usually a human, but it could also be an animal: thus these devices are called Human Energy devices. The second kind of EH devices get their energy from the environment, and thus they are called Environment Energy devices.

Another possible classification is based on the type of EH sources. According to Harb [16] and Thomas et al. [17] we can identify the following categories for small-scale EH:

- Thermal: Thermal gradient and temperature fluctuation over the time.
- Photonic: solar and light for indoor and outdoor.
- Pressure gradient.
- Micro water flow.
- Electromagnetic waves or radio frequency (RF).
- Biological.
- Kinetic: motion, vibration or mechanical energy.

Furthermore, in recent works chemical sources are also considered [18], [19]. In literature many classifications consider only mechanical, thermal, and solar energy as main sources, while pressure gradient and water flow are included in the kinetic/mechanical sources and biological and electromagnetic are not yet widely used. Here, the focus is on the kinetic EH thus the state-of-the-art of the other principal EH techniques is only briefly outlined in order to better understand the research field and compare the main results. For an exhaustive and comprehensive framework on EH techniques, in addition to the review of Harb [16] and Thomas et al. [17], you may refer to the documents of Fan et al. [20], Tang et al. [21], Ahmed et al. [22], Mathúna et al.[23], Chalasani et al.[24] , Paradiso and Starner [25], [26], Gilbert and Balouchi [27], Wei and Jing [28].

Several properties can be considered to characterize energy suppliers and compare different possible solutions. Fry et al in [29] provide a comprehensive list of these properties that includes: physical properties such as the size, shape and weight; electrical

properties like power density, maximum voltage and current; environmental properties as water resistance and operating temperature range; and operational and maintenance properties. For most EH applications, like that of portable devices, required properties are small dimensions, limited weights and, consequently, adequate power density. The power density is defined as the amount of power that can be produced per volume or sectional area of the device and is generally expressed in $\mu W/cm^3$ or $\mu W/cm^2$. This parameter is very important for portable devices as it states the minimum device volume that is required to harvest the amount of power needed, indeed results less fundamental in integrated systems that exploit dimensions already available in the existing components as well as the one conceived in this work. In any case, the impact that the harvesting produces on the subject environment must be evaluated and if necessary taken into account. In table 1.1 are reported the typical values of power generation capability for some EH techniques.

Table 1.1 Typical data for various energy harvesting techniques [24].

Energy harvesting method	Conditions	Power density
Vibration	1 m/s^2	100 $\mu W/cm^3$
Solar	Outdoors	7500 $\mu W/cm^2$
Solar	Indoors	100 $\mu W/cm^2$
Thermal	5°C temperature gradient	60 $\mu W/cm^2$

1.2.1 Thermal energy harvesting

The main way in which thermal energy is harvested is exploiting temperature gradients. The phenomenon of creating electric potential with a temperature difference and vice-versa in known as thermoelectricity. The thermoelectric EH is based on the Seedbeck effect, which is the conversion of heat directly into electric energy by means of thermocouples. A simple construct of a thermocouple is shown in figure 1.4, consisting of two pillars made of a thermoelement (generally alternating n-type and p-type semiconductors) connected in series by a metallic conducting strip.

In situations where thermoelectric generators are used for energy harvesting, many thermocouples will be connected electrically in series and thermally in parallel. The effectiveness of these conversions is limited by the Carnot efficiency.

The Carnot equation for the maximum theoretical efficiency is:

$$\eta_{Carnot} = \frac{T_h - T_c}{T_c} \quad (1.1)$$

Where T_h and T_c are respectively the absolute temperature of the hot and cold side of the device. From this equation is clear that the greater the temperature gradient, the larger the conversion efficiency. In [17] is pointed out that the small conversion efficiency for modest temperature gradient is 3% at ΔT=10°C; 14% at ΔT =50°C; only 40% at ΔT = 200°C. Many of these largescale devices exist, for example, for the generation of electricity from hot exhausts on vehicles. At a smaller scale, the main interest has been in the generation of power from body heat, to power wearable devices. Considering the thermal gradient between the human body, 37 °C, and a typical environment temperature, 20 °C, Paradiso et al. evaluate a conversion efficiency of 5.5% [26]. Another wearable thermoelectric device that exploit a temperature difference of 15 °C between human skin and the surrounding environment, was proposed by Kim et al. [30]. It can generate a voltage output of 3mV.

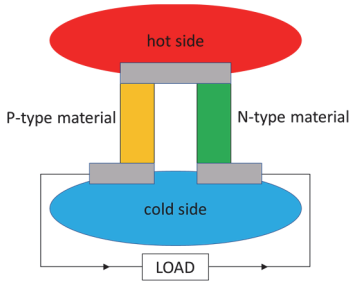

Figure 1.4 Seedbeck based thermal energy harvesting scheme.

Despite thermoelectric generators are considered to have long life, low maintenance and high reliability, their diffusion is limited because of their low energy conversion efficiency for small temperature gradients and high costs [31].

Higher temperature differences may be achievable in other environments, e.g. heaters in a building, geothermal steam (80–180°C), solar ponds (~75°C), waste heat generated by power plants (15°C) and industrial waste heat sources (75°C).

Besides the thermoelectric process there are several ways to exploit the thermal gradient: thermionic, thermomagnetism, ferroelectricity and the Nernst effect [32]. At present, the thermoelectric conversion results the most effective of these processes.

A different concept for thermal EH is based on the temperature fluctuation over time. In this case is exploited the pyroelectric materials property of showing spontaneous electrical polarization as function of temperature. It follows that temperature time fluctuation causes induced charge variations and consequently current [33]. Materials used in pyroelectric devices include piezoelectric materials such as PZT (lead zirconate

titanate) and PVDF (polyvinylidene fluoride). Nowadays, the main commercial application for pyroelectricity is for sensors in thermal imaging cameras, but many other studies for energy harvesting based on this phenomenon can be found in literature.

1.2.2 Photonic energy harvesting

Photonic EH, also known as solar and light EH, exploits the photovoltaic phenomenon that consists in the conversion of light energy into electrical energy by means of appropriate materials. The form of energy exploited is typically light energy obtained from solar radiation that delivers approximately 124PW (PW= 10^{15} Watts) globally to the surface of the Earth [33]. However, the power available from the energy conversion in the solar cells, varies widely depending on several factors. Indoors or outdoors location, sunny or cloudy day, geographical location, distance between the sun and the Earth are some of the variables which can influence the radiation/illumination level (e.g. indoors or outdoors, sunny or cloudy day) [34], [35]. Approximately 1000 W/m^2 of solar power is incident on surfaces directly facing the sun on a bright sunny day. A solar cell can be depicted as reported in figure 1.5. It is composed by a semiconductor diode with a large p–n junction in the plane of the cell that is positioned close to the top surface. When the cell is exposed to photonic radiation, an electric potential develops between the p- and n-type materials.

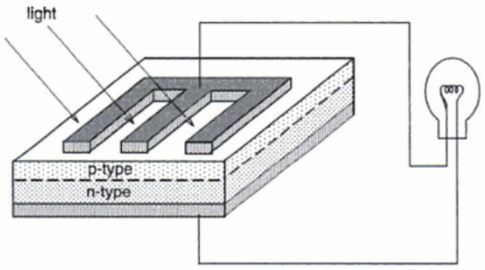

Figure 1.5 A typical solar cell scheme [36].

The most common photovoltaic cells are the silicon-based cells: single crystal, polycrystal, ribbon and sheet, and thin-layer forms. These present an efficiency range from 10% to 23 % in a state-of-art cell and a good price to performance ratio. Commercial solar conversion efficiencies of 30% or more exploit other solar technologies that include the high efficiency multi-junction devices, which stack different photovoltaic cells on top of each other to maximize the capture of incident radiation, and thin film solar cells. Experimental devices can reach about 35%.

For wireless sensor nodes application Thomas et al. [17] assume the power density of 75 $\mu W/mm^2$ for outdoor solar cell operation and a power density of 1 μW/mm2 for indoor operation.

1.2.3 Electromagnetic energy harvesting

Base stations, wireless internet, mobile phones, satellite communication, radio, TV's, digital multimedia broadcasting and X-rays are some of the electromagnetic radiation source, also known as radio frequency, RF, radiation. One must not confuse between electromagnetic energy source and electromagnetic transducer. In some articles, electromagnetic generator is used for electromagnetic transducer [16]. The energy associated with electromagnetic radiation can be collected for use by an appropriately designed antenna that converts it into an alternating electric current [37]. The key units of an RF power harvesting system are the antenna and the rectifier circuit that allows the RF power or alternating current to be converted into direct current energy [38].

As described in [39], the amount of received power is a function of the following: the wavelength, the transmitted power, the gain of both the transmitting and the receiving antenna and the distance between source and harvester. This last parameter is a key factor that mainly influence the power losses and so the harvestable energy as the transmitted power quadratic decrease with it. Other losses occur in the internal circuitry of the harvester. Considering the normal sources of radiation like standard transmitter or alternate current cables, the harvested power is usually quantifiable in less than 1μW [26].

Nishimoto et al. [39] propose a low-cost approach using RF energy harvesting from ambient RF fields; this approach relies mainly on TV broadcast signals. TV broadcast signals that are not received by TV viewers are generally dissipated as heat resulting in a waste of energy. This wasted energy can be utilized to power a low-power sensor node. Other applications of wireless charging with regard to near-field and far-field practices to better illustrate the diverse and promising use of this techniques are reported in [40]. This article provides a comprehensive survey of the emerging wireless charging systems and their fundamental technologies, international standards as well as applications in wireless communication networks.

1.2.4 Kinetic energy harvesting

The kinetic energy harvesting can be defined as the recovery and conversion of mechanical energy into electrical one. The general opinion from the literature is that while each application should be evaluated individually with regards to finding the best energy-harvesting method, kinetic energy in the form of motion or vibration is generally the most versatile and ubiquitous ambient energy source available [41].

Kinetic EH schematization and energy flow.

The recovery and conversion process of mechanical sources and consequent electrical energy consumption or storage occurs through a complex system called energy harvesting. According to Manca, in his PhD thesis [42], this system performs three main functions: energy *extraction*, energy *conversion* and *energy transfer/management*. Following this energy flow, the kinetic EH system can be schematically considered composed of three main parts/domains in which the functions are carried out. Firstly, there is the *mechanical part*, often-named energy *harvester*, designated to extract the energy from the environment to make it usable for the conversion. The second part consists in the *transduction mechanism*, or the *transducer*, that converts the extracted mechanical energy into electrical one by exploiting a physical phenomenon of electromechanical coupling. Finally, the *electrical part* is tasked with managing and transferring energy to the electric load. Figure 1.6 shows the kinetic EH system general schematization and the main energy flows that cross it.

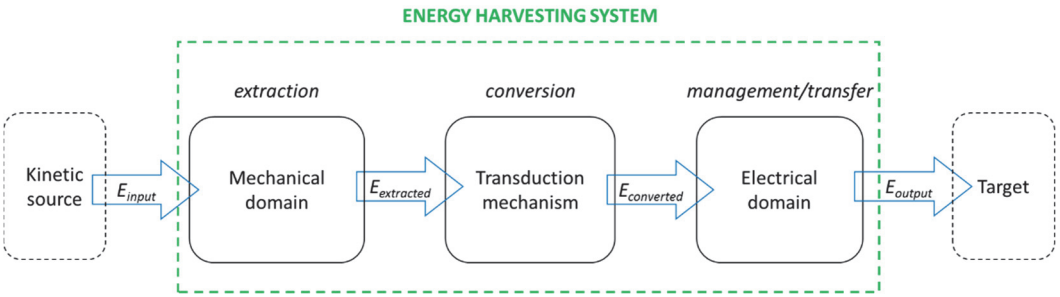

Figure 1.6 Kinetic EH system: Scheme and main energy flows.

Here it should be emphasized that even if the overall energy flow through the system is from the mechanical domain, which represent the EH system input, to the electrical one, which is the output, a backward energy flow is present and must be considered. Indeed, by means of the transducer, the two domains are coupled and while the mechanical energy is transferred toward the electrical domain, the electrical energy is transferred

backward to the mechanical domain. Generally, this backward flow does not have any effect on the source since the harvestable energy is negligible with respect to the source itself. Nevertheless, this domains coupling influences the dynamics of the harvester and thus the amount of energy that can be extracted from the environment. This is the reason why for the analysis of the EH system and for its design related to a specific application, both domains must be considered together.

Kinetic EH sources

The mechanical energy source that has to be extracted by the system may assume different forms. A useful classification has been provided by Gilbert and Balouch [27]. They divided sources of mechanical energy in three main groups depending on the type of motion: sources in which the motion is essentially constant over extended periods of time; intermittent motion; and cyclic motion as in vibration sources

- The *Steady state mechanical sources* are the ones in which the motion is quasi-constant over time. This kind of source is typical of fluid flow as well as in wind, air current and water flow either in natural channels or through pipes. Fluid flow based EH is widespread on the macro scale for electrical power generation as in wind turbines and hydroelectric plants. Recently this source has also been investigated for smaller scale applications [43], [44]. Another form of continuous motion regards objects such as a rotating shaft.

- For *intermittent mechanical sources* is intended the energy available from motion which may be cyclic in nature but in which the energy is only available for a short part of the cycle. Energy sources like these are available during vehicles passage over opportune EH device or in human normal walking or running.

- The principal type of *cyclic sources* are *mechanical vibrations*. Among other harvestable energy sources such as solar, radio frequency RF, thermal and biochemical, kinetic energy in the form of mechanical vibrations is deemed to be the most attractive in the low-power electronic domain, this is because of its power density, versatility and abundance. The amount of extractable energy mainly depends on the amplitude of the vibration and its frequency. Furthermore, it can vary dependently on the impact the presence of EH device causes on the source.

  Low-level vibrations occur in many environments such as buildings, automobiles, aircraft, ships, trains, industrial environments, vibrating machineries and human beings. Being the nature of vibration very variable with the phenomenon that

generates them, the amplitude and dominant frequency can range in a wide spectrum. In table 1.2 are reported the measurements performed by Roundy et al. [45] for a number of vibration sources in terms of frequency and acceleration magnitude of the fundamental vibration mode.

Table 1.2 Acceleration magnitude and frequency of some vibration sources [45].

Vibration source	**A (m/s^2)**	**f_{peak}(Hz)**
Car engine compartment	12	200
Base of 3-axis machine tool	10	70
Blender casing	6.4	121
Clothes dryer	3.5	121
Person nervously tapping their heel	3	1
Car instrument panel	3	13
Door frame just after door closes	3	125
Small microwave oven	2.5	121
Windows next to a busy road	0.7	100
CD on notebook computer	0.6	75
Second story floor of busy office	0.2	100
Car engine compartment	12	200

A committee formed during the Second Annual Energy Harvesting Workshop held on January 30–31, 2007 in Fort Worth, TX, drew up a comprehensive list of potential vibration sources for energy harvesting. This committee, formed by members from academia, industry, and federal labs, had the purpose to create a first draft of Standard in vibration EH [46]. The vibration sources were classified both according to their elastic stiffness and according to the surrounding. In table 1.3, the vibration sources grouped by the surrounding are shown.

Table 1.3 Vibration sources exploitable for energy harvesting in the surrounding [46].

Human body	Vehicles	Structures	Industrial	Environment
Breathing, blood pressure, exhalation, body heat	Aircraft, UAV, helicopter, automobiles, trains	Bridges, roads, tunnels, farm house structures	Motors, compressors, chillers, pumps, fans	Wind
Walking, arm motion, finger motion, jogging, swimming, eating, talking	Tires, tracks, peddles, brakes, shock absorbers, turbines	Control-switch, HVAC systems, ducts, cleaners, etc.	Conveyors, cutting and dicing, vibrating mach.	Ocean currents, acoustic waves,

In this first draft, a categorization of acceleration and frequency is also provided. Acceleration can be categorized as low (less than 10 mg), mid (10 – 100 mg) and high (above 100 mg), where 1g = 9.8 m/s^2. In the same way, frequency can be categorized as low (less than 10Hz), mid (10 – 120 Hz) and high (above 120 Hz).

The knowledge about the vibration source is essential to the design of the harvester converter. In fact, given the specific application for which the device is targeted, usually it should be designed to resonate at the fundamental vibration frequency. Furthermore, during the feasibility study, the magnitude and the frequency of the driving vibration must be known to evaluate the potential power generation.

Kinetic EH transduction mechanism

Kinetic energy harvesting requires a transduction mechanism to generate electrical energy from motion and the generator needs a mechanical system that couples environmental displacements to the transduction mechanism. Electromechanical transduction is performed by the exploitation of peculiar proprieties of materials to couple mechanical and electrical behaviour. There are three basic transduction mechanisms by which vibrations can be converted into electrical energy: electromagnetic, electrostatic, and piezoelectric. Each transducer has strengths and weaknesses, thus a best overall technique does not exist. The optimal choice depends on the specific application and should be evaluated case by case.

- In the *electromagnetic* transduction, the relative motion between a coil and a permanent magnet causes a variation of the magnetic field. Thus, a current flow in the coil according to Faraday's low (figure 1.7a). The induced voltage across the coil depends upon the strength of the magnetic field, the velocity of the relative movement and the number of turns of the coil. This generator does not need any supplementary voltage source. Electromagnetic transduction has the advantage of high efficiency compared with other mechanisms when there are no size constraints applied. This advantage is largely contributed to the feasibility of designing the coil in such a way to achieve high coupling factors. On the other hand, its integration in microsystems has some limitations. The number of coil turns achievable in a microscale device is limited resulting in low output voltages.

- In the *electrostatic* transduction mechanism, the motion is linked to the plates (conductors) of a mechanically variable capacitor. The two conductors are separated by a dielectric move relative to one another and the energy stored in the capacitor changes. This induces current in a connected circuit and thus provides the mechanism for mechanical to electrical energy conversion (figure 1.7b). The primary disadvantage of electrostatic converters is that they require a separate voltage source to initiate the conversion process.

- *Piezoelectric* transducers are based on the piezoelectric effect that is the generation of an electric charge as a result of a force exerted on the material. Mechanical strain in a piezoelectric material causes a charge separation across the material (which is a dielectric). In other word, the material is polarized and this effect is called direct piezoelectric effect. This polarization generates an electric field that is used to perform the conversion of the mechanical energy, used in the material's deformation, into electrical energy [47].
  There are two common modes utilized for piezoelectric energy harvesting: 33-mode and 31-mode. In 33-mode, the direction of applied stress (force) and generated voltage is the same, while in 31-mode the stress is applied in axial direction but the voltage is obtained from perpendicular direction (figure 1.7c).

Anyway, whatever it is the transduction mechanism, because of the variable nature of kinetic sources in terms of frequency and intensity, the resulting AC voltage and current are not directly suitable for energy storage or direct supply. An electric interface is usually used for AC/DC voltage regulation and management.

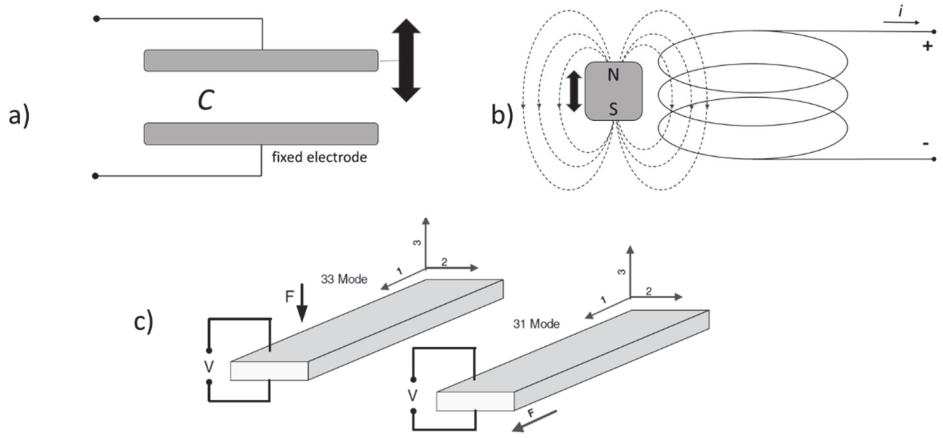

Figure 1.7 Kinetic energy harvesting transduction mechanism

Kinetic EH recent applications overview

A large number of researchers and industrialists are currently active in the field of kinetic energy harvesting, and a wide range of devices have been investigated and developed. Due to the versatility of motion-based harvesting, a wide range of applications is targeted for this kind of harvesters. The most successful ones focus on the implementation of wireless self-powered sensors networks for extensive monitoring activities like industrial process monitoring, machine health monitoring, environment monitoring, healthcare and medical applications and traffic control.

In literature, it is possible to find classifications of EH motion applications based on the transducer type, on whom or what is the source (human, vehicles, industrial machines, etc…), on the type of motion (vibration, impact, steady-state), and on the applications field [21], [28], [41]. Here an overview of recent application is provided.

Recently, many energy-harvesting applications have been referring to human motion since human motion is rich in kinetic energy. Feenstra et al. [48] and more recently Xie and Cai [49] developed backpack devices for harvesting part of human motion energy during walking. Using the human energy on the feet, with the aim of supplying a Bluetooth step-counter placed in the sole of a training shoe, a harvester for shoes application was proposed by Bonisoli et al. [50]. The system consists of a magneto-inductive transducer embedded with an electronic interface for power conditioning and exploits only the energy recovered by the impact on the ground. Energy recovery derives from the magnet-free oscillation following the shoe impact.

Other promising applications regard a vehicle travelling on an irregular road, both for harvesting vibrations of the chassis and from track-induced vibrations. Zuo et al. [51]

present a damper with an electromagnetic generator to replace the conventional damper. This device allows controlling the chassis vibration and generating a power output. Tornincasa et al. [52] proposed a vibration-powered wireless sensor node. The proposed device embeds a compact electromechanical wideband energy harvester optimized for tires.

On the track side, Jiang et al. have developed a compression-based roadway energy harvester that can be embedded into pavement to scavenge electrical energy from traffic-induced vibrations [53]. The proposed roadway harvester employs a group of piezoelectric harvesting units to convert traffic-induced vibrations into electrical energy.

Moreover, Kinetic EH energy harvesting has been investigated in other application fields such as aeronautic, ocean and railway. For example, Pearson et al. [54] applied a piezoelectric energy harvester into an aircraft for autonomous structural health monitoring systems.

Nowadays, on the buzz around the energy harvesting theme, several companies specializing in this field have emerged, making different kinetic energy harvesters available. Kinetron [55], Perpetuum Ltd. [56] and Ferro Solutions Inc. [57] are some of these companies.

1.3 Multi-physical approach

Given the overview reported in the previous sections, it is easy to understand that the study of energy harvesting systems is transversal and involves several disciplines. You refer to the ideal energy flow from the otherwise wasted energy (input) to the recovered one (output) in figure 1.8.

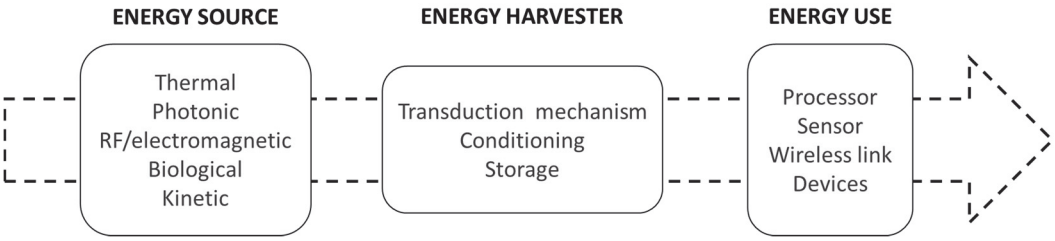

Figure 1.8 EH functional energy flow.

Starting from the harvestable energy source, an in-depth study is necessary to design the adequate device. This analysis can engage at least as many engineering areas as source

types, including mechanical, aerospace, electrical, and civil. Materials science, electrical circuitry and coupling mechanisms are subjects involved in the design and development of the harvester system. Finally, target load can be optimized to fit the harvest energy supply. Considering the motion-based energy harvesting, it encompasses mechanics, materials science, and electrical circuitry. Furthermore, to date EH devices that combine different sources are coming up. Researchers from all of these disciplines contribute heavily to the energy harvesting literature, often collaborating with each other.

On this way, it is quite clear that a multidisciplinary approach that include all physics involved (mechanics, thermodynamics, fluid dynamics, electronics etc.) is desirable. In a scenario in which there is a growing attention to EH technology, predictive models that includes and couples all these aspects can represent an ambitious goal to reach.

From the modelling point of view, it is needed to combine the modelling approaches from different domains to investigate the interaction between several parts of a device. The mechatronics systems, such as EH devices, are a clear example where the modelling activity involves the coupling of multibody dynamics with other domains such as electricity, fluid dynamics, pneumatics, control, etc.

As pointed out by Samin et al. in [58] and by Docquier in his PhD thesis [59], two main approaches can be individuated for multi-physics modelling: *strongly coupled* and *weakly coupled.* Strongly coupled techniques establish the assembling of different domains contributions into one set of coupled equations that is solved in the same environment by the same integrator. Here the coupling is performed when the model is built and the mathematical formulation is carried out by a unifying theory. On the contrary, the weakly coupled techniques implement the coupling in a subsequent step, at the simulation level by using special integration techniques such as the co-simulation. The equations of the different domains are solved separately, exchanging information at fixed time steps, possibly with iteration process to increase the numerical accuracy and stability.

Each approach presents pros and cons. For weakly coupled techniques, there is a good modularity allowing, in a relatively easy way, the addition or removal of the different domains. Moreover, it can take advantage of specific integrators dedicated to each discipline. The generation of one set of coupled equations, that characterize the strong coupling technique, gives a lighter and more portable solution beneficial to face the time simulation.

In this work, starting from the study of the energy sources, a multi-physical approach has been adopted. The methodology has been implemented for a railway application. The aim of this approach is to make the most of the otherwise wasted energy and to develop a suitable and affordable tool for the design.

Chapter 2

Application Field: Railway industry

In this chapter, the railway system is analysed in the prospective of energy harvesting. Firstly, a description of the railway system is briefly outlined. The focus is on the latest railway industry requirements that clarifies the choice of this application field for the proposed methodology. Then a literature review of the EH technologies targeted for railway systems is presented. In the third section, the source and mechanism of excitation are analysed in detail. Finally, a mathematical model of vehicle dynamics is presented.

2.1 Railway system overview

2.1.1 Railway system description

Railway is the most important form of transport worldwide. Railway basic working principle exploits the wheel/rail guidance based on the wheel profile conicity. The whole railway system can be considered as composed by two main industrial area: *rolling stock* (or *train*) and *infrastructure*. Those subsystems are strictly coupled and interconnected.

Railway *infrastructure* consists of the following items [60]:

- ground area;
- track and track bed;
- engineering structures such as bridges, etc.;
- level crossings;
- superstructure, in particular: rails, grooved rails and check rails, sleepers and longitudinal ties, small fittings for the permanent way, ballast including stone chippings and sand, points, crossings, etc.;
- access way for passengers and goods, including access by road;

- safety, signalling and telecommunications installations on the open track, in stations and in marshalling yards, including plants for generating, transforming and distributing electric current for signalling and telecommunications, buildings for such installations or plants, track brakes;
- lighting installations for traffic and safety purposes;
- plants for transforming and carrying electric power for train haulage: sub-stations, supply cables between substations and contact wires, catenaries and supports; third rail with supports;
- buildings used by the infrastructure department, including a proportion in respect of installations for the collection of transport charges.

Railway *trains* are often composed by a number of carriages that can transport either freight or passengers. Car design varies depending on the payload type, the train consist and rail route. The components constituting a vehicle can differ in function of the design and can include:

- car body;
- wagon frame (underframe);
- bogies;
- couplings;
- draft gear and brakes.

In some freight train configurations, the car body is carried just by two wheelsets, each composed of an axle and two wheels. For passenger trains, in most cases, each car body is mounted on two bogies (Figure 2.1). Another possible layout, although less frequent, considers a bogie shared by two car bodies. In turn, various bogies arrangements exist. Usually they are composed of the following main elements:

- the *frame*, which is the heaviest component of the bogie, especially if the motor and other fixed components are considered;
- the *wheelset* is an assembly that consists of two wheels fitted to an axle that ensure the guidance;
- the *central bowl,* that connects the car body to the bogie, allows relative rotations;
- The *suspension components* that are tasked with carrying static forces, vibration isolation and stability control.

Suspension of a rail vehicle can be performed in a single or multiple stage and it works in the horizontal plane and vertical directions. If suspension elements are directly connected to the wheels/axles they are called ‘primary’, otherwise ‘secondary’. Generally, in passenger and freight vehicles, the primary suspension systems connect wheel-axle sets with the bogie frame and act in the vertical direction, instead the

secondary suspension systems are located between the bogie frame and the car body. Most common suspension components include coil springs, friction-based components such as leaf springs, rubber springs, air springs and hydraulic dampers.

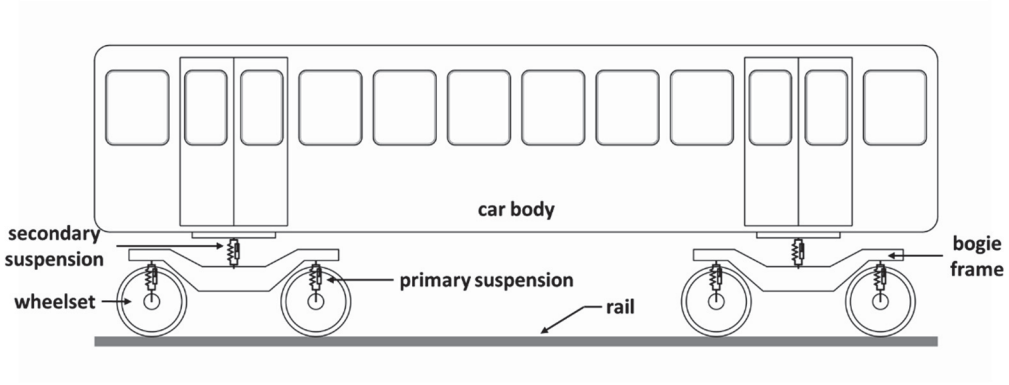

Figure 2.1 Train configuration

2.1.2 Railway systems condition monitoring

Soaring railways customer numbers worldwide and a shift to stricter regulations the railway industry focus has moved to improve capacity, punctuality, reliability and safety of the whole system. These challenges encourage the industry to invest in new technologies. Nowadays, the railway industry is moving forward at a fast pace and railway vehicles have changed from being an essentially mechanical system to one that increasingly includes electronics, computer processing and sensors [61]. These technologies play a fundamental role in train management, communication, monitoring and control for vehicle dynamics, leading improvement in terms of safety, performance, comfort and reducing life-cycle cost.

Safety is one of the most important attributes of railways compared with other means of transport. Modern technology allows to preserve, if not enhance, this characteristic i.e. reducing the cost of maintenance. Vehicle and track maintenance plans today are often based on traditional techniques. Scheduled preventive maintenance and parts replacement based on calendar, running time and distance are not always able to detect emerging faults (leading to unexpected damage) even if a simple visual inspection is included in the procedure. This method of maintenance can be quite expensive due to the replacement of working components prompted by obsolescence or distance limit, even though their real condition may allow them to run for longer. An important improvement in this field can be reached by changing from a calendar to a condition-based strategy or a combination of the two.

Modern railway vehicles provide sophisticated monitoring systems for data acquisition and processing both for rolling stock and infrastructure condition; they must be fitted with high-capacity communication buses and multiple sensors in order to allow advance processing for data collection and management. Roberts and Goodall [62], building on the concept that the railway is a complex, distributed, closely-coupled system, describe four different types of monitoring system: infrastructure-based infrastructure monitoring; rolling stock-based infrastructure monitoring; rolling stock-based rolling stock monitoring; and infrastructure-based rolling stock monitoring.

Nigigi et al. [63] provide a complete review of the modern techniques used for condition monitoring of railway vehicle dynamics. Reviewed solutions include both infrastructure-based and rolling stock-based techniques, referring to both model-based techniques (i.e. Kalman filter and sequential Monte Carlo method) and signal-based techniques (band-pass filter, spectral analysis, wavelet analysis and Fast Fourier Transform). Authors remark the importance of sensors as a starting point for practical applications of train dynamics condition monitoring. Signals can be carried out either through the employment of track-based sensors or vehicle-based sensors. Mostly, the track bed-based sensors are used to monitor wheelset condition, whereas, the rolling stock-based sensors are concerned with the monitoring of the rolling stock infrastructure. Figure 2.2 shows an appropriate sensor set for rolling stock (a) and for trackside (b).

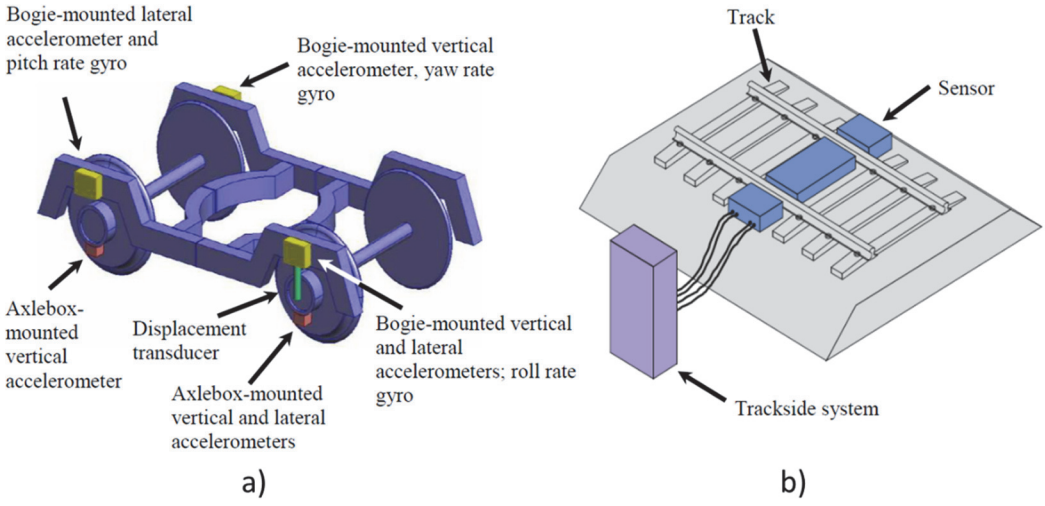

Figure 2.2 Illustration of typical sensor placement on vehicle a) and track b) [63].

Focusing on vehicle-based sensors, Ward et al. [64] study the opportunities related to condition monitoring of infrastructure and the rolling stock itself. The authors define an appropriate sensor set for use in-service vehicles that can be employed to identify certain

track defects, to monitor the running gear condition, and also to determine the absolute train speed. This list includes: axlebox-mounted vertical-and-lateral-sensing accelerometers, bogie-mounted vertical-and-lateral-sensing accelerometers, bogie-mounted pitch, roll and yow rate gyros, body-mounted lateral-sensing accelerometer, and primary suspension displacement sensor. Sensors must be placed in an appropriate location (figure 2.2a). The authors only consider inertial sensors due to their low cost and flexibility that are pushed in the last years by the developments of MEMS.

Every signal carried from the instruments can be used, on its own or with other signals, to obtain information on vehicle or track. For example, axlebox accelerometers can be used to measure shorter wavelength vertical irregularity.

From a practical point of view, whatever is the final goal of the sensors, on-board sensors and sensor networks imply the presence of wire cablings: firstly, to supply the electric power generated by the engine or stored in high-capacitance batteries; secondly to carry the signals from the field to the control room.

The proliferation of measurement points, especially on some outdoor components like the bogies, leads to an undesirable cabling architecture that often creates several operative problems in installation, reliability and maintenance. Furthermore, measurement instrumentations should be placed in a protected location in order to prevent false warning detection or disconnection.

Self-powered sensors could be a suitable solution to overcome this issue. In this context, EH generators coupled with wireless technology can be a viable option for railway applications.

2.2 Energy harvesting in Railway: literature review

Most kinetic EH applications in railway industry refer to the infrastructure-side of systems. Indeed, several researchers have concentrated their studies on the energy harvesting from train-induced track vibrations. Gatti et al. [65]. described a study to determine how much energy could be harvested from a passing train using a single-degree-of-freedom oscillator. Starting from the knowledge of the time history of vertical vibration measured on a sleeper, the authors determined the optimum mechanical parameters of a linear energy harvesting device. It should be tuned to a frequency at which the vertical acceleration is the greatest, and this corresponds to one of the train-load frequencies. By means of a numerical and experimental investigation, they found that the maximum energy that could be harvested per unit mass of the oscillator is about 0.25 J/kg at a frequency of about 17 Hz. Tianchen et al. [66] proposed a new generator

called drum transducer. The transducer, made of piezoelectric material, is positioned under the sleeper. It was able to recover and convert the sleeper vibration, induced by train passage (Figure 2.3), into electrical energy. Wang et al. proposed a different approach [67]. They designed an electromagnetic energy harvester to harness the vibrational power from railroad track deflections due to passing trains. Another transduction mechanism was proposed by Nelson et al. [68]. They attached a piezoelectric device on the bottom of the rail to exploit it bending. The power output of 1mW was generated from the longitudinal strain in the piezoelectric material produced by rail bending. More recently, a prototype for smart monitoring of underground rail transit by local energy generation was developed by Gao et al. [69]. A complete self-sustaining rail-mounted sensor node was proposed. The system included: an electromagnetic energy generator with DC-DC boost converter, a rail-based wireless sensor node with embedded accelerometers and temperature/humidity sensors and also a data processing algorithm.

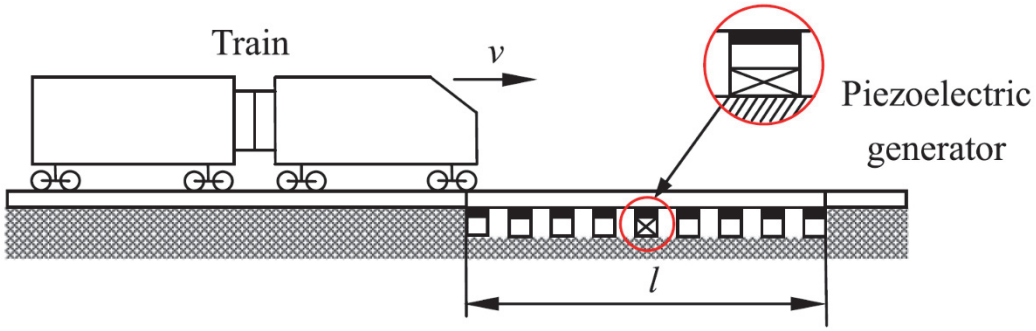

Figure 2.3 Track vibration energy harvesting by Tianchen et al. [66].

Looking at train-side a smaller number of EH device can be found respect to track-side. Socie and Barkan in the 2008 [70] proposed a smart sensor device with the scope of monitoring vehicle braking system. The completely smart system comprised three major subsystems: sensor, wireless network and energy harvester. A wireless transceiver, processor, analog electronics, and a sensing element composed the sensor part, which was attached to the brake beam (figure 2.4a). As energy supply, they used an internal battery that powered the system during normal operation and was recharged from an external EH device when the railcar was in motion. They prototyped an electromagnetic transduction mechanism that consisted of small permanent magnets vibrating within a coil to produce a current (figure 2.4b). This study greatest limitation is that the harvester device was designed lacking information on the spectrum of vibration environments encountered in service.

Figure 2.4 Smart system for monitoring rail breaking system [70]: Sensor mounted on break beam a) and prototype of energy harvester b).

De Pasquale et al. [71] proposed a piezoelectric EH generator to power autonomous sensors for sensors network applications. This device included a harvester, a small accumulator, some inertial sensors for the self-powered data acquisition, and a radio frequency transceiver. The sensing system was used to address structural monitoring of critical components such as bogies. Transduction mechanism is designated to convert the vehicle vibration into suitable electrical energy. A piezoelectric cantilever beam configuration was adopted exploiting the 31-working mode. In figure 2.5 is reported the harvester prototype.

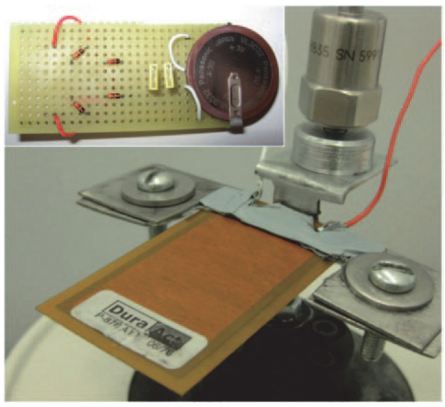

Figure 2.5 Cantilever beam harvester prototype by De Pasquale et al. [71].

The dynamic response of the cantilever was tuned to make the resonance frequency of the device coincide with the driving frequency of the excitation force. The dynamic behaviour was varied both by introducing a variable proof mass on the tip and by

increasing its structural stiffness with additional adhesive layers. The excitation frequency has been preliminarily determined by detecting lateral accelerations. The dominant excitation frequency of 5.5 Hz was obtained by the fast Fourier transformation on the acceleration signal.

The same research group also adopt an electromagnetic strategy to harvest energy from freight train vibrations [72]. Once again, the authors start from the study of input vibration source of the train through numerical simulation. Thus, the harvester was designed to fit the input vibration spectrum of the vehicle. The transduction mechanism is based on a movable permanent magnet that oscillates inside a cylindrical copper coil in the vertical direction under the excitation of environmental vibrations. An interesting innovation is that the proof mass is connected to the frame by a magnetically levitated suspension instead of traditional elastic springs. The final device package is 150x 125x95 mm, and when the freight train velocity is 80 km/h the corresponding output power, installing the system on the coach, results of 100 mW. Figure 2.6 shown the schematic layout of the harvester (figure 2.6a) and its prototype (figure 2.6b).

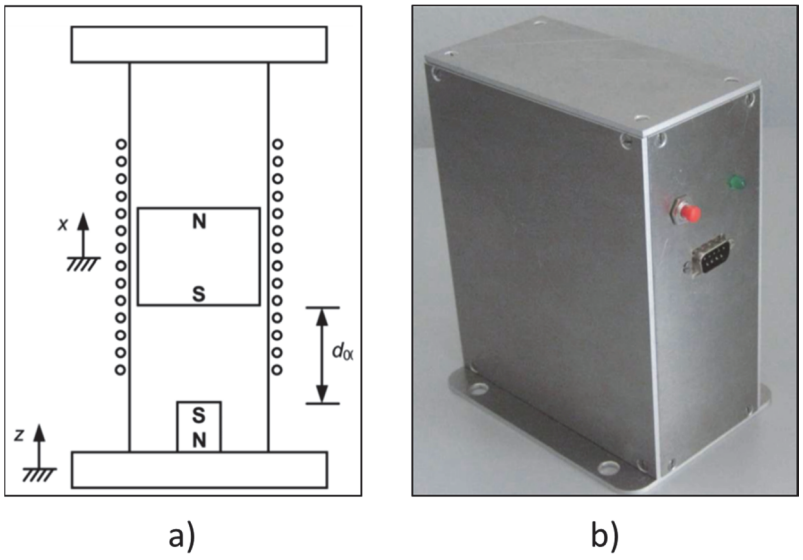

Figure 2.6 Freight train energy electromagnetic harvester [72]: schematic layout (a) and prototype (b).

A more recent publication by Bradai et al. [73] follow a similar approach. The EH device was designed for a freight train where electricity is not available in all carriages. It was targeted for a vibration profiles measured on a wagon of a train traveling between two German cities. Here the electromagnetic transducer is based on a moving coil attached to a mechanical spring unlike the previous work [72] where a magnetic suspension was

adopted. The system installed on the carriage was able to carry out an average voltage of 1.2 V peak to peak for an applied random excitation up to 1 mm of amplitude and for a frequency range from 20 to 40 Hz.

All the described applications and prototypes are finalised to fabricate a compact integrated platform, a sort of sand box, to install on the bogie or on the car body. These boxes are in addition to other components and systems and must find an appropriate place to be installed. In the context of a sensors network, the autonomous node must be properly optimized in dimensions, weights and packaging in order to have a negligible impact and no interferences with the main systems.

The study presented in this thesis is based on the idea of harvesting energy exploiting existing components. The innovative vision is the integration of a generator, electronic and sensing system in the existing space available in the components.

2.3 Excitation source analysis

2.3.1 Generalities

Railway vehicles employ steel wheels running on tracks with steel rails. The wheel/rail system provides the support, the guidance and the traction/braking functions. The interface between the two is established at contact point(s) between the wheels and rail surface, and both the vehicle configuration and the track greatly influence how vehicles behave [74]. The vehicle during the operations, in addition to the ride motion, presents other *parasitic movements* that consist in displacements and rotations along direction different from the riding one. We refer to the vehicle configuration reported in figure 2.7, consisting of one car body, two bogies, and four wheel-axles which are considered as rigid bodies. In the coordinate system showed in the figure and with velocity *v* that moves the vehicle, the parasitic movements are defined as follow:

- z - vertical motion (bouncing)
- y - lateral motion (lateral)
- x - longitudinal motion (longitudinal)
- ψ - yawing-noising
- ϕ - pitching
- θ - rolling

Furthermore, it is possible to define some combined movements, the most important are:

- z bouncing + ϕ pitching = galopping
- y lateral + ψ yawing = hunting
- y lateral + θ rolling = swaying

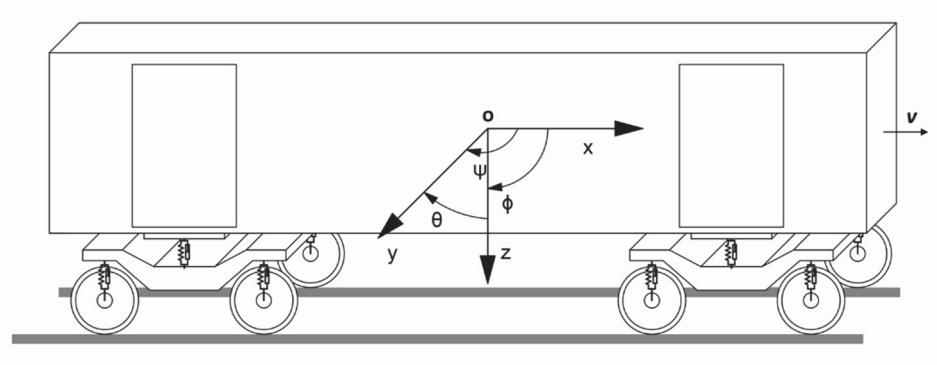

Figure 2.7 Rail vehicle dynamics coordinate system and nomenclature of motions.

These parasitic movements are a consequence of dynamic excitations. The main dynamic excitations, in addition to the weight that changes rather slowly and is therefore essentially a quasi-static problem, are caused by track/wheels interaction.

Tracks are in general neither straight nor perfectly even. In addition, wheels present some defects that can be accentuated by wear and tear. When a vehicle runs over the track with its irregularities, movements of the wheels and, thus, of the vehicle are induced. The dynamic system vehicle/track is excited to produce vibrations. The induced dynamic movements of the wheels are associated with accelerations of the vehicle bodies and forces inside the vehicle and between wheel and rail.

Zolotas and Goodall [75] divide the inputs from the track into two types: deterministic and random. *Deterministic inputs* can be subdivided in turns in isolated features such as steps, dips and short ramps; and intended inputs as gradients, curves that have well-defined characteristics. On the other hand, *random inputs* include irregularities and imperfections (roughness of track); characterised by a power spectrum (track velocity spectrum approximates to white noise).

In order to support the change in weight of the vehicle and to face the track inputs, trains are equipped with suspensions system. Suspensions have to provide guidance, so that the vehicle follows the intended path, and isolation to give a satisfactory ride quality. In the following chapters, we refer to a common configuration in which the wheelsets are

connected to the bogie via a primary suspension and the car body is supported by two bogies using softer secondary suspensions. The ‘stiff’ primary suspensions is generally needed for vehicle’s stability and guidance requirements, while the ‘soft’ secondary suspensions is designed to provide isolation from the track-induced vibrations and thus to ensure a good ride quality.

2.3.2 Vibrations induced by track unevenness

The frequency content of the vehicle vertical vibrations is fundamental to identify the highest energy levels in which the frequency range is, for a given vehicle and in function of vehicle velocity. The design of the generator must be conducted to tune its resonance frequency on this range and to harvest an energy amount as large as possible from different operating conditions.

The irregularity of the track generates some excitations on the wheel-axle set during train ride. Although filtered by the primary suspension systems, vibrations are transmitted to the bogie frame and then to the secondary suspensions. These operate another filtering action and the non-isolated part gets to the car body (Figure 2.8).

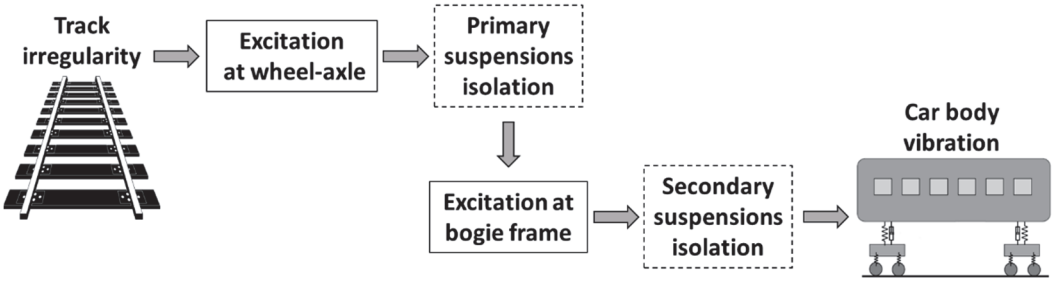

Figure 2.8 Schematic excitation flow induced by track irregularities.

Both experimental and simulation studies on train vibration induced by track irregularity can be found in literature. The main focus of these studies is passengers’ comfort. Indeed, the forces induced by the track can lead to a significant excitation not only of the car body motion as a rigid body, but also of its flexible vibration modes, especially on high speed trains [76]–[78].

Track irregularity is a random process with statistical regularity, which generates a broadband excitation. For this reason, the system response depends more on the vehicle’s dynamic characteristics than on the particular irregularity profile [79].

According to Dumitriu [80], focusing on vertical dynamics, some symmetrical and antisymmetrical movements are induced in railway vehicles from the track irregularities. We refer to the *y*-normal plane in figure 2.7, and define *axles plane* the plane identified by the two wheelset axles of a bogie. The irregularities of the rolling track transfer forces to the axles via wheel-track elastic contact. Thus, translation movements (bounce) and rotation (pitch) are generated in axles. For a two-bogie vehicle, the combination of these motions results into the symmetrical and antisymmetrical motion modes of the vehicle axles planes. Figure 2.9 shows the symmetrical (a) and antisymmetrical (b) bounce of the axles planes respectively.

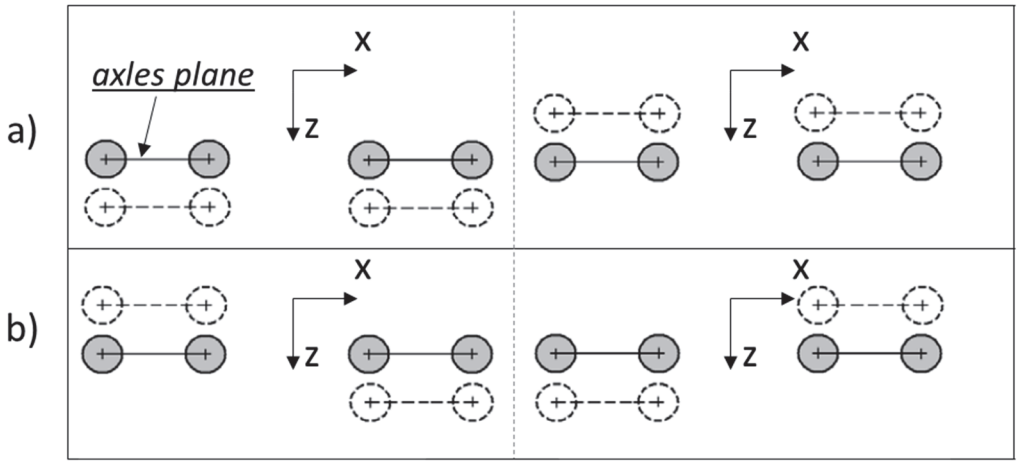

Figure 2.9 Symmetrical (a) and antisymmetrical (b) bounce of the axles planes.

Similarly, in figure 2.10 are reported the symmetrical (a) and antisymmetrical (b) pitch of the axles planes.

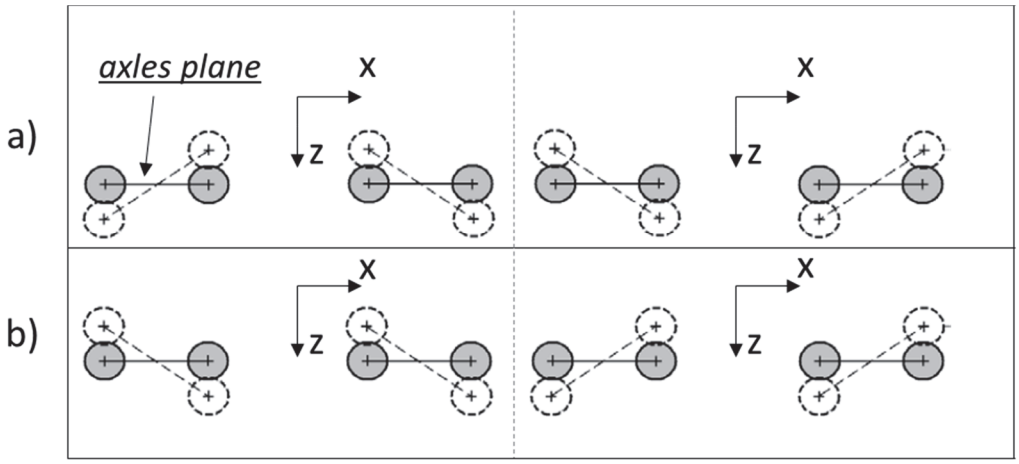

Figure 2.10 Symmetrical (a) and antisymmetrical (b) pitch of the axles planes.

These movements of the axles planes are transmitted to the suspended masses, via the suspension elements. In particular, motions of axles are imparted by the elements of the primary suspension to the bogies. The bogies are thus characterized by symmetrical and antisymmetrical vibration modes of both bouncing and pitching. These motions are in turn transmitted to the car body by means secondary suspensions. The car body will present the same type of symmetrical and antisymmetrical movements.

In our application, the interest is in the vertical dynamics of secondary suspensions. The focus is pointed on:

- Vibrations of the suspension ending attached to the bogie
- Relative motions between the secondary suspension endings in correspondence of the attachment points of car body and bogie.

The motivations of this focus will be detailed in the next chapter.

The study of rail vehicle vertical dynamics can be conducted experimentally or, more often because of costs, in simulations.

Experimental approach considers the installations of several sensors in such points of rolling stock components. Then, the acquired signals are usually elaborated to perform a frequency domain analysis. Signals, generally accelerations, can be treated by means of a Fourier Transform analysis or a Power Spectral Density analysis to study the vibration signal frequency content. Figures 2.11 shows an example of the vertical acceleration signal, measured at the middle of the car body floor of a high-speed train at about 210 km/h.

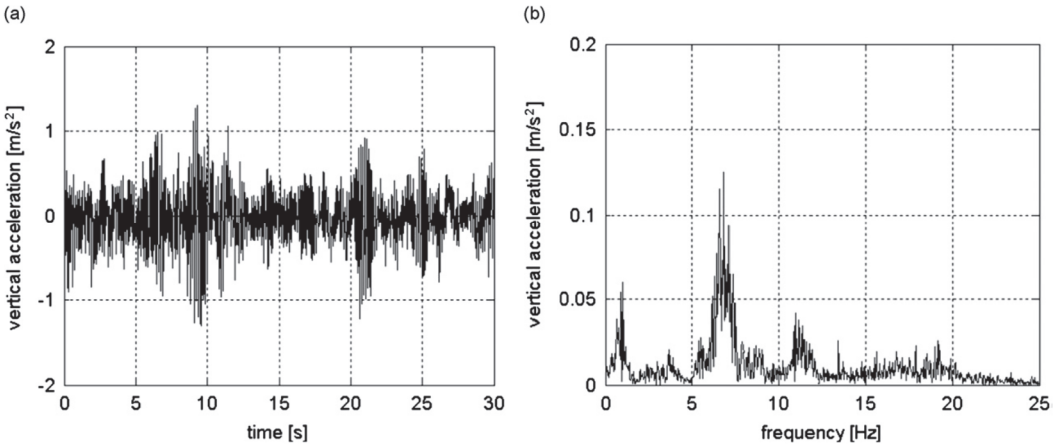

Figure 2.11 Example of the vertical acceleration measured on the car body floor of a high-speed train at about 210 km/h: time history (a) and corresponding Fourier transform (b) [79].

Here it should be noted that the measured data take into account both modes of rigid bodies and elastic modes, and are dependent on the sensors location. Zhai at al. [78] performed an experimental investigation on-track of the vibration characteristic of a China Railway High-speed at operational speed of 350 km/h. They installed: a car body acceleration sensor on the lower surface of car body floor, a bogie-frame acceleration sensor fixed on the top surface near the primary suspension, and an axle box acceleration sensor on the upper side of the axle box end cover. Authors found distinct dominant frequencies in the vertical vibration of the car body. The first main frequency was near 1 Hz, which represents the natural vibration frequency of the car body's vertical suspension. The second main frequency was about 10 Hz, close to the first-order natural vibration frequency of the car body vertical bending. The bogie vertical vibration acceleration varied within the range of ±2.5 g. In the frequency domain, the vibration energy distributed mainly in the range of 15–35 Hz which contained the low-order elastic modal frequencies of the bogie frame. Another recent on-track measurements were provided by Aravanis et al. [81]. The study was focused on railway vertical random vibration analysis in normal operating conditions. Vibration acceleration measurements were acquired using sensors installed on: car body, bogie frame, axle bearing and primary suspension of an Athens Metro vehicle. The prominent resonant frequencies in the range 0-100Hz estimated by bogie frame sensor were 11.5 Hz, 36.2 Hz and 67.5 Hz.

Also considering analysis by model simulation, most of the studies on rail vehicle vertical dynamics are focused on ride comfort and, so, on car body vibrations. For this reason, infrequently they give detailed information on bogie dynamics and the models include often the flexible car body behaviour. Zhou et al. [76] investigated the influences of car body vertical flexibility on the evaluation of ride quality. In this work the rigid modes

characteristic of the bogie, using parameters a typical high-speed passenger vehicle, result of 5.95 Hz for bounce and 10.9 Hz for pitch. For the car body they calculated 0.86 Hz for bouncing and 1.04 for pitching. In [82] the influence of bogie bounce frequency and vertical ride quality for different velocity was investigated. Dumitriu in [83] examines the dynamic response of a two-bogie vehicle derived from the track vertical irregularities. She founds for a typical passenger vehicle the following natural frequencies: 1.17 for car body bounce, 8.20 Hz for car body bending, 6.61 Hz for bogie bounce and 9.63 for bogie pitch.

The frequencies excitation for a train vary as a function of the type of vehicle and bodies/suspensions design. Nevertheless, some typical frequencies range can be identified. For bogies, frequencies excitation for rigid vertical modes (pitch and bounce) can range from 5 to 15 Hz. Referring to the car body, identifiable ranges are 0.5-2 Hz for rigid modes and 6-14 Hz for first bending flexible mode.

In order to determinate the dynamical behaviour of the secondary suspension the flexible modes of car body and bogie can be neglected. The attached points of secondary suspension with car body and bogie are slightly affected by the flexibility of these bodies. For this reason, a model that take into account only rigid bodies motions has been considered adequate for the scope of this work. A parametric model of the vehicle vertical dynamics is presented in the next section.

2.4 Railway vehicle modelling

The irregularity of the track generates excitations at wheel-axle set during train ride. Vibrations are transmitted to the bogie frame by the primary suspension systems. These movements are in turn imparted on the car body, although filtered by the secondary suspensions. As reported in previous sections, the interest is on the vertical movements of the link-points of secondary suspensions with bogie and car body in order to design the EH system. To evaluate these movements, two parametric models of the rail vehicle vertical dynamics have been created. At first, the problem is investigated through a simple two-degree-of-freedom (DOF) analytical model, often called a quarter vehicle model. Then a complete nine-DOF model that take into account also the pitch and roll motions of the bodies is presented.

2.4.1 Two-degree-of-freedom model, a quarter of vehicle

Before coming to a more detailed schematisation, a simple two-DOF analytical model is presented (Figure 2.12).

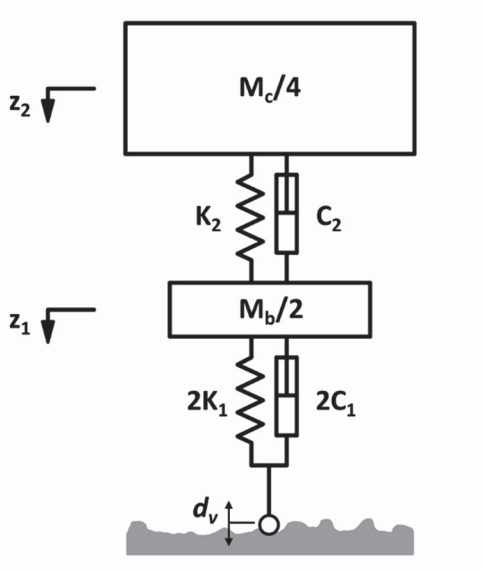

Figure 2.12 Two-degree-of-freedom rail vehicle model.

Although extremely simplified, this model has the same fundamental features of that presented in section 2.4.2. It allows to easily dive into details in the analysis of the problem and to understand the car body and bogie vibration modes excitation mechanism due to track unevenness.

The model is representative of a quarter of railway vehicle. It consists of two masses, $M_c/4$ representing the quarter car body mass and $M_b/2$ representing the bogie half mass. Each mass has a single vertical DOF, z_1 for bogie mass and z_2 for car body. The two mass are connected by an elastic element K_2 and damping system C_2 representing the secondary suspension. The wheel is considered in perfect contact with the track and is connected to the half-mass of the bogie via the primary suspension system ($2K_1$ and $2C_1$). Indicating with d_v the vertical displacements of the wheel imposed by track irregularities, the equations of motions are:

$$\frac{M_c}{4}\ddot{z}_2 + C_2(\dot{z}_2 - \dot{z}_1) + K_2(z_2 - z_1) = 0 \qquad (2.1)$$

$$\frac{M_b}{4}\ddot{z}_1 + C_2(\dot{z}_1 - \dot{z}_2) + K_2(z_1 - z_2) + 2C_1\left(\dot{z}_1 - \dot{d}\right) + 2K_1(z_1 - d) = 0 \qquad (2.2)$$

Form equations 2.1 and 2.2, considering $C_1 = C_2 = 0$, the two natural frequencies (rad/s) of the system can be calculated analytically as follow [84]:

$$\omega_{1,2}^2 = \frac{1}{2}\left[\frac{2K_1+K_2}{M_b/2} + \frac{K_2}{M_c/4} \pm \sqrt{\left(\frac{2K_1+K_2}{\frac{M_b}{2}} - \frac{K_2}{\frac{M_c}{4}}\right)^2 + \frac{4{K_2}^2}{M_c/4 \cdot M_b/2}}\right] \quad (2.3)$$

At these natural frequencies correspond two different vibration modes of the system.

In table 2.1 are summarize the parameters assumed for the dynamic analysis.

Table 2.1 Vehicle parameters for two-degree-of-freedom dynamic analysis

Parameter	Description	value	
M_c	Car body mass	30000	Kg
M_b	bogie mass	2500	Kg
K_1	Stiffness of primary suspension	1100000	N/m
K_2	Stiffness of primary suspension	600000	N/m
C_1	Damping coefficient of primary suspension	13000	N s/m
C_2	Damping coefficient of secondary suspension	12500	N s/m

Referring to such data the two natural frequencies are ω_1= 1.2 Hz and ω_1= 7.9 Hz. These are the bounce frequency of the car body and the bogie respectively.

We consider now a sinusoidal excitation:

$$d_v(t) = D_v \sin \Omega t \quad (2.4)$$

The free oscillation of the system is neglected by the presence of damping. The steady-state response of the forced system is:

$$z_1(t) = Z_1 \sin(\Omega t + \varphi_1) \quad (2.5)$$

$$z_2(t) = Z_2 \sin(\Omega t + \varphi_2) \quad (2.6)$$

Where Z_1 and Z_2 are the motions amplitudes, φ_1 and φ_2 are the phase angles.

In the figures 2.13 and 2.14 are reported the time-domain response of the system (in steady-state condition) for 1.2 Hz and 7.9 Hz sinusoidal input respectively. In both case the amplitude of the excitation is 1 cm.

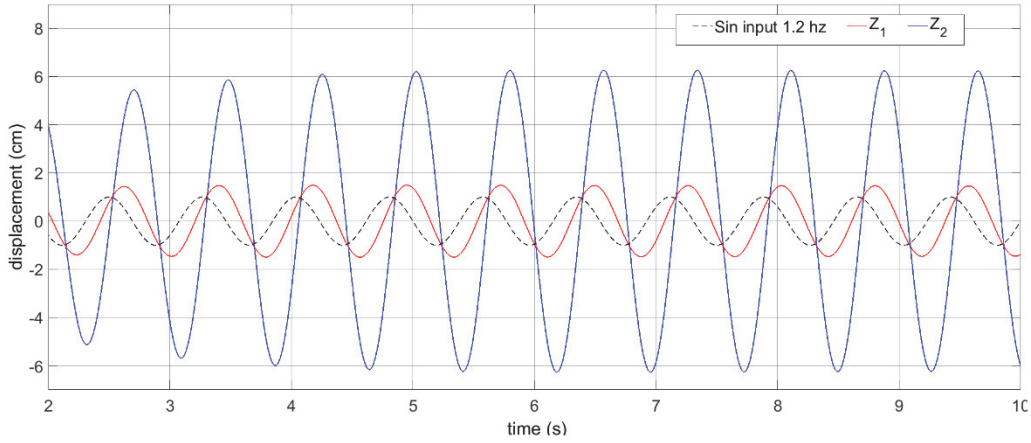

Figure 2.13 Time-domain response of the two-DOF model for 1.2 Hz sinusoidal excitation.

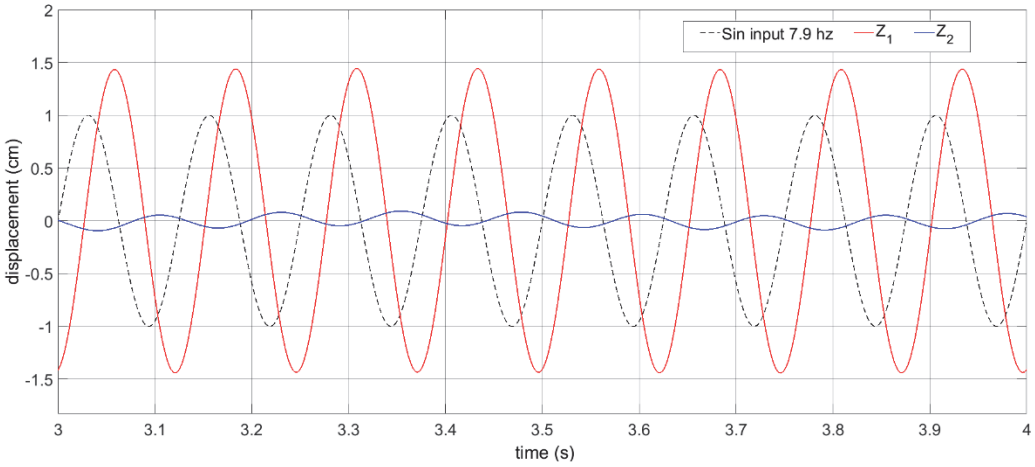

Figure 2.14 Time-domain response of the two-DOF model for 7.9 Hz sinusoidal excitation.

From the figure 2.13 it possible to note the first mode of the system. The first natural frequency (1.2 Hz) is the natural frequency of car body bounce. Indeed the car body oscillation is amplified in respect to the input and bogie oscillation. Similarly, figure 2.14 points out the natural frequency for bogie bounce (7.9 Hz). When the system is excited by a sinusoidal input of such frequency occurs the bogie resonance, while the car body does not vibrate. This mode and the correspondent frequency is that of interest for the EH design.

2.4.2 Nine-degree-of-freedom model

The components of the system are considered as rigid bodies. A rigid body in the space has six dynamic degrees of freedom: three displacements (longitudinal, lateral, and vertical) and three rotations (roll, pitch, and yaw). Each dynamic DOF results in a second-order coupled differential equations and thus, for *N* number of components in the system, 6 *N* deferential equations will be required to represent the system mathematically. Solutions for all of these differential equations are not only expensive, but many times are unnecessary. Therefore, it is important to establish the objective of a mathematical model. Considering vertical and lateral motions of a vehicle, It has been observed that they are relatively weakly coupled [85]. Consequently, it may not be necessary to include the vertical DOF in the study of the lateral response of the vehicle or the lateral DOF in the vertical response. For the complete vertical response, the bounce, pitch, and roll DOF of the components can be considered. Similarly, it may be considered the longitudinal, pitch, and roll DOF in studies of the longitudinal dynamic behaviour; and the lateral, yaw, and roll DOF of the components for lateral response.

The model consists of one vehicle body, two bogies and four wheel-sets. Bogies are connected to wheels via primary suspensions systems, and to the car body via the secondary ones. Building on the previous considerations, for both car body and bogies three DOF (bounce, pitch and roll) have been considered. Therefore, the entire model results in nine DOF. The other assumptions made for the modelling are:

1. Only forces and motions in the vertical plane parallel to the rails are considered.
2. In the vertical direction, wheel and rail are considered always in contact. This is a *geometric constraint*.
3. The vehicle moves with a constant velocity *v* and vehicle resistances due to wind, grade, curvature, and other sources are neglected.
4. The primary and secondary suspension components are modelled with viscous dampers and spring elements.
5. All kinematic relations and all spring and damper values can be *linearized* with respect to a reference state, which is like to say that all motions are considered small.

Figure 2.15 shows the model of the vehicle. Table 2.2 shows the parameters of the mathematical model.

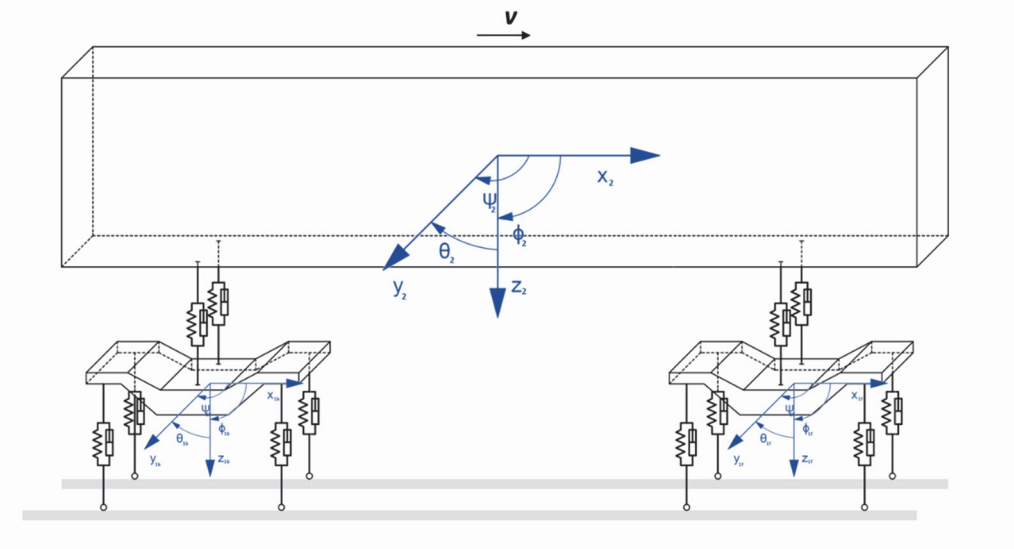

Figure 2.15 Rail vehicle model for vertical dynamics.

The bounce, pitch and roll DOF are indicated respectively with the coordinates: z_{1f}, ϕ_{1f}, θ_{1f} for the front bogie; z_{1b}, ϕ_{1b}, θ_{1b} for the rear bogie; and z_2, ϕ_2, θ_2 for the car body.

Table 2.2 Parameters of rail vehicle model for vertical dynamics.

Parameter	Description	Unit
M_c	Car body mass	Kg
M_{bf}	Front bogie mass	Kg
M_{bb}	Rear (back) bogie mass	Kg
$J_{c\phi}$	Car body pitch inertia	Kg m^2
$J_{c\theta}$	Car body roll inertia	Kg m^2
$J_{b\phi}$	Bogie pitch inertia	Kg m^2
$J_{b\theta}$	Bogie body roll inertia	Kg m^2
l_b	Half of the distance between two wheelsets in a bogie	m
w_b	Half of the distance between attached points of secondary suspensions in a bogie	m
l_c	Half of the car body length	m
w_c	Half of the car body width	m
K_1	Stiffness of primary suspension	N/m
K_2	Stiffness of primary suspension	N/m
K_θ	Angular stiffness of the anti-roll spring	N m/rad
C_1	Damping coefficient of primary suspension	N s/m
C_2	Damping coefficient of secondary suspension	N s/m

The inputs of the model are the displacements of the wheels caused by vertical irregularities of the track. We denote with d_{1r}, d_{1l}, d_{2r}, d_{2l}, the vertical displacements of front bogie wheels. The subscript *'1'* and *'2'* indicate the leading and trailing wheelset of front bogie while the subscript '*r*' and '*l*' denote the right side or left side. Similarly, d_{3r}, d_{3l}, d_{4r}, d_{4l}, are the vertical displacements of rear bogie wheels and subscript '3' and '4' indicate the leading and trailing wheelset of such bogie.

For the car body the dynamic balance along vertical, pitch and directions can be written respectively as:

$$M_c\ddot{z}_2 - 4K_2z_2 - 4C_2\dot{z}_2 + 2K_2z_{1f} + 2K_2z_{1b} + 2C_2\dot{z}_{1f} + 2C_2\dot{z}_{1b} = 0 \quad (2.7)$$

$$-J_{c\phi}\ddot{\phi}_2 - 4C_2l_c^2\dot{\phi}_2 - 4K_2l_c^2\phi_2 + 2K_2l_cz_{1f} - 2K_2l_cz_{1b} + 2C_2l_c\dot{z}_{1f} - 2C_2l_c\dot{z}_{1b} = 0 \quad (2.8)$$

$$-J_{c\theta}\ddot{\theta}_2 - 4C_2w_c^2\dot{\theta}_2 - 4K_2w_c^2\theta_2 + 2K_2w_c^2\theta_{1f} + K_\theta\theta_{1f} + 2K_2w_c^2\theta_{1b} + K_\theta\theta_{1b} - 2K_\theta\theta_2 + 2C_2w_c^2\dot{\theta}_{1f} + 2C_2w_c^2\dot{\theta}_{1b} = 0 \quad (2.9)$$

For the front bogie, the equations of motion for the three DOF are derived as follow:

$$-M_{bf}\ddot{z}_{1f} - 2C_2\dot{z}_{1f} - 2K_2z_{1f} + 2C_2\dot{z}_2 + 2K_2z_2 + 2K_2l_c\phi_2 + 2C_2l_c\dot{\phi}_2 - 4C_1\dot{z}_{1f} - 4K_1z_{1f} + C_1\dot{d}_{1r} + C_1\dot{d}_{1l} + C_1\dot{d}_{2r} + C_1\dot{d}_{2l} + K_1d_{1r} + K_1d_{1l} + K_1d_{2r} + K_1d_{2l} = 0 \quad (2.10)$$

$$-J_{b\phi}\ddot{\phi}_{1f} - 4C_1l_b^2\dot{\phi}_{1f} - 4K_1l_b^2\phi_{1f} + K_1l_bd_{1r} + K_1l_bd_{1l} - K_1l_bd_{2r} - K_1l_bd_{2l} + C_1l_b\dot{d}_{1r} + C_1l_b\dot{d}_{1l} - C_1l_b\dot{d}_{2r} - C_1l_b\dot{d}_{2l} = 0 \quad (2.11)$$

$$-J_{b\theta}\ddot{\theta}_{1f} - 4C_1w_b^2\dot{\theta}_{1f} - 2C_2w_c^2\dot{\theta}_{1f} - 4K_1w_b^2\theta_{1f} - 2K_2w_c^2\theta_{1f} - K_\theta\theta_{1f} + K_\theta\theta_2 + 2K_2w_c^2\theta_2 + 2C_2w_c^2\dot{\theta}_2 + K_1w_bd_{1l} + K_1w_bd_{2l} - K_1w_bd_{1r} - K_1w_bd_{2r} + C_1w_b\dot{d}_{1l} + C_1w_b\dot{d}_{2l} - C_1w_b\dot{d}_{1r} - C_1w_b\dot{d}_{2r} = 0 \quad (2.12)$$

In the similar way can be derived the model of the backside bogie.

The equations from 2.7 to 2.12 can be rearrange in a more compact form. So for the car body the questions became respectively:

$$\ddot{z}_2 = \frac{2C_2}{M_c}\cdot\left(\dot{z}_{1f} + \dot{z}_{1b} - 2\dot{z}_2\right) + \frac{2K_2}{M_c}\cdot\left(z_{1f} + z_{1b} - 2z_2\right) \quad (2.13)$$

$$\ddot{\phi}_2 = -\frac{2C_2l_c}{J_{c\phi}}\cdot\left(2l_c\dot{\phi}_2 - \dot{z}_{1f} + \dot{z}_{1b}\right) - \frac{2K_2l_c}{J_{c\phi}}\cdot\left(2l_c\phi_2 - z_{1f} + z_{1b}\right) \quad (2.14)$$

$$\ddot{\theta}_2 = -\frac{2C_2 w_c^2}{J_{c\theta}} \cdot (2\dot{\theta}_2 - \dot{\theta}_{1f} - \dot{\theta}_{1b}) - \frac{2K_2 w_c^2 + K_\theta}{J_{c\theta}} \cdot (2\theta_2 - \theta_{1f} - \theta_{1b}) \quad (2.15)$$

For the front bogie:

$$\ddot{z}_{1f} = -\frac{2C_2}{M_{bf}} \cdot \left(\dot{z}_{1f} - \dot{z}_2 - l_c\dot{\phi}_2\right) - \frac{C_1}{M_{bf}} \cdot \left(4\dot{z}_{1f} - \dot{d}_{1r} + \dot{d}_{1l} - \dot{d}_{2r} - \dot{d}_{2l}\right) - \frac{2K_2}{M_{bf}} \cdot \left(z_{1f} - z_2 - l_c\phi_2\right) - \frac{K_1}{M_{bf}} \cdot (4z_{1f} - d_{1r} - d_{1l} - d_{2r} - d_{2l}) \quad (2.16)$$

$$\ddot{\phi}_{1f} = -\frac{C_1 l_b}{J_{b\phi}} \cdot \left(4l_b\dot{\phi}_{1f} - \dot{d}_{1r} - \dot{d}_{1l} + \dot{d}_{2r} + \dot{d}_{2l}\right) - \frac{K_1 l_b}{J_{b\phi}} \cdot \left(4l_b\phi_{1f} - d_{1r} - d_{1l} + d_{2r} + d_{2l}\right) \quad (2.17)$$

$$\ddot{\theta}_{1f} = -\frac{C_1 w_b}{J_{b\theta}} \cdot \left(4w_b\dot{\theta}_{1f} - \dot{d}_{1l} - \dot{d}_{2l} + \dot{d}_{1r} + \dot{d}_{2r}\right) - \frac{2C_2 w_c^2}{J_{b\theta}} \cdot \left(\dot{\theta}_{1f} - \dot{\theta}_2\right) - \frac{K_1 w_b}{J_{b\theta}} \cdot \left(4w_b\theta_{1f} - d_{1l} - d_{2l} + d_{1r} + d_{2r}\right) - \frac{2K_2 w_c^2 - K_\theta}{J_{b\theta}} \cdot (\theta_{1f} - \theta_2) \quad (2.18)$$

For the rear bogie:

$$\ddot{z}_{1b} = -\frac{2C_2}{M_{bb}} \cdot \left(\dot{z}_{1b} - \dot{z}_2 + l_c\dot{\phi}_2\right) - \frac{C_1}{M_{bb}} \cdot \left(4\dot{z}_{1b} - \dot{d}_{3r} + \dot{d}_{3l} - \dot{d}_{4r} - \dot{d}_{4l}\right) - \frac{2K_2}{M_{bb}} \cdot (z_{1b} - z_2 + l_c\phi_2) - \frac{K_1}{M_{bb}} \cdot (4z_{1b} - d_{3r} - d_{3l} - d_{4r} - d_{4l}) \quad (2.19)$$

$$\ddot{\phi}_{1b} = -\frac{C_1 l_b}{J_{b\phi}} \cdot \left(4l_b\dot{\phi}_{1b} - \dot{d}_{3r} - \dot{d}_{3l} + \dot{d}_{4r} + \dot{d}_{4l}\right) - \frac{K_1 l_b}{J_{b\phi}} \cdot (4l_b\phi_{1b} - d_{3r} - d_{3l} + d_{4r} + d_{4l}) \quad (2.20)$$

$$\ddot{\theta}_{1b} = -\frac{C_1 w_b}{J_{b\theta}} \cdot \left(4w_b\dot{\theta}_{1b} - \dot{d}_{3l} - \dot{d}_{4l} + \dot{d}_{3r} + \dot{d}_{4r}\right) - \frac{2C_2 w_c^2}{J_{b\theta}} \cdot \left(\dot{\theta}_{1b} - \dot{\theta}_2\right) - \frac{K_1 w_b}{J_{b\theta}} \cdot (4w_b\theta_{1b} - d_{3l} - d_{4l} + d_{3r} + d_{4r}) - \frac{2K_2 w_c^2 - K_\theta}{J_{b\theta}} \cdot (\theta_{1b} - \theta_2) \quad (2.21)$$

The nine equations from 2.13 to 2.21 are the modelling equation of railway vehicle vertical dynamics.

This model, for a given truck and velocity, receives in input the vertical displacements of the wheels and allows the calculation of the displacements, velocities and accelerations of the car body and the bogies. In particular, this model was created with the purpose of evaluating the relative motion of secondary suspensions during normal operations. As

we will see later, this data can be used as inputs to evaluate the behaviour of the proposed EH device during train operations, both in simulation and experimental environment.

Chapter 3

Energy harvesting device integrated in the pneumatic spring

In this chapter the proposed energy harvesting device integrated in the pneumatic spring is presented. First, a pneumatic suspension system is analysed to understand the working principle and how it is composed and then an overview on the air spring modelling approach is presented, focussing on the multi-physics techniques. In the last section the layout of the energy-harvesting device integrated in the air spring is presented alongside a detailing of the system hardware and an explanation of the operation principle.

3.1 Railway pneumatic suspension

Most common passenger trains perform suspension into two stages: the primary suspension is located between the axles and the bogie frame and is most accountable for vehicle stability and guidance; the secondary suspension, instead, connects the bogie frame to the car body and has the main dynamic task of ensuring passenger comfort.

The most common suspension components include coil springs, friction-based components such as leaf springs, rubber springs, air springs and hydraulic dampers. Moreover, other components such as traction links, anti-roll bars and bump stops should also be considered in the suspension context [86].

Nowadays pneumatic springs are widespread on passenger trains to ensure the secondary suspension. They present some fundamental advantages over the classical helical spring systems which affirmed their diffusion [59]:

- reduced weight and size for equivalent stiffnesses
- improved passenger comfort and noise insulation
- vertical and transverse stiffness are provided by a single component

- possibility of constant car body height with the payload variation by adding or removing air in the cushion
- suspension stiffness regulation as a function of the payload by means of air pressure setting, given a constant eigenfrequencies
- possibility to increase damping by adding restriction orifices in the pneumatic circuit.

The main component of the secondary suspension are the pneumatic springs, also called *air springs*, *air cushions* or *bellows*. Several types of pneumatic springs are present on the market, but from a functional point, they can be considered formed by a flexible member linked to two metallic rigid plates, defining a closed volume where pressurised air was inflated in (figure 3.1).

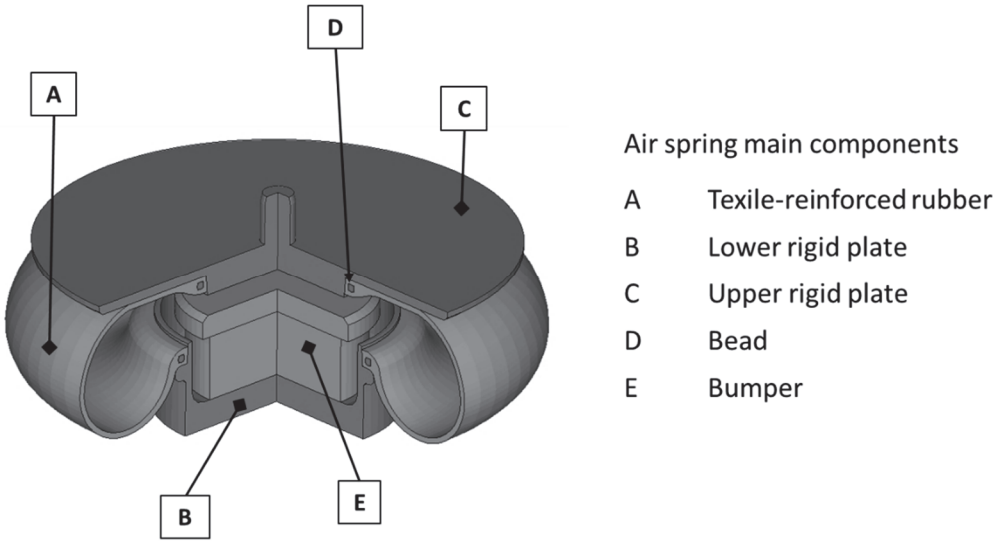

Figure 3.1 Schematic illustration of air spring main components.

The flexible member is usually made from textile-reinforced rubber, which allows vertical and horizontal deformation. The relative pressure can vary between 3 and 7 bar depending on the load. A bead ensures the link between the reinforced rubber and upper and lower plates. This coupled element is similar to the one used for tyres. Its core is made up of several individually rubber-coated steel wires formed into a hoop, that is then provided with a rubber apex. When deflated, air springs sit down on an emergency bumper. This component, built in rubber, rubber and fabric or rubber and steel, is used as an emergency suspension in case of the pneumatic system fault to prevent damage to the air spring or rail car body. It can be located internally or externally to the bellows.

The *pneumatic circuit* in which the bellows are integrated completes the secondary suspension. Therefore, other components of the system are auxiliary tanks, pipes orifices, levelling valves, compressors etc. (figure 3.2).

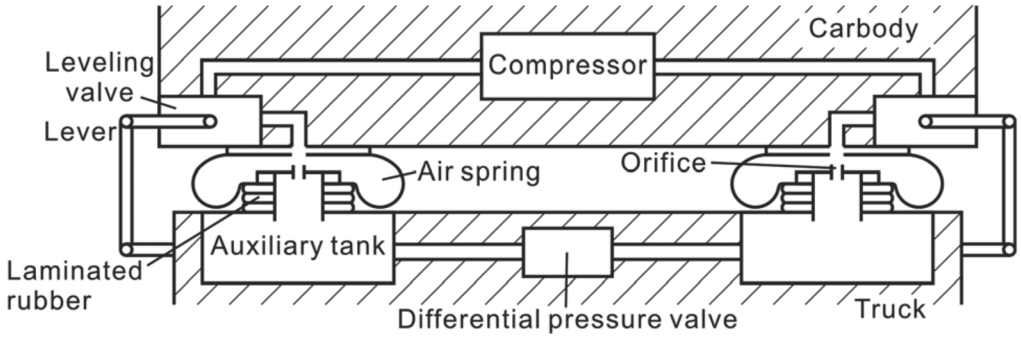

Figure 3.2 illustration of the various component of a pneumatic secondary suspension as represented by Nakajima et al. [87].

The frequency and spring rate characteristics of the air spring can be set by incorporating an auxiliary air reservoir. The *auxiliary tanks* have the main task of increasing the total air volume in order to make the suspension softer. Every tank is connected to the air spring via a *pipe,* which often presents a restriction *orifice* to increase suspension damping. Some air spring configuration presents an auxiliary tank integrated in their design to increase the damping.

A *differential pressure valve* connects the two auxiliary tanks or the two bellows of one bogie. It opens when the difference of pressure between the two auxiliary tanks exceeds the set value, from 1 to 2 bar, to equalize the pressures of both air springs.

The *levelling valve* keeps the vertical position of the car body constant when the load changes. A lever controls this valve. If the car body moves down due to the increase of the number of passengers, the lever connects the bellows to the pressure source and air is admitted into the suspension. On the contrary, if the car body moves up, the lever connects the bellows to the atmosphere allowing air discharge and implying the lowering the car body position.

3.2 Air spring modelling

The pneumatic suspension acts both in vertical and horizontal planes. In this context, we will focus on the vertical motion of the suspension since it will affect predominantly the EH system. Moreover, as shown by Facchinetti et al. in [88] the vertical and horizontal behaviours have a weak mutual interaction while the vertical dynamics can be considered not affected by the lateral or roll deformations of the bellows.

Several modelling approaches of air spring vertical behaviour have been proposed in literature. The models can be classified into *equivalent mechanical models* and *thermodynamic models* [86]. Equivalent mechanical models replace the air springs by equivalent lumped parameter springs, dashpots and masses. The approach of calculating the pressure in the bellows and the tanks and then deducing the corresponding force are the base for thermodynamic models. These models implement a mathematical formulation of thermodynamics processes in the suspension system giving a clear physical meaning at every parameter.

Equivalent mechanical modelling

As far as equivalent mechanical models are concerned, the simplest one is composed by a spring with a viscous dashpot in parallel. This model is only able to describe the quasi-static stiffness of the suspension and presents several problems in the definition of the damper parameter value, because of the non-linearity of the dissipative. More complex combinations of springs and dampers are proposed by different authors such as Oda-Nishimura [89] and Berg [90] with the purpose of considering the frequency dependency of the stiffness. Referring to figure 3.3a, the Oda-Nishimura model is composed a spring K_1 in series with the parallel of a spring K_2 and a viscous damper C. K1, K_2 and C represents the bellow stiffness, the air compressibility and the dissipations of the system respectively. Another spring K_3 can be considered in parallel at the aforementioned combination in order to take into account the additional stiffness due to the change in the effective area with the suspension height. This model is adequate for a wider frequency range. Berg proposes a three-dimensional model, whose the vertical part is shown in figure 3.3b. This model is able to take into the resonance effect of the air mass inertia present in the pipe that connect bellow and auxiliary tank, by means the introduction of an additional mass.

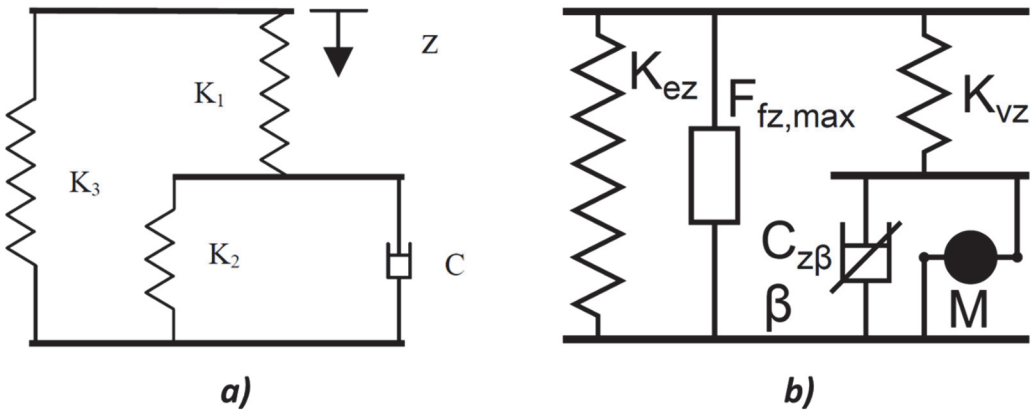

Figure 3.3 Bellows-tank equivalent vertical mechanical models: a) Oda-Nishimura and b) Berg.

The equivalent mechanical models are widely used in multibody vehicle dynamics simulation due to convenience in implementing them in multibody computer algorithm.

Thermodynamic modelling

In the context of this work, we focus on the thermodynamic models that allow the calculation of the airflow through the orifice and pipe, the pressure in the bellows and auxiliary tanks etc. Indeed these variables will be combined to the ones of the EH system to form the proposed multi-physics model.

Several models for vehicle pneumatic suspension can be found in literature [87], [88], [91]–[95]. These thermodynamic models have in common the mathematical implementation of the following main elements: bellows, auxiliary reservoir and connecting element (orifice or pipe). Other components such as the levelling valve can be added in function of model scope. This approach consists in modelling the various components of a pneumatic circuit using energy and mass balances and then connect each element in function of the form of circuit morphologies.

Quaglia and Sorli propose a useful model [91], then further developed by Docquier et al. [92], [93] to evaluate different formulation of loss effects in the piping. Figure 3.4 shows the reference scheme considered in the following to model the air suspension. It consists in a bellow connected to an auxiliary tank through an orifice.

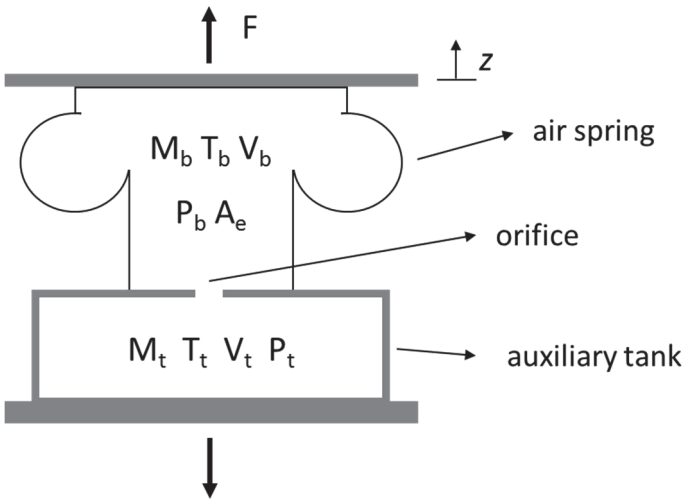

Figure 3.4 Thermodynamic scheme for air spring model.

Bellow and tank are modelled as pneumatic chambers in which the mass, the volume, the temperature and the pressure (thermodynamic state) vary because of the relative motion of bellow plates that causes a flow via the connected pipes. This flow is from the bellow to the tank if the plates move closer and from the tank to the bellow when the distance between the plates increases.

The bellow and tank are modelled, respectively, as variable size and constant size air volumes. These parameters must be known for thermodynamic modelling. As proposed by Quaglia and Sorli [91] and tested by Docquier [59], the volume of the bellow can be assumed dependent only on the air spring height and not on the internal pressure. Furthermore, same authors underline that the nonlinear relationship between volume and bellow height is closely approximated by a linear function. It is thus possible to write:

$$V_b(z) = V_{b0} + \frac{dV_b}{dz} \cdot z \tag{3.1}$$

Where V_b is the volume of the bellow, V_{b0} is the initial volume of bellow, z is bellow height and $\frac{dV_b}{dz}$ is the linear volumetric coefficient.

The vertical force F exerted by the air spring can be expressed as:

$$F = A_e P_{rel} \tag{3.2}$$

Where P_{rel} is the relative pressure between the air in the bellow (P_b) and ambient, A_e is the effective area. This area is an imaginary area over which the relative internal pressure is assumed to be acting. It is variable during air spring operations and is function

of air spring height and pressure $A_e = A_e(P_b, z)$. Generally, this parameter is empirically measuring the force *F* and varying the height at constant internal pressure. As this area does not correspond to a geometrically defined value, it is assessed by means of constant internal pressure tests in which force F is measured while varying height h. In the references [91]–[93] is shown that, being a weak dependence from the pressure, in first approximation is possible to assume that A_e vary linearly with bellow elongation.

The thermodynamic state of the air the bellows and auxiliary tank can be described using a formulation based on mass and energy balances. Concerning the air mass, the continuity equation, for both volumes, gives that the air mass variation is due to the flow rate through the pipe. Thus, we have for bellow and tank respectively:

$$\frac{\mathrm{d}m_b}{\mathrm{d}t} = \dot{m}_b = G \tag{3.3}$$

$$\frac{\mathrm{d}m_t}{\mathrm{d}t} = \dot{m}_t = -G \tag{3.4}$$

Equivalently to energy conservation equations, given the bellow volume from the (3.1), the tank volume (fixed) and the air mass they contain from (3.3) and (3.4), the pressure in pneumatic volumes can be calculated considering the polytropic law:

$$P\left(\frac{V}{m}\right)^k = cost. \tag{3.5}$$

Where *V* is the volume of the bellow or tank, *m* is the air mass in the bellows or tank and *P* is the (absolute) air pressure in the bellow or tank. The parameter *k* is the polytropic exponent whose value depends on assumptions made on the energy balance of the system. Generally, the process occurs in air spring is polytrophic but for simplicity in literature it is often debated as adiabatic ($k = c_p/c_v$) or isothermal (k=1). From a theoretical point of view, the isothermal transformation results more reliable for very low frequencies (0.1 – 0.5 Hz) and adiabatic one for increasing frequencies. In this study, the air spring vibration is regarded as an adiabatic process as commonly used in literature [92], [95]–[97]. To complete the knowledge of thermodynamic state, the air temperature in the volumes, can be evaluated from the perfect gas relation:

$$PV = mRT \tag{3.6}$$

Where R is the universal gas constant (286.9 J/kgK) and T the air temperature.

The second main component of air spring thermodynamic models is the model of the connection element between bellow and tank. Depending on whether this element is an orifice or a long pipe, it can be defined at different levels of complexity. Different models for this element are debated by Docquier et al. in [92], [93]. Referring to the orifice (figure 3.4) as a nonlinear component, the flow conditions through it may be sonic or non-sonic

depending on pressure difference between the linked chambers. Here we assume the flow rate through the orifice calculated in accordance to the ISO 6358 [98]:

$$G = DP_1\rho_{ref}\sqrt{\frac{T_{ref}}{T_1}}\sqrt{1-\left(\frac{\frac{P_2}{P_1}-b}{1-b}\right)^2}\cdot sign(P_2-P_1) \quad \text{if} \quad {}^{P_2}/_{P_1} > b = 0.518 \tag{3.7}$$

$$G = DP_1\rho_{ref}\sqrt{\frac{T_{ref}}{T_1}}\cdot sign(P_2-P_1) \quad \text{if} \quad {}^{P_2}/_{P_1} \leq b = 0.518 \tag{3.8}$$

Where:

- $P_1 = max\{P_b, P_t\}$, $P_2 = \min\{P_b, P_t\}$,
- $T_1 = max\{T_b, T_t\}$, $T_{ref} = 293.15\ K$
- *D* is sonic conductance
- *b* is critical pressure ratio
- T_{ref} and ρ_{ref} are the temperature and the density of the air at standard reference condition

According to the standard, the sonic conductance is related to the orifice *effective area*, *e,* by following equation:

$$e = D\rho_{ref}\sqrt{sRT_{ref}} \tag{3.9}$$

Where s= 1/ (1-b).

Combining equation (3.9) with (3.7) and (3.8) the expression of mass flow rate became:

$$G = P_1 e\sqrt{\frac{1}{sRT_1}}\sqrt{1-\left(\frac{\frac{P_2}{P_1}-b}{1-b}\right)^2}\cdot sign(P_2-P_1) \tag{3.10}$$

$$G = P_1 e\sqrt{\frac{1}{sRT_1}}\cdot sign(P_2-P_1) \tag{3.11}$$

3.3 Proposed device: energy harvester integrated in the air spring

3.3.1 System description

As debated in the chapter 2, the irregularities of the track generate some excitations at wheel-axle set during the train ride. Although filtered by the primary suspension systems, vibrations are transmitted to the bogie frame and therefore to the secondary suspensions, which often is formed by the air springs. In order to harvest this kinetic energy source, we propose a device located inside the bellow that may intercept this energy flow (figure 3.5).

This EH system must be able to extract the energy from the air spring environment (EH *mechanical part* or *harvester* - see paragraph 1.2.4) to make it usable for the conversion in electrical energy via an ad-hoc transduction mechanism (*transducer*). Finally, the obtained electrical energy is managed and transferred to the electrical load.

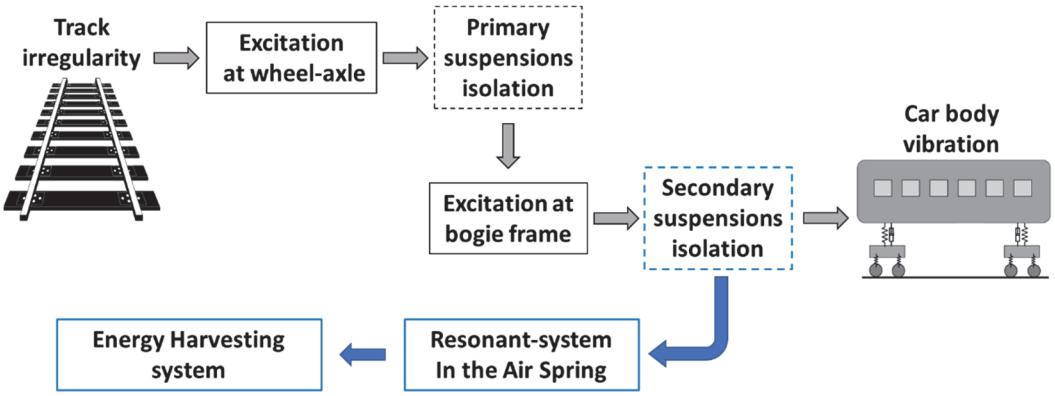

Figure 3.5 Location of the proposed EH system in the vehicle excitation flow.

The pneumatic bellows, as showed in paragraph 3.1, can present various configurations, but from a functionally point of view it is composed by a flexible member that connects two rigid metallic plates, forming a closed volume where pressurised air is inflated in. Usually the system has an internal emergency bumper. The idea is that of harvesting energy through a resonant system and an ad-hoc transduction mechanism located inside the defined closed volume, replacing and/or including the internal bumper. If the device replaces the bumper, the latter can be set outside the bellow; otherwise, it can be redesigned to include the harvester. For simplicity here we refer to the first case

remarking that all in the following can be extended to the second one. Figure 3.6 shows schematically the location of the resonant system in a pneumatic spring.

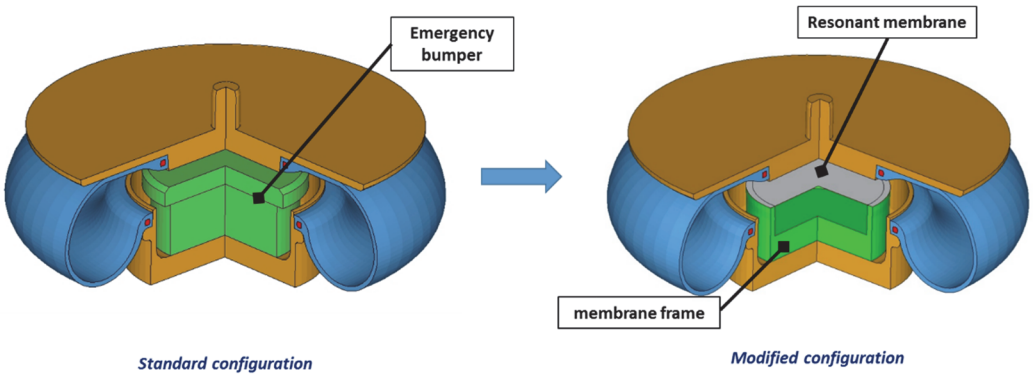

Figure 3.6 Illustration of resonant system integration in the air spring.

The layout of the energy harvester integrated in the air spring is shown in figure 3.7 via a sectioned view. As resonant system we consider a *flexible diaphragm* (FD) connected by a frame at the lower rigid plate. At the circle centre of the FD can be installed a *tuning mass* in order to set the device natural frequency at a required value so to have the desired resonance effect. This layout has been chosen to create two air chambers in the volume of the bellow: the principal one that we call *bellow chamber* (BC), and a small one, named *auxiliary chamber* (AC). This scheme is conceptually similar to the one reported in the section 3.2 in figure 3.4, with the difference that in that case the auxiliary volume is fixed, indeed in the considered system changes during operation. As detailed in the following paragraph this architecture has been considered with the purpose of exploiting the external excitation as much as possible. The BC and the AC are connected by means of one or more appropriately calibrated *orifices* present on the FD frame. These holes allow the airflow between the two chambers and thus guarantee the pressure equilibration. Moreover, they can affect the suspension damping.

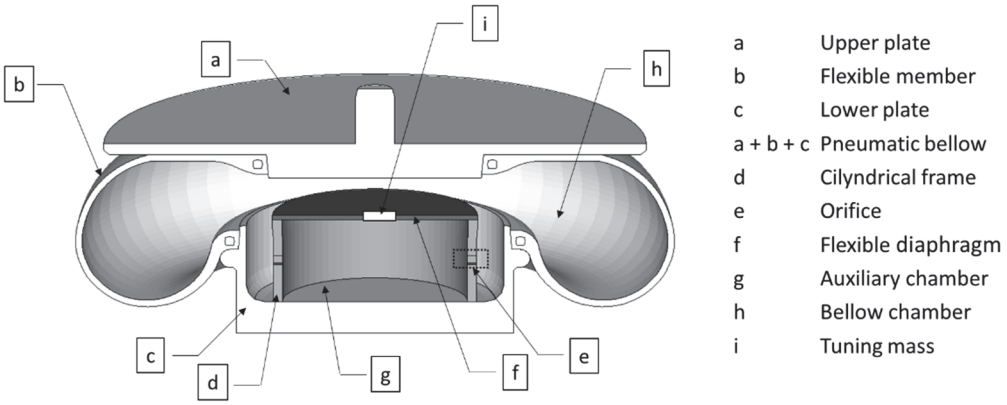

Figure 3.7 Layout of the energy harvester included in the air spring - sectioned view.

The layout concept of harvester has been designed observing that:

- The device must be integrated in the air spring component
- The dimension of the device must not exceed the volume occupied by the emergency bumper (that vary depending on air spring type and application)
- The device must be integral to the lower bellow plate in order to exploit the excitations in the frequency range discussed in the chapter 2 (7-10 Hz)
- In the bellow closed volume, a pressure oscillation occurs during the train ride.

As concerns the *transduction mechanism*, one or more films of piezoelectric material can be made integral with FD in order to exploits its deformation. These piezoelectric films are able to provide the conversion from mechanical energy into electrical energy.

Theoretically speaking the FD can be made of piezoelectric material but, typically, piezoelectric harvesters that work in 31-mode refer to layered structures. These structures are composed by an elastic substructure (usually metallic or carbon fibre), also called passive layer, to which are attached the flexible piezoelectric films, the active layer. Two kind of configuration are possible the unimorph and the bimorph [99]. In the first layout the active material is attached to one side only of the passive layer. For bimorph configurations the elastic substructure is embedded between two active layers.

In this study, to exploit commercially available components we consider arranging some rectangular piezoelectric films in a radial pattern on the upper surface of the FD as illustrate in figure 3.8 for different possible configuration. Each piezoelectric element is anchored at one end to the FD rigid frame and is free to move at the other end. Therefore the piezoelectric elements are in cantilever beam configuration, working in 31-mode.

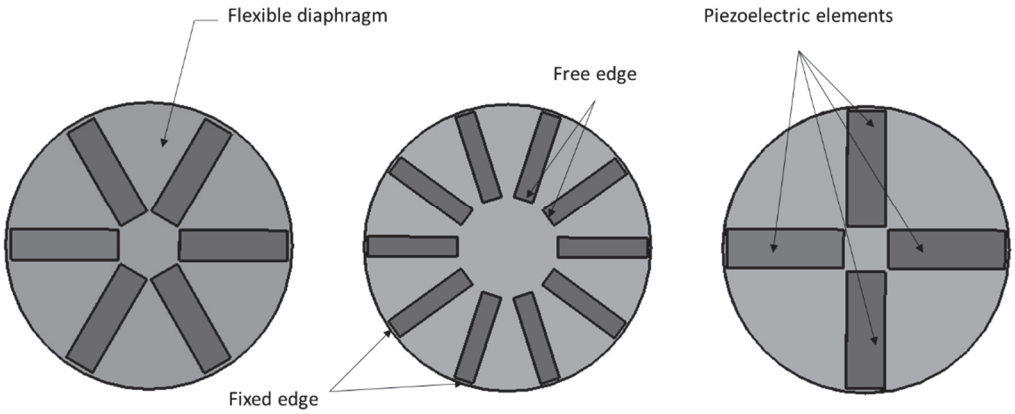

Figure 3.8 Possible layouts of commercial piezoelectric transducer on the flexible diaphragm.

3.3.2 Operation principle

In kinetic energy harvesting, the energy extraction process can be performed in two ways: by transferring the mechanical energy by means of direct application of a force or by exploiting the inertial force associated to a moving mass [100]. In practical applications the inertial generators are preferred to direct-force devices for vibration energy harvesting as they are simpler in construction.

With the purpose of making the most of the characteristics of the system and maximise the kinetic energy extraction, the joint action of both working principle has been evaluated. The excitation mechanisms investigated are:

- excitation deriving from the bogie during train operations, also called *base motion vibration,*
- excitation due to chambers pressure difference, called *pressure-induced vibration*.

Base motion vibration

Base-motion excitation mechanism refers to the energy extraction process that exploits the inertial force associated to the tuning mass. Indeed the vibration at the lower plate of the air spring, generated by track irregularities and transmitted by the bogie frame, are transmitted wholly to the FD support frame. These vibrations, making the flexible diaphragm resonant at the desired frequency by the use of opportune tuning mass, can be amplified to extract, convert and harvest energy [3].

When the FD deforms under the inertial force associated to the tuning mass, the piezoelectric films bend and normal strains are generated. The normal strain causes electrical charge to accumulate on the piezoelectric electrode, resulting in a voltage in the thickness direction of the piezoelectric element (31 piezoelectric working mode).

Pressure induced vibration

The second way investigated to extract energy is related to the characteristic of the bellow in forming a closed volume. During the train ride, there is a relative motion between lower and upper plate of each air spring. This relative motion induces a volume variation of the bellow and, thus, a pressure oscillation of the air included in it. In order to exploit this energy source, the layout of the system has been conceived to form an auxiliary chamber with FD (see figure 3.7). To explain the operation principle of the pressure induced vibration excitation mechanism we refer to the pure vertical motion of the spring. For simplicity we consider the upper plate fixed and impose a step displacement on the lower plate. In this condition, when the plates move closer to each other, there is an increment of the pressure in SC because of volume reduction. This pressure causes the diaphragm deflection. After a period of time, dependent on the calibrated holes dimension, the pressure in the AC balances the pressure in the principal one. At this time the diaphragm comes back to the equilibrium position (figure 3.9). In the same way, when plates increase their distance a depression occurs in the SC and the flexible diaphragm deflects in the opposite direction.

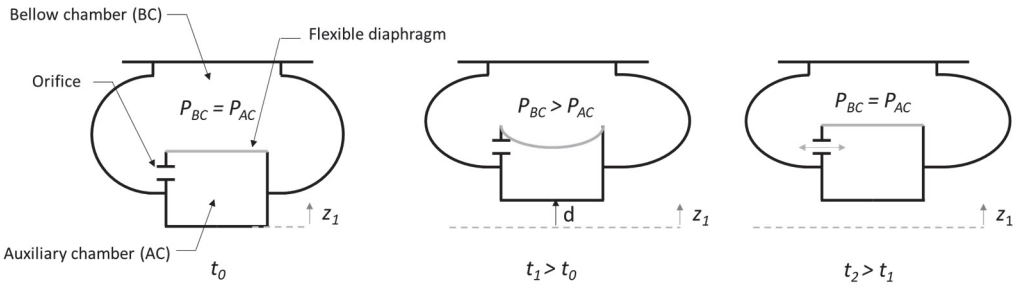

Figure 3.9 Operation principle of diaphragm deformation caused by pressure gradient between bellow chamber (BC) and auxiliary chamber (AC).

In other words, the calibrated holes on the cylindrical frame have the task of connecting the two chambers introducing a time delay in pressure oscillation and balance. This delay generates a pressure load that deforms the FD and, thus, the mechanical energy is transferred to the harvester by means the direct application of a force.

When a dynamic vibration occurs, one may expect that the FD may oscillate with a frequency similar to that observed in the pressure difference between the two chambers. When the FD deforms under oscillating pressure, the piezoelectric films bend and work in 31 mode.

3.3.3 Remark

The study of the operation principle builds on the observation that in the frequency range of interest (0-30 Hz) and for the displacements characterising the rail vehicle vertical dynamics, all bodies of the bellow-EH device integrated system (plates, FD, etc..) move into the air in subsonic condition. Therefore, the pressure in each chamber is considered spatially homogeneous and there are no considered pressure waves.

Another consideration concerns the possible working conditions of the proposed layout. It allows to investigate two working configurations to transfer the mechanical energy to the FD harvester: the base motion excitation only and the combination of it with the pressure induced excitation mechanism. When on the FD frame there are several holes big in diameter, qualitatively speaking, it is possible to assume that the pressure in both chambers is the same all the time. In such case, the FD moves only due to inertial load and therefore the energy of the only base motion excitation flows in the harvester. When the holes are appropriately calibrated, in number and dimension we introduce the delay in pressure and therefore the two excitation mechanisms act in combination.

The combination of excitation mechanisms aims to increase the deformation of piezoelectric elements that allow an increment of normal strain and therefore a higher voltage generation.

3.4 Reference air spring

The reference air spring used in this study has been purchased from Brighel srl. It is a commercial pneumatic spring and corresponds to the size of bellows used for a metropolitan train suspension. It is composed of three main parts: the steel upper plate, that should be fixed to the car body, the rubber diaphragm and the base block that contains the emergency bumper. In figure 3.10 are showed the air spring (a) and its 3D reconstruction in CAD environment (b).

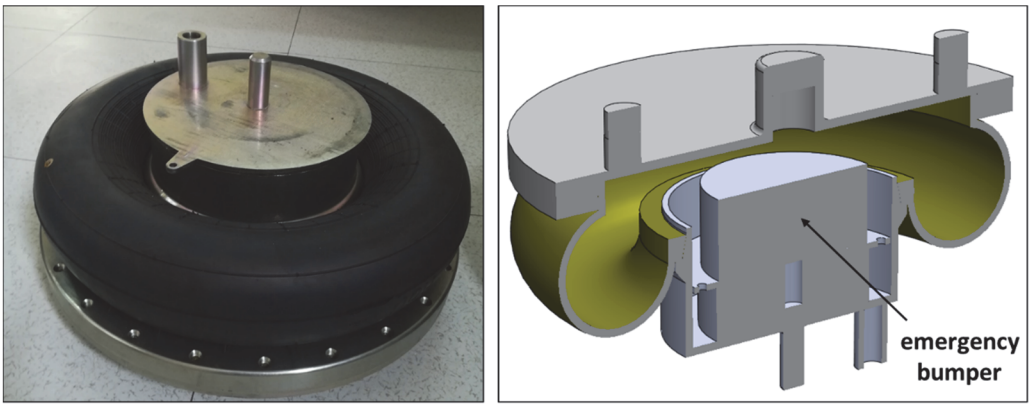

Figure 3.10 reference air spring (a) and its 3D CAD reconstruction (b).

The main parameters of the reference air spring are listed in Table 3.1.

Table 3.1 Reference air spring main parameters

Parameter	value	
Upper plate diameter	530	mm
Nominal distance between emergency bumper and upper plate	23	mm
Nominal height	200	mm
Working vertical stroke	40	mm
Maximum rubber diameter	570	mm

It should be emphasised that a pneumatic spring has been chosen as a reference to perform the quantitative analysis in the following, in simulation and experimentally, but the proposed methodology can be applied and scaled for whatever pneumatic spring.

Chapter 4

Finite element study of the harvester integrated in the air spring

This chapter is dedicated to the modelling of energy harvesting devices integrated in the railway pneumatic spring. It is important to point out that the dynamic of the harvester is strictly influenced by the air spring type and working condition. Conversely, the presence of the harvesting system modifies the geometry of the bellow. For this reason, we need an integrated model to accurately describe the phenomena. As reported in the 2nd and 3rd chapter, we focus on the vertical motion of the suspension as it mainly affects the harvester dynamics. Here, we first present a finite element model (FEM) that was developed to preliminary study the dynamic behaviour of the assembly: this model allows to visualize the overall behaviour of the proposed architecture from a mechanical and spatial point of view. We in the next chapter move to a multi-physical model, which includes the double excitation mechanism, for piezoelectric energy harvesting.

4.1 Finite Element model description

An accurate model is of great importance for the design of a resonant system. Taking advantages of finite element analysis technique, the characteristics of linked structure harvester-bellow have been studied, considering all the accessible nonlinearities and adopting proper load, geometry and material parameters as reported in [3].

This model has been developed to preliminary understand the dynamic behaviour of the system and to have a reference model for the design of the harvester.

The main aims of the model are:

- Investigate the dynamics of the integrated system
- Estimate the displacement of FD
- Evaluate the stresses/strains evolution of the FD during the operations
- Evaluate the pressure evolution for a given bellow.

Using ABAQUS finite element software a three-dimensional, half-symmetry model has been created. With regard to the modelling technique, the numerical model can be considered as composed by four parts: upper and lower plate, textile-reinforced rubber, FD and air. Upper and lower plates are both made of metallic materials and are modelled as a rigid body. They are defined by three dimension-three rigidity elements (R3D3 in ABAQUS). The boundary conditions can be defined on the reference points, which are located respectively on the centre of the upper and lower plate.

The flexible member, made from textile-reinforced rubber, can be considered as a composite material and modelled with the same techniques [1]. The eight node-solid elements (C3D8H in ABAQUS) are used to define the rubber part and the hyper-elastic Mooney-Rivlin material formulation. The steel cord-reinforcement between the inner and outer surface of the rubber wall is simulated with a rebar surface element (SFM3D4R in ABAQUS) embedded in the in the solid elements aforementioned. There are two rebar layers for modelling the composite structure. Different cord-reinforcement can be modelled changing the rebar diameter and the rebar angle in each layer.

The FD is discretized using S4R and S3R elements. An elastic rubber-like material is considered for this component and a concentrated mass is located in the centre to simulate the presence of the tuning mass. The nodes at the edge of the diaphragm, which are anchored to the rigid frame, are constrained using the *tie* technique. The same type of constraint is implemented to link the rubber and both metallic plates in correspondence of the surface that are in contact in nominal working condition.

The air behaviour inside the bellow is modelled using the element-based surface with normal versors pointing to the inside of the cavity. Surface elements are defined along the bottom and top rigid disk boundaries of the cavity to define it completely and to ensure proper calculation of its volume. The air inside the cavity is modelled as a compressible fluid satisfying the ideal gas law. During the simulation process, the software, using the defined surface geometry and reference node, creates the volume elements for the cavity. For this study two types of air elements are used: three dimension-three nodes element (F3D3 in ABAQUS) and three dimension-four nodes element (F3D4 in ABAQUS). If the nodes of the air elements move from their positions, the air elements volume change and so does the pressure. Here, it should be noted that considering the adopted approach, all the fluid elements share the nodes with their

adjacent elements thus, gas and solid are coupled. When, due to external loads, the bellow changes in shape, the variation of air volume is also evaluated as well as the pressure inside the bellow. Conversely, changes of the internal pressure involves movement of the air bag. Effectiveness of the method is dependent on the position of the cavity reference node, which is used to calculate the cavity volume and has a single degree of freedom representing the air pressure. Because of model symmetry, the fluid cavity doesn't appear to be completely enclosed, for this reason the reference node has been placed on the symmetrical axis of the air spring. The numerical model of pneumatic spring is shown in figure 4.1.

The interaction between the FD and the air inside the spring results in a pure damping action, thus the pressure acting on the two faces of the membrane is the same at any given time.

A comprehensive list of the parameters used for finite element simulations are reported in Table 4.1.

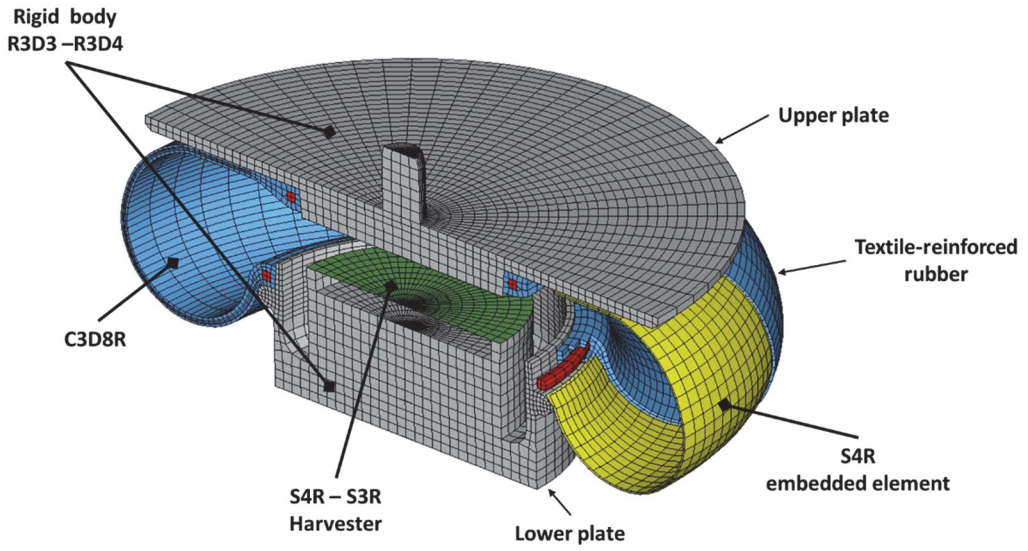

Figure 4.1 Air spring-harvester finite element model.

Table 4.1 Finite Element model parameter.

Parameter	value	
Textile-reinforced rubber component		
Thickness	6	mm
Rebar layer	2	-
Rebar angle	+30°/-30°	degree
Spacing	3.5	mm
Rebar diameter	1	mm
Rebar Young modulus	210	MPa
Rubber Mooney-Rivlin coefficient	C_{10} = 3.2; C_{01} = 0.8.	MPa
Fluid cavity		
Ambient pressure	0.1	MPa
Initial volume of air spring	1.42E+07	mm^3
Flexible diaphragm		
Radius	80	mm
Thickness	1	mm
Young modulus	60	MPa
Poisson coefficient	0.4	-
Density	0.001	g/mm^3

4.2 Static analysis

In order to evaluate the strength of the model some static simulation tests were performed. In particular, a static verification of the air spring behaviour was carried out in terms of pressure-volume variation and force-displacement relation for a vertical load. Furthermore, a static validation of the FD model stiffness was performed comparing simulation results with static experimental tests.

4.2.1 Air spring model static verification

One of the most important characteristic evaluated to verify the strength of the model for the verification is the vertical stiffness of the air spring. A range from -10 mm to +10 mm with respect to nominal position is explored to calculate the vertical stiffness. This range represents the usual strokes working condition of the considered case study. The

simulations are performed for different initial air pressures: 0.4 MPa, 0.5 MPa, 0.6 MPa, 0.7 MPa and 0.8 MPa.

For each value of initial pressure, numerical simulations are conducted in four static standard steps. Initial step (0) allows constraints application. Full constraints to the reference points of the upper and lower plate and symmetrical constraints to the air bag at the symmetry plane are applied. In the first step, the initial air pressure is assigned to the reference point of the air element by a ramp law. These two steps carry the model in the nominal bellow working condition that consists of the inflated air bag at a specific pressure at the design height. In the second step, the reference point of the upper plate is lowered in the vertical direction to the lower palate by 10 mm. Then, in the last step we push the upper plate to come back to the nominal height and then to move of 10 mm in the opposite direction. Under prescribed loads, the air bag volume change in function of the relative positions of the upper and lower plate.

In the figure 4.2 the volumetric change is reported for the aforementioned steps. In the first one, the bellow is inflated and consequentially the volume increases. In the second step (from 1 to 2 second), the lowering of upper plate induces a volume reduction and a pressure increment. In the last step the volume increases with the raising movement of the upper plate.

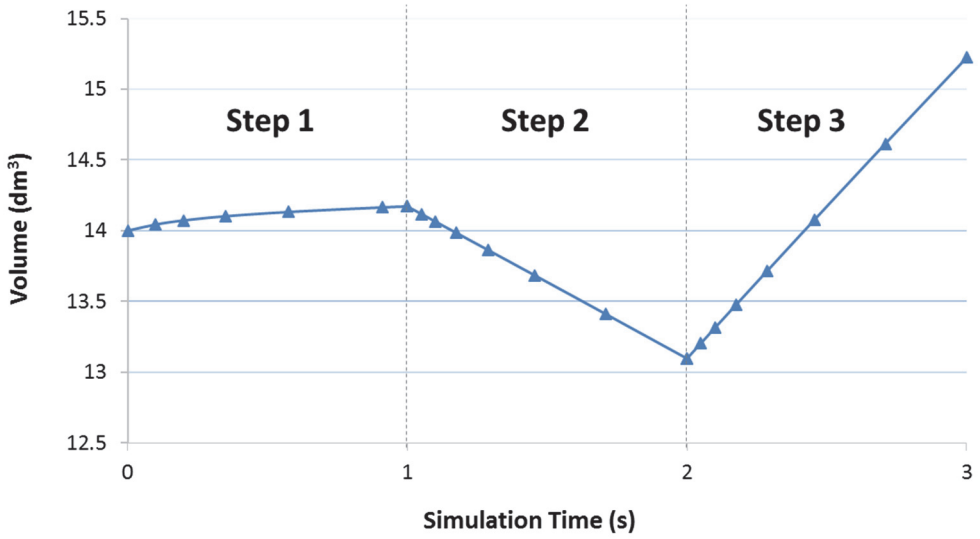

Figure 4.2 Bellow volumetric change in finite element simulation.

The static diagram of the force-displacement vertical curves for the five initial air pressures is shown in Figure 4.2. In these curves the direction of the compression direction is assumes as positive, which means the spring extension covers the range from -10 mm to 0 mm while the compression ranges from 0 mm to +10 mm.

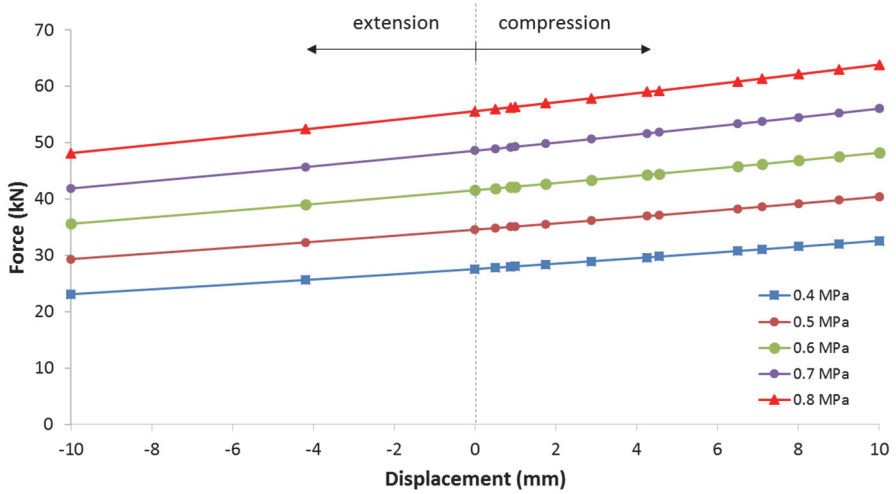

Figure 4.3 Force –displacement curve for different inflation pressure.

4.2.2 Flexible diaphragm model static validation

The vertical stiffness of the FD is a function of the material characteristics, and system geometry. Therefore, even though the material is assumed linear elastic, the matrix stiffness of the diaphragm could change significantly during the deformation for non-small displacements. In order to take into account this FD stiffness variation, the nonlinear geometric effects are considered in the finite element analysis.

The static analysis is conducted via a multistep simulation. In the initial step (step 0) the FD is fixed at the edges and in the last two steps it is loaded at the centre. It is loaded controlling its displacement and in output is recorded the reaction force. In the first step, FD centre is lowered in the vertical direction by 10 mm, subsequently in the second step we push it to come back to the nominal position and then to move by 10 mm in the opposite direction (figure 4.4).

For each displacement of the membrane centre, the vertical stiffness is calculated as reaction force-vertical displacement ratio, as showed in figure 4.5. It should be noted that the recording force in the model must be doubled as we are only considering half of the model. Simulation results depict that the stiffness of the FD can be considered constant

in the range of small displacements (0.5-1.5 mm), with a value of 0.044 N/mm. When the displacement imposed onto the membrane centre further increases, the membrane stiffness increases with a nonlinear law due to geometry variation.

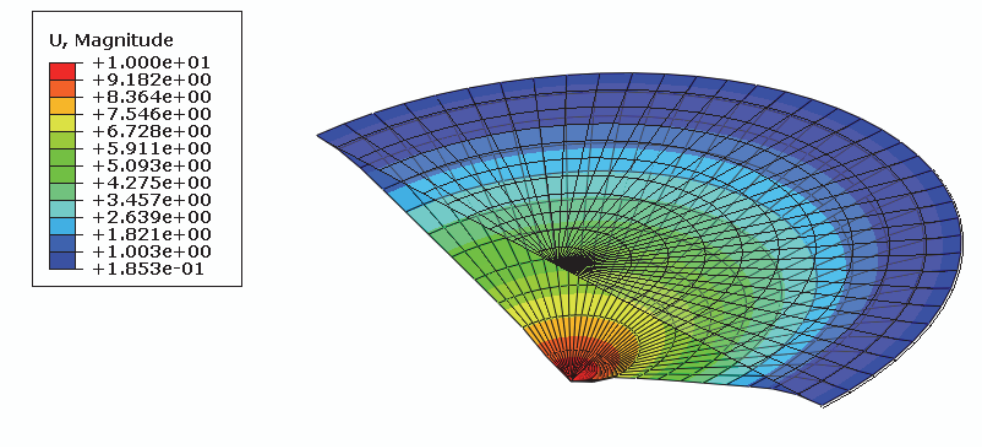

Figure 4.4 Amplified deformed shape of flexible diaphragm for a 10 mm static load at its centre.

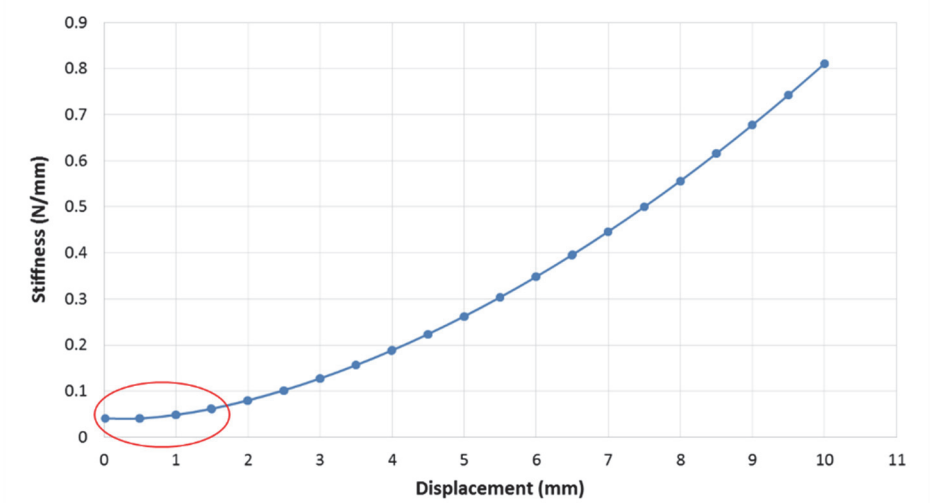

Figure 4.5 Flexible diaphragm stiffness as a function of its centre vertical displacement.

In order to validate the FD vertical stiffness simulations results have been compared with the experimental ones. The material used for FD is natural rubber operating in a temperature range of -40 °C to+85 °C. In the table 4.2 are reported the technical specifications.

Table 4.2 Main technical specification of the natural rubber used as flexible diaphragm.

Parameter	Regulation	value	
Density	-	1.04	gr/cm^3
Thickness	-	1	mm
Tensile strength	ASTM D412	1570	N/cm^2
Elongation	ASTM D412	600	%
Hardness	ASTM D2240	45	SH A

The experimental set-up used in the tests reproduces the one in simulation. The FD is constrained by a cylindrical steel frame and the experimental measurements are conducted by an in-house instrument, called V-ELA, developed at the laboratory of the Department of Industrial Engineering (DII) of the University Federico II. The instrument consists of two main parts: a fixed part, connected to the ground/specimen that is the external cylinder; and a moving part, composed by the elements inside that cylinder. The moving part allows the measurement of the force and displacement by means of a load cell and an LVDT transducer. An analogue-digital card for data acquisition completes the instrument layout. For the details on the V-ELA see Appendix A.

Test configuration is shown in figure 4.6. The loading rod applies the load at diaphragm centre. It is bound to the cylinder A and it is the last component that transmits the force to the specimen. It is considered infinitely rigid. A rigid disk with a central hole is positioned between the instrument and FD. Its bottom surface rests on the diaphragm frame and the upper surface supports the instrument fixed part. The central hole allows the passage of the loading rod and thus the load application.

Tests were conducted applying constant loads using known masses and load cell and LVDT transducer output were recorded. Several repetitions were made for each load. A third order polynomial law was used to fit the measured force-displacement points. Measured data and fitting curve are reported in figure 4.7.

The vertical stiffness was evaluated as a force-displacement ratio for each load. In figure 4.8 the FD stiffness vs. its centre displacement is plotted comparing the simulated and experimental results. The diagram show that the nonlinear law, due to geometry variation of the model, is able to approximate the behaviour of a real FD.

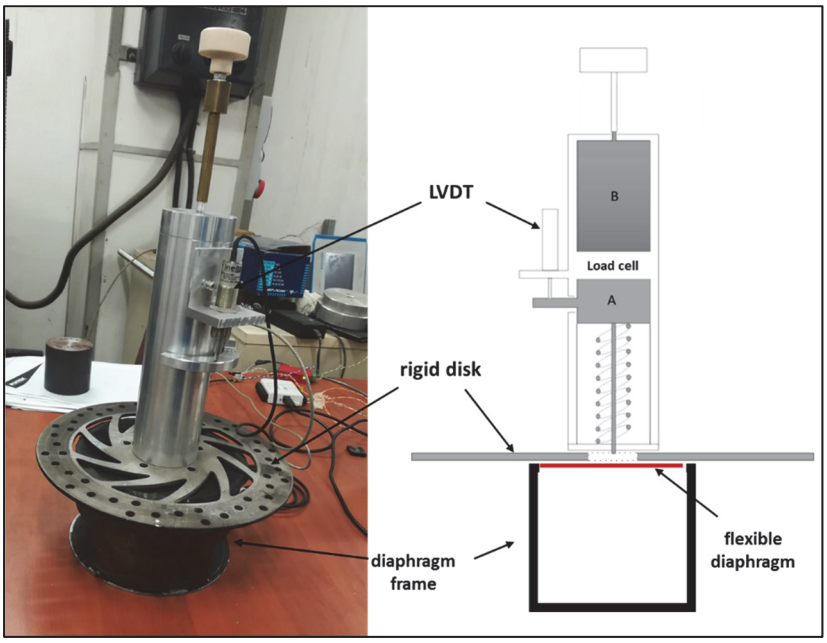

Figure 4.6 Experimental layout for the determination of FD static stiffness.

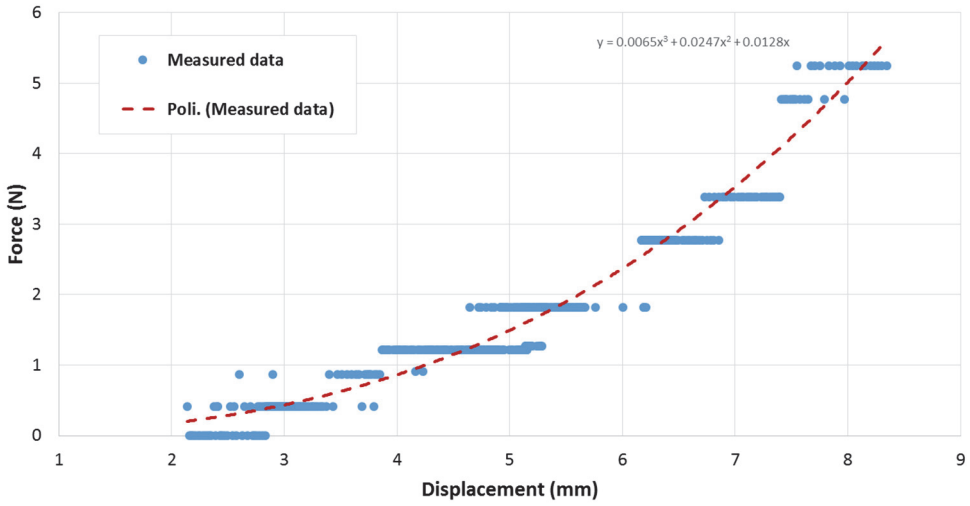

Figure 4.7 Measured data and fitting curve for static loads at flexible diaphragm centre

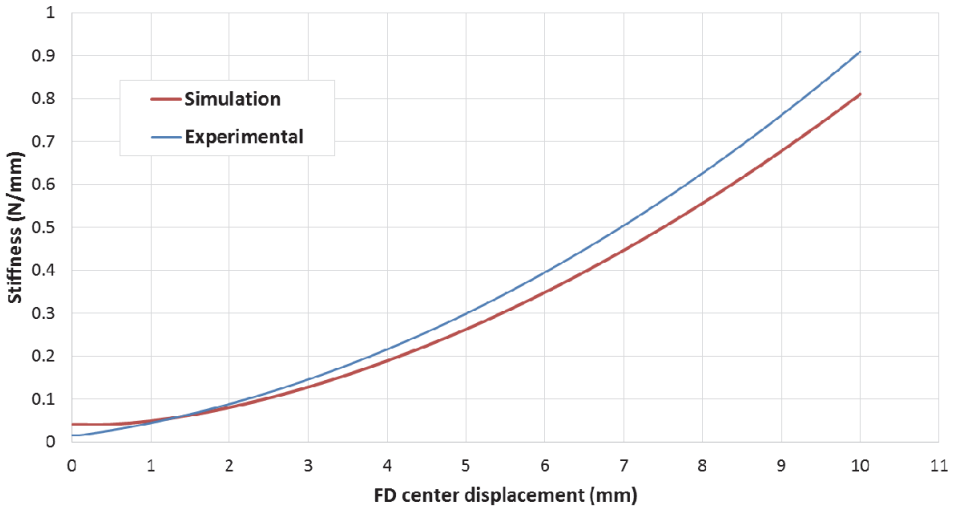

Figure 4.8 Flexible diaphragm stiffness-displacement curve: Simulation vs. experimental

4.3 Dynamic analysis

The dynamic analysis was performed in two steps. Firstly, a linear modal analysis has been performed to extract the natural frequencies of the FD and the relative mode shapes in the range of interest. Then dynamic simulations have been performed considering the geometric nonlinearities.

4.3.1 Linear modal analysis

As discussed in the chapter 2 and 3, the irregularities of the track lead to vibration at the air spring lower plate in a range of 0-30 Hz during the train ride. Assuming for the considered system a prominent exciting frequency of 8Hz and making the hypothesis of small displacement, we can linearize the FD model and, as showed in the section 4.1.2, consider constant the vertical stiffness K_{FD}. Therefore, we assume K_{FD}= 44 N/m. To obtain a natural frequency of the FD coincident with the exciting one, we can calculate the tuning mass approximating the system with a single degree of freedom lumped spring mass damper one. Thus we have:

$$M = \frac{K_{FD}}{(2\pi f_n)^2} = 0.017\ kg \qquad (4.1)$$

Where M is the tuning mass and f_n is the desired natural frequency.

Generally, this approach describes well systems with a single floating mass linked to the host structure as they have a relatively poor modal density and there is a clear separation between the first resonant frequency and the others.

Implementing in the model the calculated mass in the centre of FD, a modal analysis has been performed to extract his natural frequencies and the relative mode shapes in the range of 0 – 50 Hz. In the Figure 4.9 are reported the first three mode shapes at the eigenfrequencies of 8 Hz, 39 Hz and 46 Hz respectively. Here it should be noted that in that frequency range the first natural frequency is clearly distinct from the others.

The linear response of the system carried out considering the modal superposition procedure is summarised in Table 4.3 where the maximum displacement values of FD centre caused by a sinusoidal input at lower plate of amplitude 10 mm in steady state condition and for different frequencies are reported. Simulations are performed assuming a damping ratio equal to 0.3.

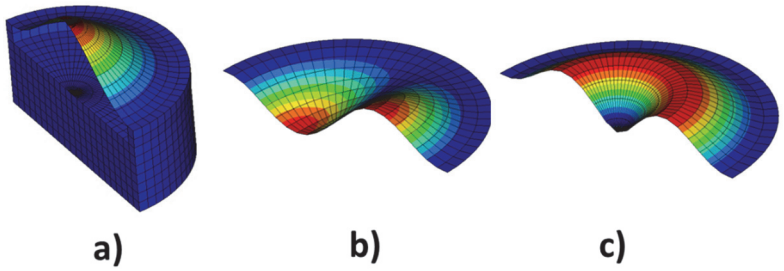

Figure 4.9 Mode shapes of the flexible diaphragm: a) 8 Hz; b) 39 Hz; c) 46 Hz.

Table 4.3 Dynamic linear response of flexible diaphragm centre.

Frequency (Hz)	**Diaphragm centre displacement (mm)**
1	10.1
6	17
8	18
12	8
21	3.3
30	3

4.3.2 Nonlinear analysis

The matrix equation of motion of the structure must be solved directly, rather than the uncoupled modal equations, to take into account the nonlinear behaviour of the FD and the flexible member of the air spring. In this case, Rayleigh material damping is commonly used to provide a source of energy dissipation. It expresses the damping matrix as a linear combination of the mass and stiffness matrices:

$$[C] = a[M] + b[K] \tag{4.2}$$

Where [*C*], [*M*] and [*K*] are the system damping, mass and stiffness matrices respectively; *a* and *b* are constants with units of s^{-1} and s.

In this study *a*=30 and *b*=0 are assigned to FD in order to simulate material dissipation and air damping.

Dynamic simulations are performed in two steps plus an initial one (step 0) in which full constraints to the reference points of the upper and lower plate and symmetrical constraints to the air bag at symmetry plane are applied. The inflation of the air spring at the prescribed initial air pressure are thus simulated in the first step. The inflation step is 0.02 seconds long and the pressure is assigned at the reference point of the air element by a ramp law. In the last step, a motion low is applied to the reference point of lower plate in vertical direction, freezing the remaining constraints.

Firstly, the step response of the system was carried out to evaluate the transient time and to check the simulation time. Figure 4.10 depicts the dynamics of the FD centre compared to a 10-mm amplitude smooth-step external excitation. Figure shows that after 0.3 seconds the transient extinguishes.

In order to investigate the dynamic behaviour of the resonant system in terms of deformed shape and stresses/strains time trend, sinusoidal displacement excitation at different frequencies around the resonance (6, 7, 8 , 9 and 10 Hz) has been simulated. As we will detail in the next paragraphs knowing stresses and strains trend is fundamental to make a prediction about voltage generation from piezoelectric films adopted for the conversion of mechanical energy into electrical one.

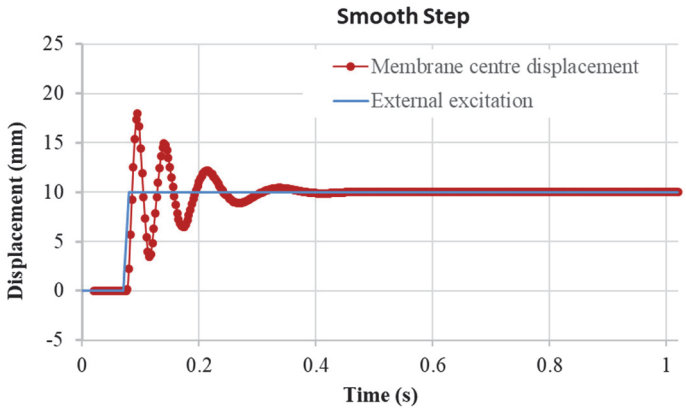

Figure 4.10 Dynamic nonlinear response of diaphragm centre for a smooth step external excitation

The sinusoidal motion, 10 mm in amplitude, is applied in vertical direction at lower plate. The evolution of the pressure inside the air bag is also monitored to verify the whole model behaviour and to quantify the magnitude of pressure oscillations. Due to lower plate motion the volume of the air spring changes with sinusoidal law as well as the air pressure. Figure 4.11 shows the pressure variation in the airbag for 0.7 MPa initial pressure and 8 Hz excitation frequency. In the range [0; 0.02] seconds the pressure increases until the nominal value, then in the second step [0.02; 1.02] seconds the pressure changes because of the bellow shape variation. The amplitude of pressure oscillation is 0.04 MPa, thus the pressure oscillates in the range [0.66; 0.74] MPa

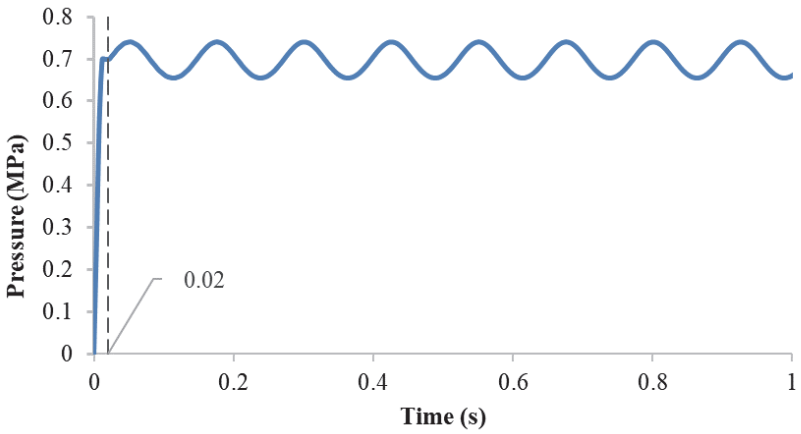

Figure 4.11 Air pressure variation inside the air spring under an 8 Hz sinusoidal load.

The dynamic displacement of FD centre compared to the sinusoidal motion imposed at lower plate is shown in figure 4.12. The reported values are sampled every 0.0025 seconds. The numerical simulation points out that the assembly diaphragm-tuning mass is sensitive to external excitation of 8 Hz amplifying the vibration amplitude. In particular, after the transient time (0.3 s), the maximum displacement of membrane centre is 13.9 mm. The relative motion between the FD centre and its edges (that are integral with its frame and thus with lower plate) can be calculated subtracting instant by instant the two curves in the figure. This parameter, as detailed in next paragraphs, is related to FD strains and thus to electrical generation by means of piezoelectric elements. The maximum relative displacement from simulations is 4.7 mm. With regard to the deformed shape of the FD, it reflects the mode shape characteristic of its first natural frequency for explored frequencies range.

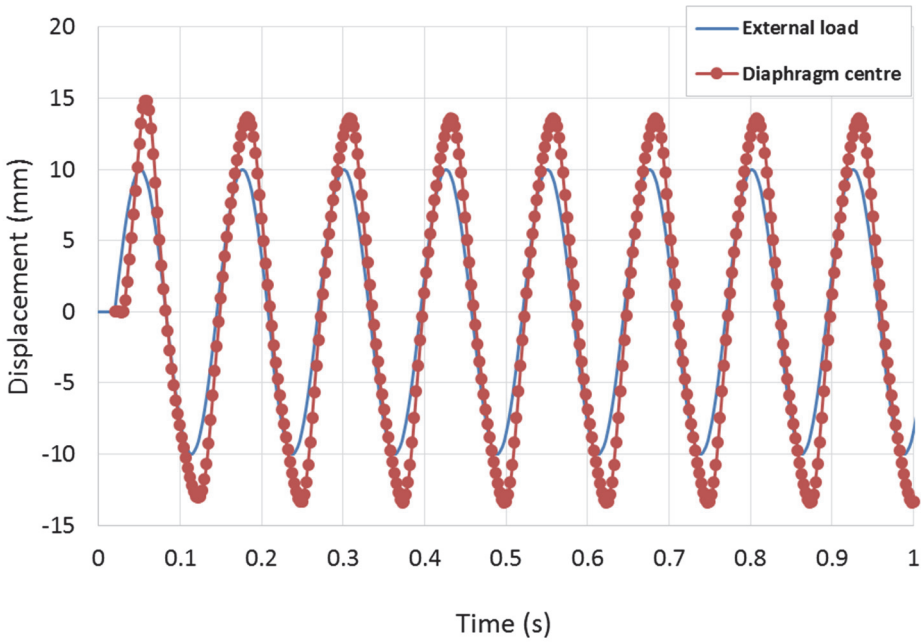

Figure 4.12 Dynamic response of FD centre compared to 8 Hz sinusoidal excitation.

The deformed shape of the FD integrated in the air spring is shown in the Figure 4.13. This depicts two instants where the FD reaches the maximum deformation corresponding to a positive (a) and negative (b) deflection of its centre.

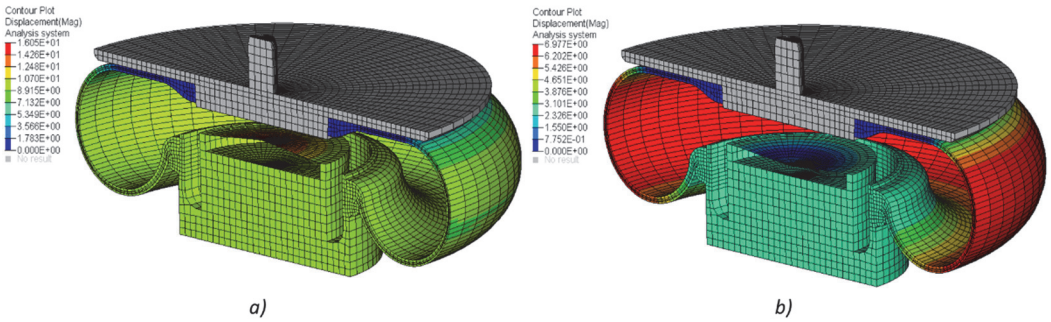

Figure 4.13 Flexible diaphragm nonlinear deformed shape.

Regarding to the stresses and strains that originate in the FD caused by its deflection, we only focus on the in-plane components. The two principal in-plane stress components are directed radially and circumferentially along the diaphragm. Considering the arrangement of rectangular piezoelectric films in a radial pattern on the upper surface of the FD as explained in section 3.3.1, we are interested most in the radial stresses. Indeed the elongation of the rectangular piezoelectric elements along radial direction produces voltage in vertical direction according the 31-working mode. In figure 4.14 are reported the FD and a reference system for one element. The radial direction is indicated with 1-axes, the circumferential with axes 2, and vertical direction with axes 3.

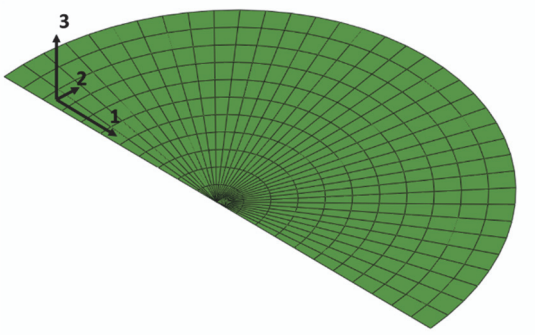

Figure 4.14 Reference system of FD elements in finite element simulations.

Analysing the time evolution of the radial stress in all elements of FD between the centre and the edges, we note that it does not vary with a sinusoidal law having the same frequency of the excitation but shows a periodic evolution. In figure 4.15 the radial stress evolution of one FD element is reported. This evolution is due to the nonlinearity of the phenomenon. Indeed, being in the field of non-small displacement the stress is given by the combination of two portion, the stress due to the bending and the stress due to the traction.

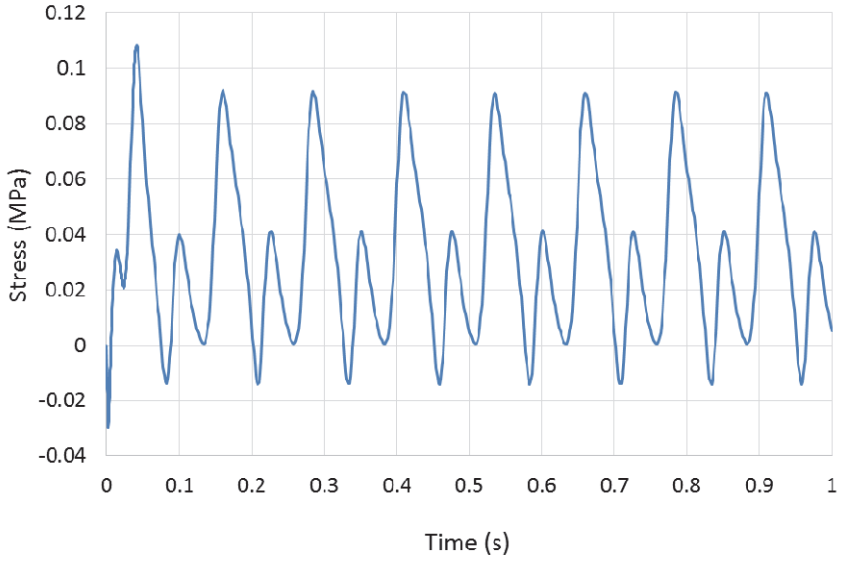

Figure 4.15 Stress evolution in an element of FD for an 8 Hz sinusoidal excitation.

Chapter 5

Energy harvesting device integrated in the air spring multi-physical modelling

The proposed finite element model allows to understand the overall dynamic behaviour of the integrated system from a mechanical point of view but is limited to be used as design tool. Indeed, it does not take into account neither the presence of the double excitation mechanism nor the electro-mechanical coupling due to the transduction mechanism. Here it should be emphasised that modelling the pressure-induced vibration and the electro-mechanical coupling, exploiting a commercial finite element environment, would require the use of the co-simulation technique between mechanical, fluid dynamics and piezoelectric domains. The equations of the different domains would be solved separately, exchanging information at fixed time steps, possibly with an iteration process to increase the numerical accuracy and stability, leading at high computational costs.

Here we opt for a strongly coupled approach for the multi-physics modelling, establishing the assembly of different domains contributions into one set of coupled equations to be solved in the same environment by the same integrator. The aim of the proposed model is to provide a suitable tool for the design of the device.

As indicated in chapter 1, and here reported for convenience, a kinetic EH system performs three main functions: energy extraction, energy conversion and energy transfer/management. Schematically speaking, the energy extraction from the environment is performed by the mechanical part, the harvester, and the conversion of extracted mechanical energy into electrical one by the transduction mechanism, or simply the transducer. The whole harvester-transducer is called generator. Finally, the electrical part is tasked with managing and transferring energy to the electric load. Below the three main parts constituting the EH system are analysed separately and then merged together in the global simplified model, focusing on the generator.

5.1 Mechanical part

The mechanical part of the proposed device, as detailed in section 3.3.1, is the resonant system, the flexible diaphragm (FD), connected by the holed rigid cylindrical frame at the lower rigid plate of the bellow. Furthermore, at the circle centre of the FD there is the tuning mass. The dynamics of the harvester is strictly influenced by the air spring type and working condition. For example, the pressure-induced vibrations are a function of the air spring state, volume, initial pressure and dynamics. For this reason, the modelling of the mechanical part must include all integrated system.

Literature review provides several models both for the kinetic harvester and for the pneumatic suspension as shown in paragraphs 1.2 and 3.1 respectively. Here we propose to use one model for each component such as the bellow, the auxiliary chamber, the orifice, the harvester, etc. and then to combine them to form the integrated model.

5.1.1 Lumped parameter model of the kinetic harvester

The general model of a kinetic energy harvester was first propose by Williams and Yate [101]. It is a lumped parameters model consisting of a second order mass-spring-damper single DOF system. This modelling approach well describes harvesters with a single floating mass linked to the host structure like electromagnetic energy harvesters as well as cantilever beam with bonded piezoelectric material. The finite element study, outlined in paragraph 4.1, shows that the proposed architecture has a relatively poor modal density, presenting a clear separation between the first natural frequency and the others. Therefore, our harvester can be modelled as an equivalent mechanical, second order mass-spring-damper single DOF system. The grater is the tuning mass in respect to that of FD, the more realistic is this assumption.

Figure 5.1 shows the equivalent mechanical model of the proposed kinetic energy harvester, integrated in the air spring and composed by lumped elements and a generic transducer connected to the electrical part. In this model:

- K_{air} is the air spring vertical stiffness
- C_{air} is the air spring vertical damping
- M is the tuning mass [kg]
- K_{FD} is the vertical stiffness of FD that depend on flexural stiffness of membrane and material [N/m]
- C_{FD} is the parasitic damping of FD

And where, according to the reference system of rail vehicle model (see chapter 2), z_1 and z_2 are the vertical displacements of bellow lower (integral with the bogie frame) plate and upper plate (integral with the car body) respectively.

In this scheme the mass motion, indicated with the absolute coordinate z_3, is representative of FD centre motion.

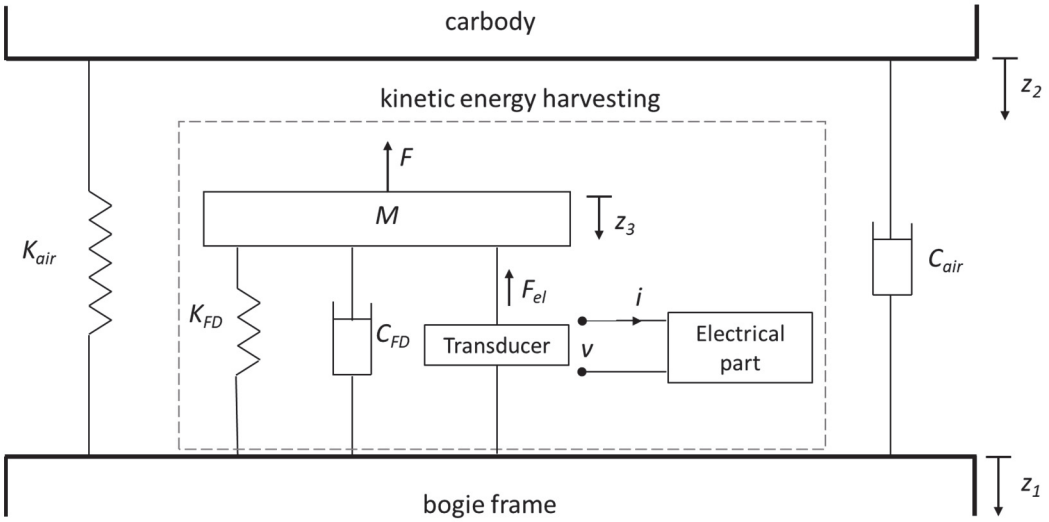

Figure 5.1 Equivalent mechanical model of proposed energy harvester integrated in the air spring.

In this model the mechanical system is connected to the electrical parts by a transducer. This element, due to the electromechanical feedback, exerts a force (F_{el}) that influences the dynamics of the seismic mass.

Here some considerations must be made about the stiffness K_m and damping C_m. As studied by finite element model (see paragraphs 4.2 and 4.3) the stiffness of FD plus the piezoelectric elements varies with nonlinear law for big relative displacements of mass in respect to the frame. A Similar effect can occur for the damping coefficient. In the proposed model, these coefficients are treated as constant. This assumption is built considering the model as a designing tool. Whose main goal is to preliminary find the device set up in terms of the stiffness K_m and the mass M, such to obtain the desired natural frequency.

In the most generic case both a frame motion and a direct force act on the seismic mass and exciting the system. In our study both excitations are present. More in detail, the motion of lower plate of the air spring represents the base-motion excitation and the

pressure difference between the spring and the auxiliary chamber is modelled as a force acting directly on the mass. Thus, the mechanical behaviour of the system is described by the equation:

$$M\ddot{z}_3 + C_{FD}(\dot{z}_3 - \dot{z}_1) + K_{FD}(z_3 - z_1) + F_{el} = F(t) \quad (5.1)$$

where dots stand for time-derivatives and *F(t)* is the external force directly applied to the mass. Rearranging in terms of relative displacement:

$$M(\ddot{z}_3 - \ddot{z}_1) + C_{FD}(\dot{z}_3 - \dot{z}_1) + K_{FD}(z_3 - z_1) + F_{el} = F(t) - M\ddot{z}_1 \quad (5.2)$$

This equation describes the dynamics of the mass, or equivalently of the FD centre, from a point of view of an observer integral with the lower plate of the air spring. Placing the relative displacement $z_r = (z_3 - z_1)$ we can write:

$$M\ddot{z}_r + C_{FD}\dot{z}_r + K_{FD}z_r + F_{el} = F(t) - M\ddot{z}_1 \quad (5.3)$$

Applying the superimpose principle, we study the system considering the loads separately in order to calculate the motion of diaphragm centre for each case and in combination. Here it should be underlined that the equation 5.3 is independent from the kind of technology employed for energy conversion.

Considering just the base motion excitation mechanism, *F(t)* is null and the equation 5.3 becomes:

$$M\ddot{z}_{r,bm} + C_{FD}\dot{z}_{r,bm} + K_{FD}z_{r,bm} + F_{el} = -M\ddot{z}_1 \quad (5.4)$$

Where the subscript *bm* indicates that we refer to only base-motion load condition. Considering only a direct force energy harvester equation 5.3 becomes:

$$M\ddot{z}_{r,pl} + C_{FD}\dot{z}_{r,pl} + K_{FD}z_{r,pl} + F_{el} = F(t) \quad (5.5)$$

It should be noted that, as no motion is imposed to the bellow lower plate and in turn to FD cylindrical frame, z_1 and its derivatives are both null. Therefore, in this relation results that $z_{r,pl}$ and its derivatives are equals to z_3 and its derivatives. Where the subscript *pl* indicates that we refer to only direct force application load condition that is caused by the pressure load gradient. In order to pass from the distributed load caused by the pressure difference between chambers to the force acting to the mass of lumped parameters model, the equivalent resultant force operating on the FD can be evaluated as:

$$F(t) = (P_{bc} - P_{ac}) \cdot \frac{\pi a^2}{4} \quad (5.6)$$

In which, in accordance with the notation of chapter 3:

- P_{bc} is the pressure in the bellow chamber
- P_{ac} is the pressure in the auxiliary chamber
- a is the radius of the FD.

Equations (5.5) and (5.6) describe the dynamics of the FD centre, known the pressure difference evolution between BC and AC. To calculate the pressure in chambers we refer to the thermodynamics model of the air spring presented in the paragraph 3.2.

Once again here it should be remarked that the layout of our system includes the bellow chamber (BC) and the auxiliary chamber (AC) but, although this scheme is conceptually similar to the one reported in the figure 3.4 of section 3.2, it presents the substantial difference that the auxiliary volume changes during operation. From the modelling point of view this means that, starting from the formulation presented in paragraph 3.2, we introduce a new one.

When both loads acting simultaneously, the overall relative displacement is given adding the two contributions calculated integrating the equations (5.4) and (5.5):

$$z_r(t) = z_{r,bm} + z_{r,pl} = z_3 - z_1 \tag{5.7}$$

5.1.2 Air spring with a volume-variable auxiliary chamber model

Bellow and auxiliary chamber are two pneumatic chambers in which the mass, the volume, the temperature and the pressure (thermodynamic state) vary because of the relative motion of bellow plates and of FD deflection, which cause a flow via the connection orifice(s). From a modelling point of view, the thermodynamic state of the air in the bellow and auxiliary chambers is known once the pressures, the volumes and the masses in the chambers at any time are known. In the following we present the mathematical formulation to determine the thermodynamic state.

Dynamics equations of chambers

The reference thermodynamic scheme for air spring with a volume variable auxiliary chamber model is reported in figure 5.2.

Detailing the equation (3.5) for both BC and AC, the pressure in pneumatic volumes are calculated by the following relation respectively:

$$P_{bc}\left(\frac{V_{bc}}{m_{bc}}\right)^{k} = cost. \tag{5.8}$$

$$P_{bc}\left(\frac{V_{bc}}{m_{bc}}\right)^{k} = cost. \tag{5.9}$$

Deriving, equations (5.8) and (5.9) give:

$$\dot{P}_{bc} = \frac{kP_{bc}}{m_{bc}}\dot{m}_{bc} - \frac{kP_{bc}}{V_{bc}}\dot{V}_{bc} \tag{5.10}$$

$$\dot{P}_{ac} = \frac{kP_{ac}}{m_{ac}}\dot{m}_{ac} - \frac{kP_{ac}}{V_{ac}}\dot{V}_{ac} \tag{5.11}$$

Where:

- m_{bc} and m_{ac} are the air mass in BC and AC respectively
- $\dot{m}_{bc} = -\dot{m}_{bc} = G$ is the mass flow-rate and denotes the change of air mass in the chambers.
- V_{bc} is the volume of BC
- V_{ac} is the volume of AC
- $k = c_p/c_v$ is the adiabatic coefficient

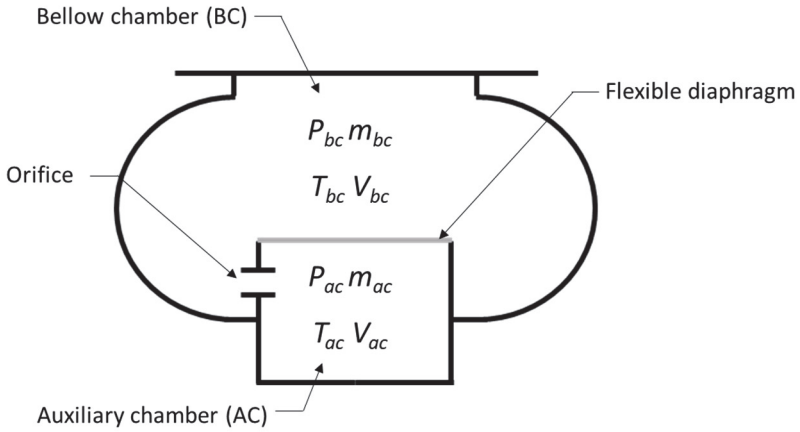

Figure 5.2 Thermodynamic scheme for air spring with a volume-variable auxiliary chamber model.

Equations (5.10) and (5.11) are the thermodynamics equations of bellow and auxiliary chambers. These equations allow to calculate the pressure evolution in both pneumatic chambers in function of the mass flux and volume variation. Thus, for the pneumatic modelling, both SC and AC internal volumes have to be known. Their evaluations must be implemented taking into account that the presence of FD term implies an additive term affecting the volume variation.

Volumes calculation

In regard to the BC, as detailed in paragraph 3.2, we assume that it varies depending only on the air spring height with a linear function and not on the internal pressure. Detailing the expression (3.1) for BC and adding the term due to the presence of FD we have:

$$V_{bc}(t) = V_{bc0} + \frac{dV_{bc}}{dz}(z_2 - z_1) + V_{bc,H} \tag{5.12}$$

Where:

- V_{bc0} is the initial volume of spring chamber
- z_1 and z_2 are the vertical displacements of lower plate and upper plate respectively
- $\frac{dV_{bc}}{dz}(z_2 - z_1)$ is the variation of SC volume assumed linear with the bellow elongation
- $V_{bc,H}$ is the volume occupied as a consequence of the harvester FD deformation

The first two terms of the relation represent the bellow volume calculation found in the references and reported in the paragraph 3.2. The third term instead take into account the presence of the harvester FD in the air spring.

The evaluation of the last term can be made using the superposition principles. We evaluate separately the volume given by the deformation of the FD and caused by the instantaneous pressure difference between the two chambers and the volume given by the deformation of the FD caused by mechanical excitation at the membrane boundaries.

The mathematical formulation of this volume variation can be derived starting from the diaphragm deflection that, in turns, can be evaluated considering Timoshenkos' theory on symmetrical bending of circular plates [102]. When a load, acting on a circular plate (diaphragm), is symmetrically distributed around the axis perpendicular to the plate through its centre, the deflection surface to which the middle plane of the plate is bent will also be symmetrical. In other words, all points equally distant from the centre of the plate have the same deflections. Referring to figure 5.3, we assume the origin of the coordinate system at the centre of the undeflected plate, where r is the radial distance

of points in the middle plane and *a is* the plate radius, for a membrane plate clamped at the edges, we assume the shape deflection z as defined below.

For a uniformly distributed load and, thus, for pressure load:

$$z_{pl}(r,t) = z_{r,pl}(t) \cdot \left(1 - \frac{r^2}{a^2}\right)^2 \tag{5.13}$$

For a concentrated load at the centre, which represents the inertial load at the floating mass associated at base motion load, is:

$$z_{bm}(r,t) = z_{r,bm}(t) \cdot \left(1 - \frac{r^2}{a^2} + 2 \cdot \frac{r^2}{a^2} \cdot \frac{(1+\nu)}{(3+\nu)} \cdot log\frac{r}{a}\right) \tag{5.14}$$

Where $z_{r,pl}$ and $z_{r,bm}$ are the relative displacement of the FD centre, in respect to the FD edges that are integral with the frame (or equivalently with the spring lower plate), for a pressure load and a base motion load respectively.

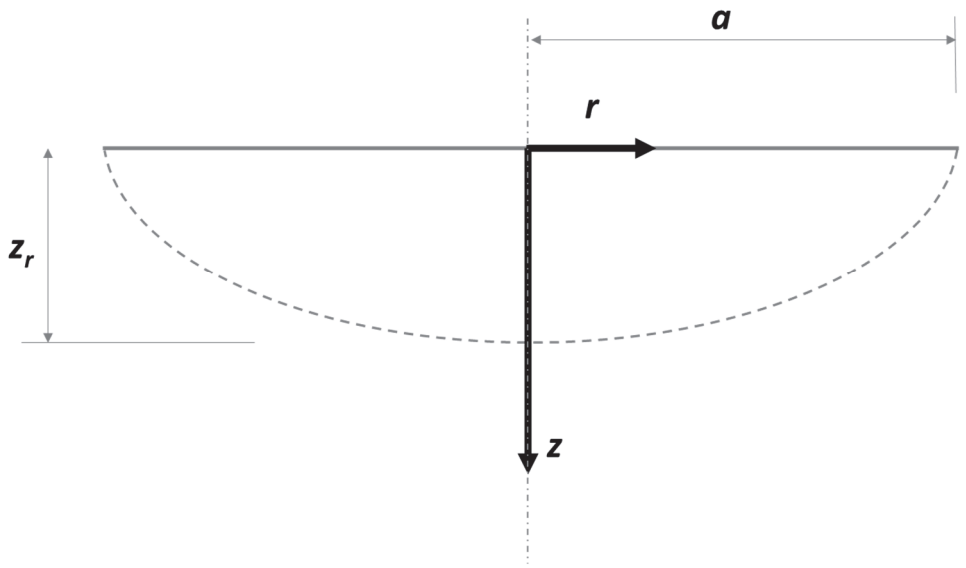

Figure 5.3 Deflection in one diametrical section of flexible diaphragm.

In both cases, the volume occupied by the membrane can be calculated as:

$$V = 2\pi a \int_0^a z\, dr \tag{5.15}$$

Thus, solving the integral (5.15) for expression (5.13) and (5.14), we have that the volume occupied as a consequence of the harvester FD deformation is, for pressure load:

$$V_{sc,H,pl} = \frac{16}{15}\pi a^2 \cdot z_{r,pl} \tag{5.16}$$

And for base motion load:

$$V_{sc,H,bm} = \frac{4}{9}\pi a^2 \left(3 - \frac{(1+\nu)}{(3+\nu)}\right) \cdot z_{r,bm} \tag{5.17}$$

Finally, the volume variation due to the membrane deformation results, applying the superposition method, the sum of the two elements and we can write:

$$V_{sc,H}(t) = V_{sc,H,pl} + V_{sc,H,bm} \tag{5.18}$$

The volume variation $\dot{V}_{ac}$ of AC in equation (5.11) is not equal to zero. This is a departure from what previously seen in literature where the value is usually considered nullable for ACs or tanks. Indeed, the presence of FD implies a variation of the AC volume. Its calculation can be built on the same considerations made for BC. With the difference that the AC initial volume does not change directly as a function of the spring deformation. Thus, the auxiliary volume varies only as a function of the deformation of the harvester membrane. Analogously to expression 5.12, for AC we have:

$$V_{ac}(t) = V_{ac0} - V_{sc,H} \tag{5.19}$$

Where:

- V_{ac0} is the initial volume of auxiliary chamber
- $V_{sc,H}$ is the volume variation due to harvester deformation

The term $V_{sc,H}$ in AC is of opposite sign to that of SC. In fact, when the FD deforms, increasing the SC volume, the AC volume decreases and vice versa.

Mass flow rate calculation: dynamics equations of orifice

The last term necessary to calculate the pressure evolution in both pneumatic chambers is the mass flow rate. We adopt the ISO 6358 [98] formulation detailed in the paragraph 3.2. and here reported for convenience.

$$G = P_1 e\sqrt{\frac{1}{sRT_1}}\sqrt{1-\left(\frac{\frac{P_2}{P_1}-b}{1-b}\right)^2}\cdot sign(P_2-P_1) \qquad \text{if} \qquad {}^{P_2}/_{P_1} > b = 0.518 \qquad (5.20)$$

$$G = P_1 e\sqrt{\frac{1}{sRT_1}}\cdot sign(P_2-P_1) \qquad \text{if} \qquad {}^{P_2}/_{P_1} \leq b = 0.518 \qquad (5.21)$$

5.1.3 Mechanical part (air spring – harvester) modelling summary

The set of equations (5.3), (5.6), (5.10), (5.11), (5.12), (5.19), (5.20) and (5.21) is the air spring-harvester integrated model, this describes both the dynamics of the energy harvester and that of the pneumatic spring, which are mutually influenced. The equations are here reported for convenience:

$$\begin{cases} M(\ddot{z}_3-\ddot{z}_1)+C_{FD}(\dot{z}_3-\dot{z}_1)+K_{FD}(z_3-z_1)+F_{el}=F(t)-M\ddot{z}_1 \\ F(t)=(P_{bc}-P_{ac})\cdot\frac{\pi a^2}{4} \\ \dot{P}_{bc}=\frac{kP_{bc}}{m_{bc}}\dot{m}_{bc}-\frac{kP_{bc}}{V_{bc}}\dot{V}_{bc} \\ \dot{P}_{ac}=\frac{kP_{ac}}{m_{ac}}\dot{m}_{ac}-\frac{kP_{ac}}{V_{ac}}\dot{V}_{ac} \\ V_{bc}(t)=V_{bc0}+\frac{dV_{bc}}{dz}(z_2-z_1)+V_{bc,H} \\ V_{ac}(t)=V_{ac0}-V_{sc,H} \\ G=P_1 e\sqrt{\frac{1}{sRT_1}}\sqrt{1-\left(\frac{\frac{P_2}{P_1}-b}{1-b}\right)^2}\cdot sign(P_2-P_1) \text{ if } {}^{P_2}/_{P_1} > b = 0.518 \\ G=P_1 e\sqrt{\frac{1}{sRT_1}}\cdot sign(P_2-P_1) \text{ if } {}^{P_2}/_{P_1} \leq b = 0.518 \end{cases}$$

This model receives as input the displacement of the lower and upper plates of the pneumatic spring, z_1 and z_2, and returns the dynamics of harvester (in terms of membrane centre displacement z_3, deformed shape of FD) and pressures in chambers. The model allows to evaluate the single effect of base motion and the overall behaviour due to its combination with pressure-induced vibration.

Here it should be pointed out that acting on the number of orifices or their dimension, it is possible to vary the mass flow rate and, consequently, the pressure statement into the two chambers. We consider the two limit conditions: “close” condition that means no orifices between the two chambers (e=0) and “open” connection between chambers (e=infinite). In the first case if the pressure of SC increases, because of volume reduction, there is no mass flow rate between chambers and, thus, their pressure cannot become balanced. In the second case, if the motion of plates is not too fast, it can be considered that the pressure in both chambers is equal at any time. The orifices area is an important design parameter that can vary between “closed” and “open” conditions.

The model has been implemented in the Matlab-Simulink environment and simulations have been performed using the ode45 integrator.

5.1.4 Power extraction consideration

Starting from Williams and Yates [101], many studies assume that the dissipative effect of the energy conversion results in a damping effect. Therefore, the force due to electromechanical feedback F_{el} is modelled as an electrical damping force proportional to the relative velocity between the mass and the frame:

$$F_{el} = C_{el}(\dot{z}_3 - \dot{z}_1) = C_{el}\,\dot{z}_r \tag{5.22}$$

Where C_{el} is the equivalent damping due to electromechanical feedback of the transducer. In this way, in this simplified model, the overall linear viscous damping coefficient can be assumed as composed of a mechanical part (due to the FD characteristics) and an electric part:

$$C = C_{FD} + C_{el} \tag{5.23}$$

This schematisation is suitable for the electromagnetic conversion when a pure resistive electric load is connected, but it results quite approximate for the piezoelectric. However, many interesting considerations about energy conversion may be carried out from the analysis of this model in terms of the maximum amount of power that can be extracted by the mechanical source, as extensively motivated and illustrated by Stephen [103]. Combining relation (5.22) and (5.23) with the equations (5.4) and (5.5) we have respectively for base motion excitation ad pressure-induced vibration:

$$M\ddot{z}_{r,bm} + C\dot{z}_{r,bm} + K_{FD}z_{r,bm} = -M\ddot{z}_1 \tag{5.24}$$

$$M\ddot{z}_{r,pl} + C\dot{z}_{r,pl} + K_{FD}z_{r,pl} = (P_{bc} - P_{ac}) \cdot \frac{\pi a^2}{4} \quad (5.25)$$

The instantaneous power transfer to the mass is, for each load case, the product of the force on the mass and its absolute velocity. So, for base motion case:

$$W_{input,bm}(t) = -M\ddot{z}_1 \cdot (\dot{z}_{r,bm} + \dot{z}_1) \quad (5.26)$$

Remembering that only for pressure-induced vibration, z_1 and its derivatives are null and thus $z_{r,pl}$ and its derivatives are equals to z_3 and its derivatives, in this case the power transfer to the mass is:

$$W_{input,pl}(t) = F \cdot \dot{z}_{r,pl} = (P_{sc} - P_{ac}) \cdot \frac{\pi a^2}{4} \cdot \dot{z}_{r,pl} \quad (5.27)$$

For the superimpose principle, according to relation (5.7), the overall instantaneous power transfer to the mass can be expressed as follow:

$$W_{input}(t) = (-m\ddot{z}_1 + F) \cdot (\dot{z}_{r,bm} + \dot{z}_{r,pl} + \dot{z}_1) = (-m\ddot{z}_1 + F) \cdot (\dot{z}_r + \dot{z}_1) \quad (5.28)$$

From this amount of power, only the fraction dissipated and/or absorbed by the damper can be extracted from the mechanical part for the electrical domain.

The instantaneous power extractable from the device is for the base motion case, the pressure-induced vibration and for the combination of the two respectively:

$$W_{extr,bm}(t) = C \cdot \dot{z}_{r,bm}^2 \quad (5.29)$$

$$W_{extr,pl}(t) = C \cdot \dot{z}_{r,pl}^2 \quad (5.30)$$

$$W_{extr}(t) = \left[C \cdot \dot{z}_{r,bm} + C \cdot \dot{z}_{r,pl}\right] \cdot [\dot{z}_{r,bm} + \dot{z}_{r,pl}] = C \cdot \dot{z}_r^2 \quad (5.31)$$

It should be emphasised that the expressions (5.26), (5.27) and (5.28) refer to the flow of power from the environment into the device. Equations (5.29), (5.30) and (5.31) express the power extractable from the input and refer to the instantaneous power dissipated by mechanical damping or transferred to electrical domain and not the one delivered to the electrical load. As demonstrated by Stephen in [103], both mechanical and electrical contributions of damping participate in energy transfer from the environment to the system and both to it dissipation/harvesting. In particular, the mechanical contribution due to FD, C_{FD} plays both a beneficial and dissipative role but it cannot contribute more energy than it dissipates.

In case of a harmonic excitation and for the only base motion mechanism, the theoretic steady state solution is known. Thus, for FD centre, the solution of eq. (5.24) is:

$$z_{r,bm} = Z_{r,bm}\sin(\omega t - \varphi_{bm}) \tag{5.32}$$

Where

$$Z_{r,bm} = \frac{M\omega^2 Z_1}{\sqrt{(K_{FD}-M\omega^2)^2+C^2\omega^2}} \tag{5.33}$$

is the amplitude of relative diaphragm deflection.

The average power absorbed by the equivalent damper is:

$$W_{extr,bm,av} = \frac{1}{2}C \cdot \omega^2 Z_{r,bm}^2 \tag{5.34}$$

Considering the pressure load, it can be supposed harmonic with the same frequency of input displacement, being the bellow volume function of relative displacement between the plates. Thus, for FD centre, the solution of eq. (5.25) is:

$$z_{r,pl} = Z_{r,pl}\sin(\omega t - \varphi_{pl}) \tag{5.35}$$

In which

$$Z_{r,pl} = \frac{M\omega^2 F}{\sqrt{(K_{FD}-M\omega^2)^2+C^2\omega^2}} \tag{5.36}$$

The average power absorbed by the equivalent damper is:

$$W_{extr,bm,av} = \frac{1}{2}C \cdot \omega^2 Z_{r,bm}^2 \tag{5.37}$$

If the force deriving from the base motion inertial load and the force due to the pressure oscillation have the same timing, the phase angle in equation (5.32) and (5.35) are the same ($\varphi_{pl} = \varphi_{bm} = \varphi_{pl}$). Therefore, the two amplitudes of relative displacements can be added and the average power absorbed by the equivalent damping becomes:

$$W_{extr,av} = \frac{1}{2}C \cdot \omega^2 \left(Z_{r,bm} + Z_{r,pl}\right)^2 = \frac{1}{2}C \cdot \omega^2 Z_r^2 \tag{5.38}$$

Comparing equation (5.34) and (5.38) we note that, if the two excitation mechanisms, the base-motion and pressure-induced vibration, act with the same frequency and the same timing the amplitude of the harvester relative displacement increases, leading at

an increment of average power extractable from the input. On the contrary not-in-phase action could lead to a reduction of power extractable. The proposed model (see paragraph 5.1.3) gives an instrument to evaluate the combination of the excitation mechanism.

Base motion vs. combined action simulation results

In order to preliminary evaluate the effects of the double excitation mechanism the dynamic behaviour of the system and the extractable power have been evaluated in simulation. Results are carried out under the simplified assumption of harmonic motion of lower plate, considering the upper plate fixed (z_2=0). An 8 Hz, 10 mm in amplitude, sinusoidal load has been applied. The device behaviour has been evaluated for two different conditions: in the first one, just the base motion mechanism has been exploited; in the second one, also the pressure-induced vibration has been taken into account. The first condition represents the aforementioned open connection between the two chambers. Furthermore, the influence of the orifices dimensions has been evaluated. At this stage, we want to remark that it is tempting, but quite wrong, to consider also the case of the only pressure-induced vibration. In fact, the pressure gradient between the two chambers occurs because of base vibrations.

In the table 5.1 the general data of the air spring and of the harvester used in the simulation are reported. As a result, the natural frequency of the FD is 7.67 Hz and the static deflection of diaphragm centre is 4 mm.

Replacing in equation (5.33) and (5.34) the data in the table, we have $Z_{r,bm}$ =16.6 mm and $W_{av} = 3.73\ W$. These theoretical results have been compared with simulations ones in order to verify the model. In figure 5.4 and 5.5, the relative displacement of FD centre and the extractable power are plotted for both cases: base motion on its own and the combination between base motion and pressure-induced vibration. There, it could be observed that, after the transient period (≅ 0.4 s), the values of average power and FD centre displacement amplitude for solo base motion are in accordance with theoretical calculation.

From diagrams is quite evident how the combination of excitation mechanisms causes a consistent increment of the membrane centre displacement and, thus, of extracted power. In particular, the mass displacement amplitude is $Z_{r,bm}$ =33.5 mm and the average extractable power become $W_{av} = 15\ W$.

Table 5.1 Main parameters for mechanical part simulation

Parameter	description	value	
Air spring			
$V_{sc,0}$	Initial Air spring chamber volume	0.015	m^3
$V_{ac,0}$	Initial auxiliary chamber volume	0.001	m^3
P_{atm}	Atmospheric pressure	0.101	MPa
$P_{sc,0}$	Spring chamber initial pressure	0.7	MPa
$P_{ac,0}$	Auxiliary chamber initial pressure	0.7	MPa
$\frac{dV_{sc}}{dz}$	linear coefficient air spring volume variation	0.12	-
Flexible diaphragm			
a	Diaphragm radius	82	mm
K_{FD}	vertical stiffness of FD	0.93	N/mm
M	Tuning mass	0.4	Kg
ξ	Damping ratio	0.3	-
e	orifice effective area	100	mm^2

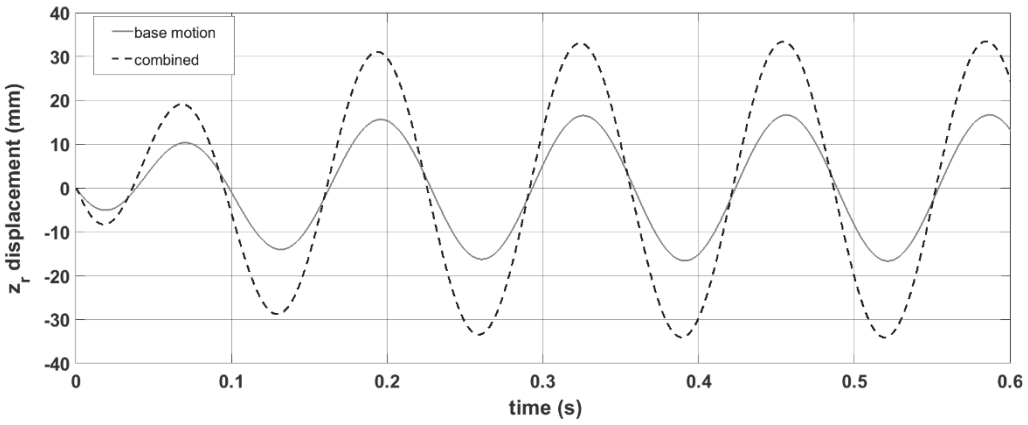

Figure 5.4 Comparison between results obtained exploiting only base motion source and the combined sources in terms of FD centre displacements.

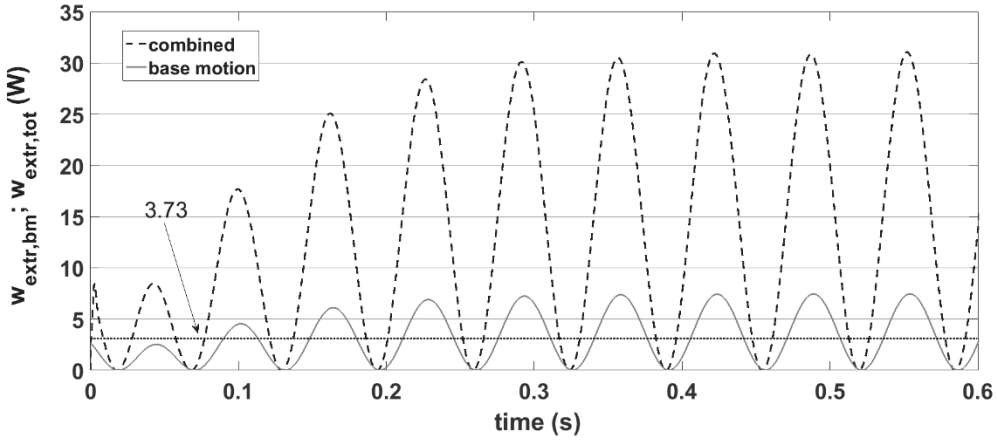

Figure 5.5 Comparison between results obtained exploiting only base motion source and the combined sources in terms of extractable power.

Orifices dimension analysis

A parametric study was performed to investigate the effects of orifices number and dimension on the device. Several simulations were conducted varying the single orifice effective area and, furthermore, increasing the orifices number. Figure 5.6 depicts the pressure difference between BC and AC under prescribed sinusoidal load and for various orifices dimension. There it could be observed that, after the initial transient, for one orifice with effective area included between 50 mm^2 and 200 mm^2 there is a small variation in terms of pressure difference evolution. Further increasing the global effective area by means of greater orifices number, the gradient between chambers becomes smoothest and the peak value decreases tending to zero, which represents the chambers open connection state. According to eq. (5.6), a smaller value of pressure difference means a littlest excitation force on mass. As shown in figure 5.6 this implies a reduction of FD overall deflection tending to only base motion vibration behaviour. Here it should be remarked that if on one hand a little pressure difference between chambers means less power extraction, on the other hand orifices should guarantee pressure equilibrium achievement between BC and AC for the device operation. Furthermore pressure gradient should not overcome the limit imposed by geometric constraint and FD strength.

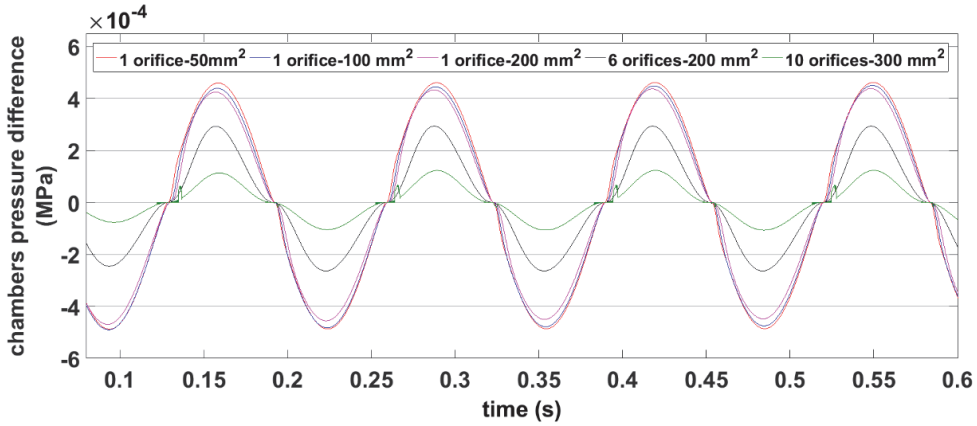

Figure 5.6 Pressure difference between BC and AC for different orifices dimension.

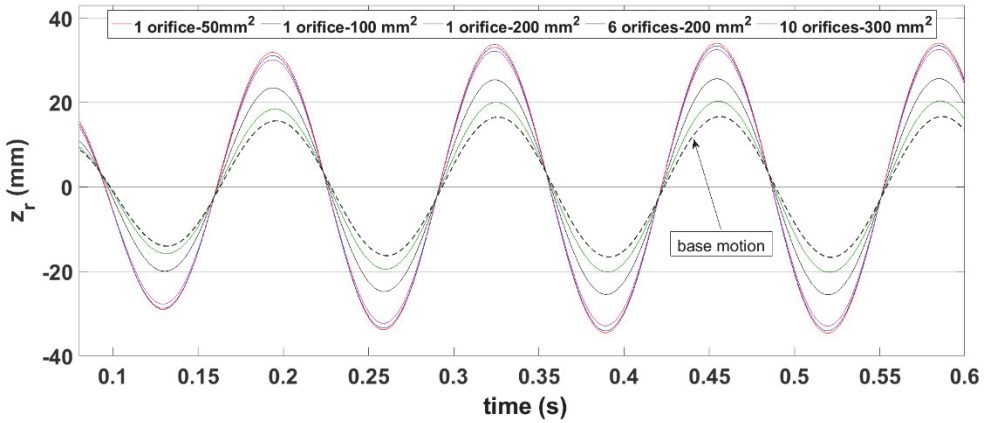

Figure 5.7 Flexible diaphragm centre deflection in function of orifices dimension.

To sum up the modelling activity of the mechanical part, the harvester has been designed to have its undamped natural frequency around an excitation input frequency. Numerical results show that appropriately combining the base motion excitation with the pressure-induced vibration, the displacement of the FD centre significantly increases and therefore increase the power flow into the device and the extractable power. Furthermore, the orifices that connect BC with AC play a fundamental role in the excitation mechanism combination and the model is sensitive to their number and dimensions. With a variation of the global orifices effective area, it is possible to act on chambers pressure difference. Increasing this parameter, the pressure difference decreases to the point of an open connection condition, this is representative of the only base motion excitation state.

5.2 Piezoelectric transduction mechanism

5.2.1 Generalities

The coupling between the mechanical and the electrical domain is performed by means of the transducer. This element performs the energy conversion from mechanical energy into an electrical one by establishing a relation between force and velocity and between voltage and currents. The converting relations are dependent on the type of transducer (piezoelectric, electromagnetic or electrostatic), its layout and operating conditions. Here a piezoelectric transduction mechanism is considered.

Piezoelectrics are the class of dielectric materials that can be polarized, in addition to the action of an electric field, also by the application of a mechanical stress. This unusual property, exhibited by a few dielectric materials, is called piezoelectricity [47].

To transform the mechanical energy into electrical energy the so called direct piezoelectric effect is exploited, which is the generation of an electric charge as a result of a force exerted on the material. Some materials also show the inverse piezoelectric effect: an electric field applied across the electrodes produces mechanical deformation or strain in the material. This way of transforming the electric energy into usable mechanical energy is used for actuation applications.

Nowadays, piezoelectric materials are commercially employed in sensors and actuators and represent a promising and concrete way in the kinetic energy harvesting field.

Typical piezoelectric materials are crystal materials such as quartz and ceramics such as lead zirconate titanate (PZT). They can be of two types: piezo-polymer in which the piezoelectric material is immersed in an electrically passive matrix (for instance PZT in epoxy matrix) and piezo-composites that are composite materials made by two different ceramics. A recent discovery found that the proprieties of polyvinylidene (PVDF), that is a ferroelectric polymer, exhibit piezoelectric and pyroelectric properties.

A peculiarity of these materials is that the piezoelectric characteristics show a strongly anisotropic behaviour. Therefore, the piezoelectric behaviour depends on the direction of the applied mechanical strain and on the direction of the resulting polarisation. A more thorough analysis of piezoelectricity can be found in [47], [104].

5.2.2 Piezoelectric effect modelling

In this section, we introduce the linear constitutive equations that describe electromechanical properties of piezoelectric materials largely used in energy harvesting applications. The formalization is based on the IEEE standard for piezoelectricity [105] which is widely accepted as being a good representation of piezoelectric material properties:

$$\begin{pmatrix} \mathbf{S} \\ \mathbf{D} \end{pmatrix} = \begin{pmatrix} \mathbf{s}^{\mathbf{E}} & \mathbf{d}^{\boldsymbol{T}} \\ \mathbf{d} & \mathcal{E}^{\sigma} \end{pmatrix} \begin{pmatrix} \boldsymbol{\sigma} \\ \mathbf{E} \end{pmatrix} \tag{5.39}$$

Where **S** is the mechanical strain, **σ** is the mechanical stress, **D** is the electric charge displacement, **E** is the electrical field, $\mathbf{s}^{\mathbf{E}}$ is the elastic compliance under a zero or constant electric fields (indicated by the superscript E), $\boldsymbol{\mathcal{E}}^{\sigma}$ is the dielectric permittivity under a zero or constant stress (indicated by the superscripts). **d** and $\mathbf{d}^{\mathbf{T}}$ are the matrices for the direct and the reverse piezoelectric effect, where the superscript **T** means the transposed matrix. Equations (5.39) describe both the reverse and the direct piezoelectric effect. If the coupling terms **d** and $\mathbf{d}^{\mathbf{T}}$ are neglected, these equations becomes the uncoupled constitutive equations of an elastic dielectric material.

Although in energy harvesting applications the direct piezoelectric effect is exploited, the reverse effect is even so present and influences the dynamics of the mechanical part of the system. Therefore, the forward and backward effects must be considered for a complete description of the system.

Being the piezoelectric material behaviour strictly anisotropic it can be used in various ways. However, In EH practical applications there are two common modes utilized for piezoelectric energy harvesting: 33-mode and 31-mode. In this notation, the first number indicates the voltage direction, while the second indicates the direction along which the stress is applied. Thus, in 33-mode the direction of applied stress (force) and generated voltage is the same, while in 31-mode the stress is applied in axial direction but the voltage is obtained from perpendicular direction (figure 5.8). In both cases, voltage is applied along the direction 3; this means that electrodes are attached to the bottom and upper surfaces of piezo material that have as a normal this axis.

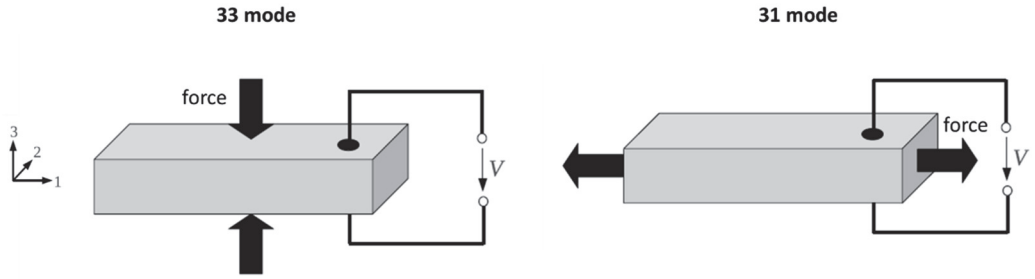

Figure 5.8 Piezoelectric material in 33 and 31 operating mode

For the proposed EH system the piezoelectric patches work in 31-mode (see paragraph 3.3). For 31 mode, the constitutive equations (5.39) can be simplified in one dimension:

$$S_1 = s_{11}^E \cdot \sigma_1 + d_{31} \cdot E_3 \tag{5.40}$$

$$D_3 = d_{31} \cdot \sigma_1 + \varepsilon_{33}^\sigma \cdot E_3 \tag{5.41}$$

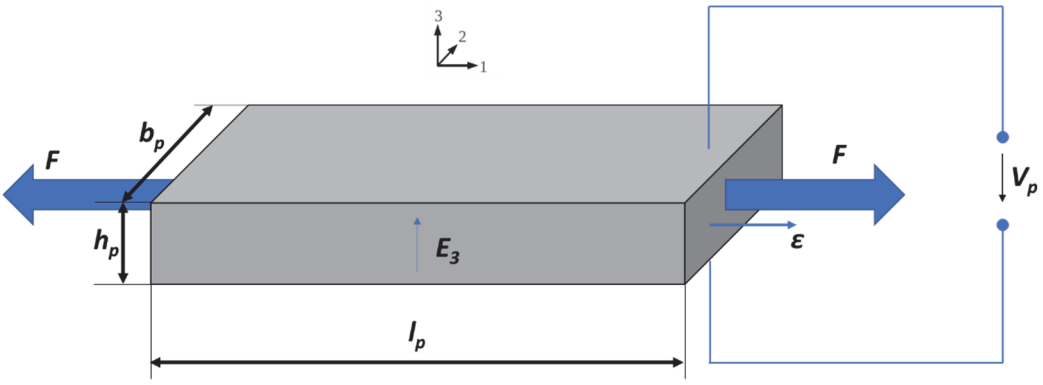

Figure 5.9 Piezoelectric material patch used as energy harvester in the 31 mode

We refer to the piezoelectric patch working in 31-mode as show in figure 5.9. The force *F* acting on the material causes an elongation ε in the direction 1. Therefore, the piezoelectric effect implies the generation of a voltage V_p in the direction 3. In turn, if a circuit is connected, a current *i* is induced. Using the relations:

$$E_3 = -\frac{V_p}{h_p}; \qquad q = D_3 l_p b_p; \qquad \sigma_1 = \frac{F}{h_p b_p}; \qquad S_1 = \frac{\varepsilon}{l_p}; \qquad i = \frac{dq}{dt} \tag{5.42}$$

where q denotes the charge. The constitutive (5.40) and (5.41) can be rewritten in terms of the macroscopic variables *F, ε, V_p* and *i* , instead of the local variables [106]:

$$\begin{cases} F = K_p\varepsilon + \Gamma V_p \\ i = \Gamma\dot{\varepsilon} - C_p\dot{V}_p \end{cases} \tag{5.43}$$

Where

$$K_p = \frac{b_p h_p}{l_p s_{11}^E}\ ;\ C_p = \left(\varepsilon_{33}^{\sigma} - \frac{d_{31}^2}{s_{11}^E}\right)\frac{b_p l_p}{h_p};\ \Gamma = \frac{d_{31} b_p}{s_{11}^E} \tag{5.44}$$

where K_p is the axial stiffness of the piezoelectric patch along direction 1, C_p is the piezoelectric output capacitance along direction 3, Γ is the force-voltage factor or the generalized electromechanical coupling factor (GEMC) [107]. From the first equation of (5.43), the force F is composed by the elastic force $K_p\varepsilon$, that depends on the material mechanical characteristics, and the coupling force ΓV_p, which depends on the voltage across the piezoelectric material. Due to the balance of forces, F can be considered as the restoring force F_e acting on the seismic mass.

The outgoing current of the piezoelectric element *i* consists of a contribution $\Gamma\dot{\varepsilon}$ due to the mechanical behaviour and related to the time derivative of the elongation along direction 1, and a contribution $C_p\dot{V}_p$ related to an equivalent capacitance between the electrodes. Considering a parasitic resistance R_L, another possible contribution is given by the dielectric losses V_p/R_L but normally the resistance presents a very large value and this contribution is negligible.

From equations (5.43) it should be noted that for a given mechanical excitation, the larger Γ is the more energy is generated in the electrical domain. Vice versa, the same mechanical energy leads to only little useable electrical energy for a lowly coupled factor. On Γ also depends the magnitude of the feedback that the electrical part has on the mechanical.

According to the IEEE Standards on Piezoelectricity, a measure of the piezoelectric patch ability to convert mechanical energy into electrical one when used in 31 mode, independently from geometric dimension, is given by the squared piezoelectric material coupling factor k_{31}^2:

$$k_{31}^2 = \frac{d_{31}^2}{\varepsilon_{33}^{\sigma} s_{11}^E} \tag{5.45}$$

The material coupling factor can be expressed as a function of the generalized electromechanical coupling factor (GEMC) Γ , which depends on the geometry of the patch, by considering equations 5.44:

$$k_{31}^2 = \frac{\Gamma^2}{k_p C_p} \tag{5.46}$$

5.3 Electrical part

The energy produced by the generator has to be managed and transferred to the electric load. This task is performed by the electrical part of the EH system. Usually the AC voltage and current induced by the piezoelectric transducer are neither suitable for electronics supply nor for energy storage, so several power processing steps are necessary. Generally, the current is rectified with an AC/DC converter, and a DC/DC converter is used to regulate the voltage to make it compliant to the storage element or the electric load requirements.

In this work, we refer to a simplified and common approach that consists in considering a linear circuit by replacing the extraction circuit by an equivalent linear input impedance [108],[109]. A resistor R is then connected to the generator and the harvested power is defined as the power dissipated into the resistive load R. This means that the induced current is deduced from following relation:

$$V_p = Ri \tag{5.47}$$

Recovery performance are dependent on R and, thus, it is adapted to maximise power harvesting. This model does not take into account the losses in the converters, thus the calculated power is overestimated in comparison with a practical case.

Although in the practical implementation of the EH device, the electric load represented by a resistor R, cannot be directly connected to the transducer because a stabilised DC voltage is required, here we limit the analysis at this point, referring to future development for the implementation of power management strategies.

Generally, there is a poor coupling between the mechanical and electrical domains of the piezoelectric material. This means that the force due to the voltage at the transducer terminals is low and the oscillation amplitude of the tip-mass is due almost exclusively to the mechanical parasitic damping rather than the electrical loading. As a consequence, it can be shown [110] that the maximum power that can be dissipated in a linear load resistance occurs when the load resistance is given by:

$$R = R_{opt} = \frac{1}{\omega C_p} \tag{5.48}$$

From the relation it is clear that the potential recovered power is limited by the clamped capacitance of the piezoelectric patch.

Through the implementation of power management strategies, it is possible to act on the electromechanical coupling of the system to influence the energy conversion performance.

5.4 Multi-physical model of energy harvester

In the previous paragraphs the mathematical formulations of the three main parts constituting the EH system (mechanical, the transducer and electrical) were analysed separately. In this paragraph we merge the three domains together to form a global simplified model of the energy harvester integrated in the air spring that take into account the mechanical excitation, the thermodynamic state evolution of the air inside the c air spring chambers and the electromechanical coupling.

According to the description of the harvesting system in paragraph 3.3 we refer to the following configuration: n rectangular piezoelectric films arranged in a radial pattern on the upper surface of the FD as depicted in figure 5.10. For explanatory purpose in the figure are shown four piezoelectric patches, which are considered perfectly bounded with the FD and the tuning mass. Each piezoelectric element is anchored at one end to the FD rigid frame and is free to move along the vertical direction to the other end.

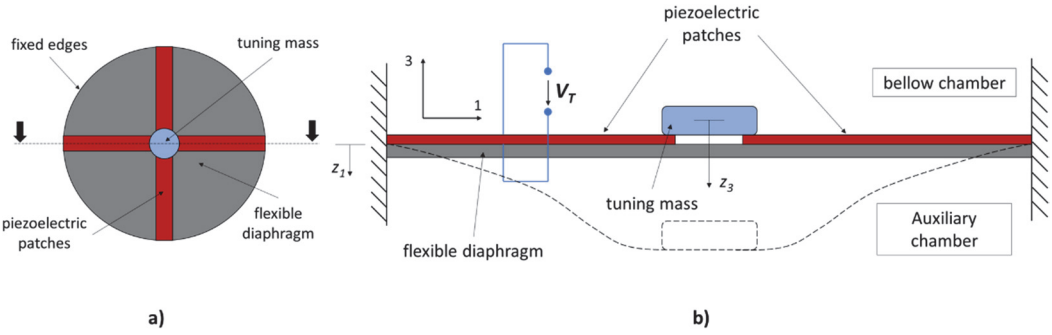

Figure 5.10 Piezoelectric EH in radial pattern based on FD: a) top view and b) enlarge schematic section view.

When a mechanical input acts at the bellow lower plate along the vertical direction, the FD vibrates. As a consequence of the tuning mass displacement (FD centre deflection), the FD deforms and, thus, strain is induced into the piezoelectric patches.

Being the piezoelectric patches very thin, strains are considered as traction/compression along the direction 1 of the piezoelectric elements. Electrodes are applied along the direction 3 and so piezoelectric elements work in 31 mode. The dynamic input induces, by means of the transducer, an AC current exploiting the piezoelectric direct effect and, if the transducer terminals are not short-circuited, a voltage is generated. Vice-versa the voltage at the transducer terminal, by the piezoelectric reverse effect, induces mechanical stress on the piezoelectric patch along the direction 1. As a consequence of the shift of the piezoelectric patch, with respect to the neutral surface of the support diaphragm, the voltage produces a force along the direction z_3 at the patches free-end. As a result of the FD vibrating at the first mode a resonance occurs. Furthermore, at the same time, the force due to pressure gradient between the chambers acts on it. If the two actions are in phase the largest strain is induced on the piezoelectric elements and more energy is generated in the electric circuit. This operating condition is the most convenient for energy harvesting purposes. As debated in chapter 4 the system has a poor modal density and thus a clear separation between the first and the following modes is present. The first mode well describes the FD behaviour when it is excited around the corresponding frequency or the mass freely oscillates after a shock. In this assumption, the integrated energy harvesting system can be modelled as shown in figure 5.1.

Here it should be noted that in the piezoelectric EH modelling the equations 5.43 cannot be directly implemented to describe the electromechanical coupling of the system. These equations refer to the macroscopic variables, force and elongation, acting along direction 1 of the piezoelectric element. In the analysed system, we need to relate the electric variable to forces and displacements acting along the z axis.

In the proposed EH system, the displacement of the FD centre along the z axis, due to the geometric and constraining characteristics of the system, induces an elongation along the direction 1 of the piezoelectric patch. Therefore, elongation velocity induces current. Vice versa, the force F along direction 1, due to the geometric characteristics of the system produces a force F_T (transducer force) applied to FD centre along the z axis.

Furthermore, looking at the geometrical layout of the system we can consider the elongation of the piezoelectric patch as a sum of two contributions, bending and traction:

$$\varepsilon = \varepsilon_b + \varepsilon_t \tag{5.49}$$

Indeed, due to the axial symmetry of the system, the floating mass can move only along z direction and considering the perfect bonding between all elements, the piezoelectric patches result bent and stretched at the same time (see figure 5.10).

Therefore, it is necessary to link the force *F* and the elongation speed $\dot{\varepsilon}$ of equations 5.43 to the force F_T and the relative velocity $\dot{z}_r$ acting in the mechanical model.

Simplified relations to determine F_T and the two elongation contributes can be found as follows.

- *Transducer vertical force F_T*

  When a voltage is applied to the piezoelectric patch along the direction 3, a force F is produced along the direction 1 due to piezoelectric 31 effect. Considering that there is a distance Δh between the patch neutral surface and neutral surface of the support FD, each piezoelectric layer imposes a moment $F\Delta h$ to the FD. The equilibrium of the system is achieved applying a force F_T at the FD centre that generates a moment $F_T\, l_p$ that opposes $F\Delta h$ (figure 5.11). similarly to what is described in [42] the relation between *F* and F_T is derived as follows.

$$F_T \frac{l_p}{2} = F\Delta h \implies \tag{5.50}$$

$$F_T = \frac{2\Delta h}{l_p} F = -AF \tag{5.51}$$

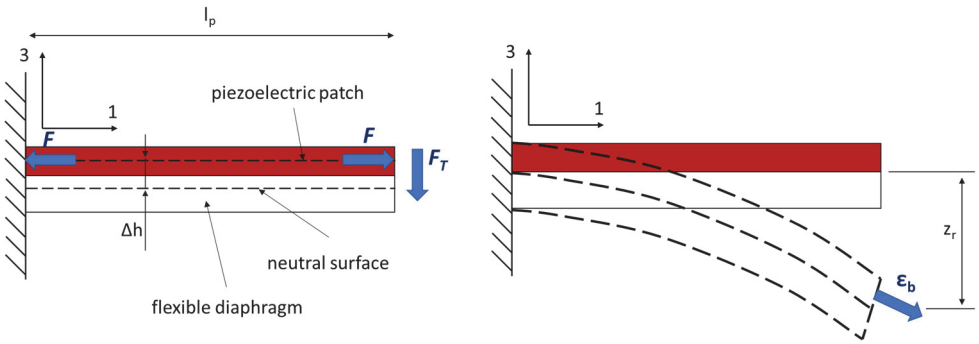

Figure 5.11 Simplified scheme for the calculation of piezoelectric element elongation due to bending.

- *Elongation bending part*

This part can be calculated in first approximation considering the piezoelectric element as a cantilever beam at distance *Δh* from the bending neutral surface due to the presence of FD (figure 5.11). In this simplified configuration, a displacement *z*, imposed to the free-end of the piezoelectric beam, induces a curvature to the neutral surface. Being F_T the load at the free edge the curvature of neutral axis is:

$$\frac{d^2 z_r}{dx^2} = \frac{F_T}{K_{flex}}(l_p - x) \tag{5.52}$$

Where K_{flex} is the flexural rigidity of the equivalent layered cantilever beam composed by the piezoelectric electric element end the corresponding FD part. The maximum deflection of the beam at the free end, z_r is:

$$z_r = \frac{F_T \, {l_p}^3}{3K_{flex}} \tag{5.53}$$

From this it is possible to obtain F_T to be replaced in (5.50). The average strain is obtained integrating $S_1(x)$ along the piezoelectric patch:

$$S_1(x) = \Delta h \frac{d^2 z_r}{dx^2} = \Delta h \frac{3}{{l_p}^3} z_r (l_p - x) \tag{5.54}$$

$$S_1 = \Delta h \frac{d^2 z_r}{dx^2} = \int_0^{l_p} \Delta h \frac{3}{{l_p}^3} z_r (l_p - x) dx = \frac{3\Delta h}{2{l_p}^2} z_r \tag{5.55}$$

The piezoelectric element elongation due to the bending is:

$$\varepsilon_b = S_1 l_p = \; l_p \frac{3\Delta h}{2{l_p}^2} z_r = \; -B z_r \tag{5.56}$$

Thus, the elongation velocity is:

$$\dot{\varepsilon_b} = -B \dot{z}_r \tag{5.57}$$

- *Elongation traction part*

This contribute is calculated referring to the scheme in figure (5.12). One end of the piezoelectric element is considered simply supported, to avoid flexural deformation, and at the other end (the one integral with the mass), is free to move along z and restrained in other directions.

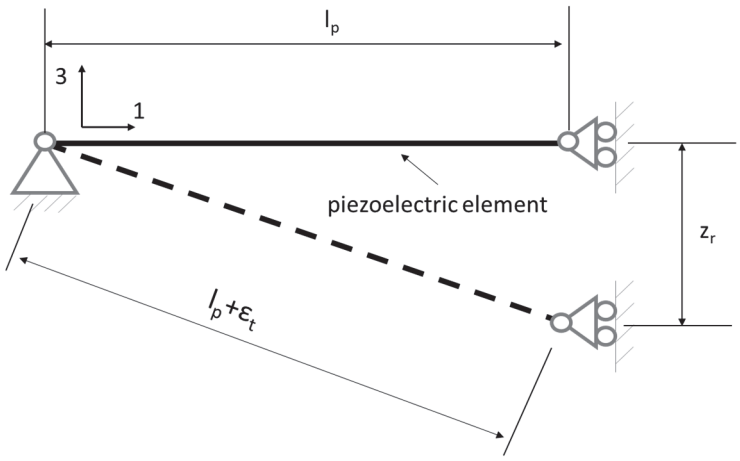

Figure 5.12 Simplified scheme for the calculation of piezoelectric element elongation due to traction.

Thus we can write:

$$(\varepsilon_t + l_p)^2 = {l_p}^2 + {z_r}^2 \Longrightarrow {\varepsilon_t}^2 + 2l_p\varepsilon_t - {z_r}^2 = 0 \tag{5.58}$$

Solving the quadratic equation and noting that the solution with the *minus* it is not acceptable for our geometry, the elongation is:

$$\varepsilon_t = -l_p + \sqrt{{l_p}^2 + {z_r}^2} \tag{5.59}$$

Deriving this relation, the elongation velocity is:

$$\dot{\varepsilon_t} = \frac{z_r \dot{z}_r}{\sqrt{l_p^2 + z_r^2}} = -J\frac{z_r \dot{z}_r}{\sqrt{l_p^2 + z_r^2}} \tag{5.60}$$

Therefore, the force *F* and the elongation speed $\dot{\varepsilon} = \dot{\varepsilon_b} + \dot{\varepsilon_t}$ of equations 5.43 are linked to the force F_T and the relative velocity $\dot{z}_r$ acting in the mechanical model by means of three coefficients A, B and J:

$$F_T = -AF \tag{5.61}$$

$$\dot{\varepsilon_b} = -B\dot{z}_r \tag{5.62}$$

$$\dot{\varepsilon_t} = -J\frac{z_r \dot{z}_r}{\sqrt{l_p^2 + z_r^2}} \tag{5.63}$$

These coefficients depend on the geometry configuration of the system. For a more detailed determination of these coefficients a suitable way is represented by the parameters identification via an experimental test.

The formulation (5.43) is deduced from the constitutive equations of the piezoelectric material, thus no mechanical dissipative effect is considered for the piezoelectric element. As this contribute is negligible, it doesn't add any complexity when considered as part of the model. Thus, we add the dissipative term $C_{mp}\dot{\varepsilon}$ to the expression of the force *F* in equations (5.43), where C_{mp} is the mechanical damping of a piezoelectric element. The coupling equations of the piezoelectric patch in 31 working mode, equations (5.43), become the equations of the piezoelectric transducer consisting of one piezoelectric patch bonded on the FD:

$$\begin{cases} F_T = -AF = -A\left(K_p\varepsilon + C_{pm}\dot{\varepsilon} + \Gamma V_T\right) = K_{p\_eq}\varepsilon + C_{mp\_eq}\dot{\varepsilon} + \alpha V_T \\ i_T = \Gamma\dot{\varepsilon} - C_p\dot{V}_T = \Gamma\dot{\varepsilon_b} + \Gamma\dot{\varepsilon_t} - C_p\dot{V}_T = -\beta\dot{z}_r - \gamma\frac{z_r\dot{z}_r}{\sqrt{l_p^2+z_r^2}} - C_p\dot{V}_T \end{cases} \tag{5.64}$$

where F_T is the force acting on the tuning mass along z direction due to the piezoelectric element, k_{p_eq} and C_{mp_eq} are the equivalent mechanical stiffness and damping of the piezoelectric patch when its behaviour is referred to the relative displacement of the mass. i_T and V_T are the output current and voltage of the transduction mechanism. α, β and γ are the electromechanical coupling coefficients of the transducer. α refers to the backward piezoelectric effect, while β and γ refer to the forward one. C_p is the aforementioned clamped capacitance.

Finally, considering equations (5.53) for transduction mechanism, the formulation model of mechanical part (5.3), and equation (5.47) for electrical part, the governing equations of the EH system are:

$$\begin{cases} M(\ddot{z}_3 - \ddot{z}_1) + C_m(\dot{z}_3 - \dot{z}_1) + K_m(z_3 - z_1) + nF_{el} = (P_{bc} - P_{ac})\frac{\pi a^2}{4} - M\ddot{z}_1 \\ i_T = -\beta\dot{z}_r - \gamma\frac{z_r\dot{z}_r}{\sqrt{l_p^2+z_r^2}} - C_p\dot{V}_T \\ F_{el} = -\alpha V_T \\ i_T = {V_T}/{R_L} \end{cases} \tag{5.65}$$

where $z_1, \dot{z}_1, \ddot{z}_1$ refer to the displacement of air spring lower plate, $z_3, \dot{z}_3, \ddot{z}_3$ to the floating mass at FD centre; $z_r = (z_3 - z_1), \dot{z}_r, \ddot{z}_r$ to the relative displacement of the mass with respect to the lower plate, F_{el} is the force due to the reverse piezoelectric effect; n is the number of piezoelectric patches; $(-\beta\dot{z}_r - \gamma\dot{z}_r)$ is the current due to the forward

piezoelectric effect; $P_{bc}$and $P_{ac}$are the pressure in the bellow and auxiliary chamber respectively; *M* is the tuning mass; R_L is the resistive load . With regard to the parameters $K_m$and C_m they are respectively the overall mechanical stiffness and the overall mechanical damping of the system defined as:

$$K_m = nK_{p\_eq} + K_{FD} \tag{5.66}$$

$$C_m = C_{mp\_eq} + C_{FD} \tag{5.67}$$

The piezoelectric transduction coefficients α, β and γ relate the generalised coupling factor of the piezoelectric patch to the mechanical proprieties of the EH system:

$$\alpha = A\Gamma \tag{5.68}$$

$$\beta = B\Gamma \tag{5.69}$$

$$\gamma = G\Gamma \tag{5.70}$$

These coefficients extend the meaning of Γ when a harvester is interposed between the vibrating system and the piezoelectric transducer. In our case the harvester is the FD that relates the stress along direction 1 of the piezoelectric patch to the vibrations along z direction through the coefficients A, B and G..

5.4.1 Power conversion considerations

By multiplying the first of equations of (5.65) by $\dot{z}_r$ and the second by V_T , the power balance of the mechanical part and of the electrical side is derived:

$$\underbrace{M\ddot{z}_r\dot{z}_r}_{kinetic} + \underbrace{C_m{\dot{z}_r}^2}_{damping} + \underbrace{K_m z_r\dot{z}_r}_{elastic} + \underbrace{n(-\alpha V_T)\dot{z}_r}_{piezoelectric} = \underbrace{[(P_{bc} - P_{ac})\frac{\pi a^2}{4} - M\ddot{z}_1]\dot{z}_r}_{input} \tag{5.71}$$

$$\underbrace{V_T i_T}_{output} = \underbrace{-\beta\dot{z}_r V_T - \gamma\frac{z_r\dot{z}_r}{\sqrt{l_p^2 + z_r^2}}V_T}_{converted} \underbrace{- C_p\dot{V}_T V_T}_{capacitance} \tag{5.72}$$

From equation (5.71) we can see that the input power of the system, which is the power extracted from the source and delivered to the harvester, is equal to: the kinetic power of the floating mass, the elastic power stored in the mechanical elements, the power wasted for mechanical damping and the overall power delivered to the electric part of the system through the piezoelectric element. The power balance of electrical side,

equation (5.72), shows that the output power for each piezoelectric element, which is the electric power provided to the electrical part of the system, consists in the converted power from the mechanical domain minus the power stored in the clamped capacitance of the piezoelectric patch.

5.5 Conclusion

In this chapter, a multi-physical model of a new kinetic energy harvester architecture integrated in a pneumatic spring has been proposed. The three main parts constituting the EH system, the mechanical, the transducer and the electrical, has been analysed separately and then merged together in the global simplified model whose mathematical formulations are expressed by the set of equations (5.65). This model, receiving as input the motion of lower and upper plate of the pneumatic spring, carries out the dynamics of harvester, the pressures and volumes in chambers, and the electric power recovered by means piezoelectric transducers.

It is worth noting that this system is nonlinear in state due to the consideration of the elongation traction contribute (equations 5.59 and 5.60). This term must be taken into account considering the boundary condition between the piezoelectric elements and the tuning mass. Another observation concerns the stiffness K_m and damping C_m. They vary, for big relative displacement, with nonlinear law. In the proposed model these coefficients are treated as constant because the aim of the model is to preliminary find their values for the device design. The nonlinearities that happen when big relative displacements occur must be further considered by a nonlinear model or in the prototype experimental testing activity.

With reference to the electrical part, we refer to a simplified and usual approach that consists in considering a resistor directly connected to the generator and the harvested power is defined as the power dissipated into the resistive load R_L.

In the practical application of the EH devices an electric load represented by a resistor RL cannot be directly connected to the transducer terminals. Various circuit topology able to perform AC/DC ca be easily implemented and linked to the proposed model for further analysis.

The presented model describes the behaviour of the different components of the device that has been implemented in the Matlab Simulink environment to build a simulator. Therefore, a numerical block-oriented model has been developed. Each part, mechanical, transducer and electrical, interacts with the others exchanging mutual inputs and outputs. The block-oriented model can be seen as composed of three main subsystems.

The first one is the input signal. It generates the acceleration or, alternatively, the velocity or the displacement profile that excites the lower plate of the air spring and, thus the energy harvester. It can be a sinusoidal input or the acceleration profile measured on a bogie or carried out from vehicle dynamic simulation (see chapter 2). The second part is the generator composed by mechanical part and the transduction mechanism. This part includes the mutual interaction between the FD and the thermodynamic state of the air spring. Finally there is the connection to the electrical load.

Chapter 6

Energy harvesting device prototyping and testing

This chapter concerns the activities of prototyping and experimental testing of the EH device. A piezoelectric EH based on a resonant FD and integrated in an air spring was designed, prototyped and experimentally tested. The aims are to develop an energy harvesting device targeted to environmental vibrations energy recovery and to tune the numerical model against experimental evidence.

These activities were conducted in two steps. A first mock-up was prototyped and tested on a shaker, considering just the base motion excitation mechanism, to develop the device and to tune the numerical model against experimental evidence. In the second step a full-scale prototype of an air spring with the EH system was built. In order to test the full-scale component, the design of a new test bench was carried out. Finally, the Air spring integrating the EH device was tested and models were validated.

6.1 Experimental activity on the shaker

6.1.1 EH device prototyping

Flexible diaphragm and rigid frame

The support assembly consists of a flexible diaphragm, made by natural rubber, connected to a cylindrical steel frame. Its dimensions are designed considering as reference air spring the one illustrated in the section 3.3.4. Therefore, the steel cylinder has an internal diameter of 160 mm, a thickness of 3 mm and a height of 100 mm. In order to fasten the support cylinder to the shaker, a circular steel plate is welded on one side to form a cup. This cup is thus bolted to the shaker. On the opposite side the FD is

fixed and stretched on the cylinder by means of a steel ring. Along the cylinder lateral surface there are two opening to guarantee the assembly operations and the location of the accelerometer and the tuning mass. The geometrical features of FD and rigid frame are summarised in figure (6.1).

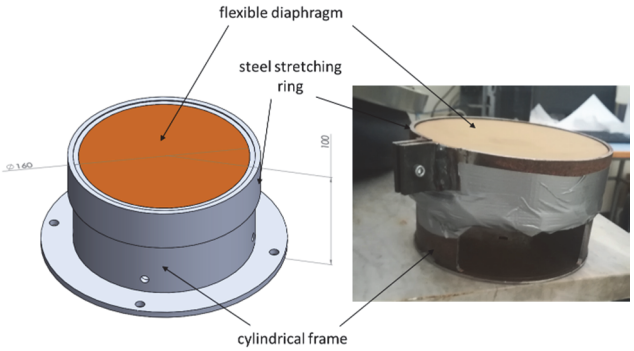

Figure 6.1 Flexible diaphragm and cylindrical frame.

The material used for FD is natural rubber operating in a temperature range of -40 °C to+85 °C. The technical specifications are already showed in the table 4.2 section 4.2.2.

A tuning mass is installed at the circle centre of the FD in order to set the device natural frequency at a required value so to have the desired resonance effect.

The piezoelectric patch

The piezoelectric element bonded on the FD support is a transducer supplied by PI Ceramic [111], whose commercial name is DuraAct. A DuraAct patch transducer consists of a thin piezo-ceramic film which is covered with an electrically conducting material to ensure the electrical contact and that is subsequently embedded in an elastic composite polymer. Given that the piezoceramic element is brittle in itself, it is mechanically preloaded and electrically insulated to make it is so robust that it can even be applied to curved surfaces with bending radii of only a few millimetres. The material of the piezo-ceramic film is called PIC255. It is a modified Lead Zirconate-Lead Titanate. From a qualitative point of view is characterized by a high Curie temperature, high permittivity, high coupling factor, high charge coefficient, low mechanical quality factor, low temperature coefficient. In table 6.1 are reported the main properties of piezoelectric material.

Table 6.1 Main parameters of piezoelectric patch.

Parameter	description	value	
ρ	Density	7.80E+03	kg/m³
d_{31}	Piezoelectric charge coefficient	-1,74E-10	m/V
s_{11}^{E}	elastic compliance	1,590E-11	m²/N
$\varepsilon_{33}^{\sigma}$	Relative dielectric permittivity	1750	-
k_{31}	Coupling factor for transverse oscillation	0.351	-

From a dimensional point of view, the active piezoelectric area of the patches is smaller than the overall area occupied by the transducer. The considered layer dimensions are 81.5×13 mm while the active area is 70×10 mm. It follows that, when the patch is bonded, the active area remains shifted with respect to the fixed-end.

The EH device

According to the description of the harvesting system in paragraph 3.3 it is possible to arrange n rectangular piezoelectric films in a radial pattern on the upper surface of the FD as depicted in figure 6.2.

Figure 6.2 Possible arrangements of the piezoelectric rectangular patches on the FD.

In the following we refer to a prototype composed by four piezoelectric patches. Each transducer is glued to the corresponding substrate and has one end anchored to the rigid frame and the opposite one to the tuning mass. Figure 6.3 illustrates the EH system prototype used for the experimental tests.

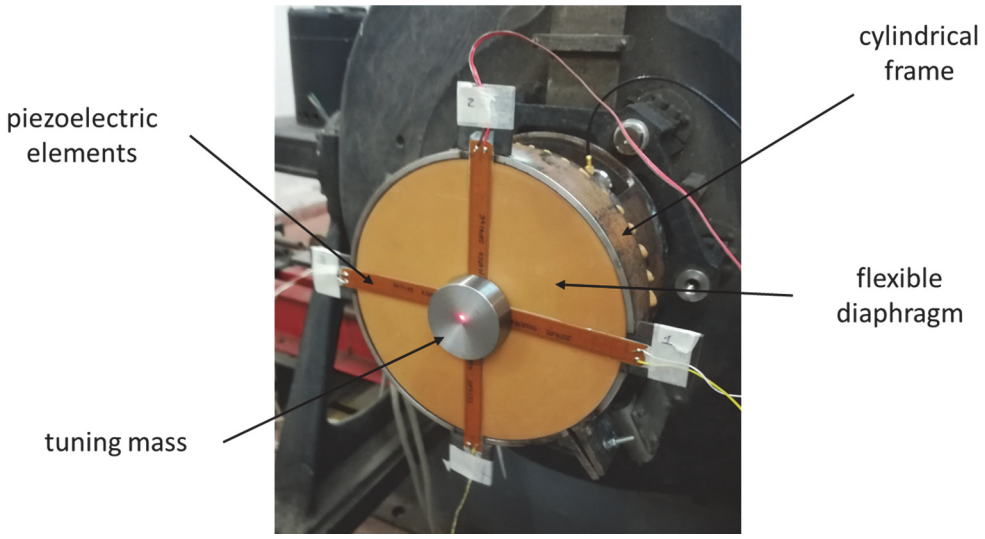

Figure 6.3 Energy harvesting device prototype.

6.1.2 Experimental setup and preliminary tests

Experimental setup

The experimental setup used for the device tests is based on the LabView system and it is shown in figure 6.4. A MB model C-5 shaker controlled in velocity reproduces the desired excitation profile of the mechanical input imposed on the fixed-end of the harvester. An uni-axial accelerometer placed on the steel cylinder base allows the measurement of the input. An interferometric laser sensor head OFV-505 Polytec Vibrometers measures the displacement, velocity and acceleration of the tuning mass, while LabView directly acquires the voltage signals.

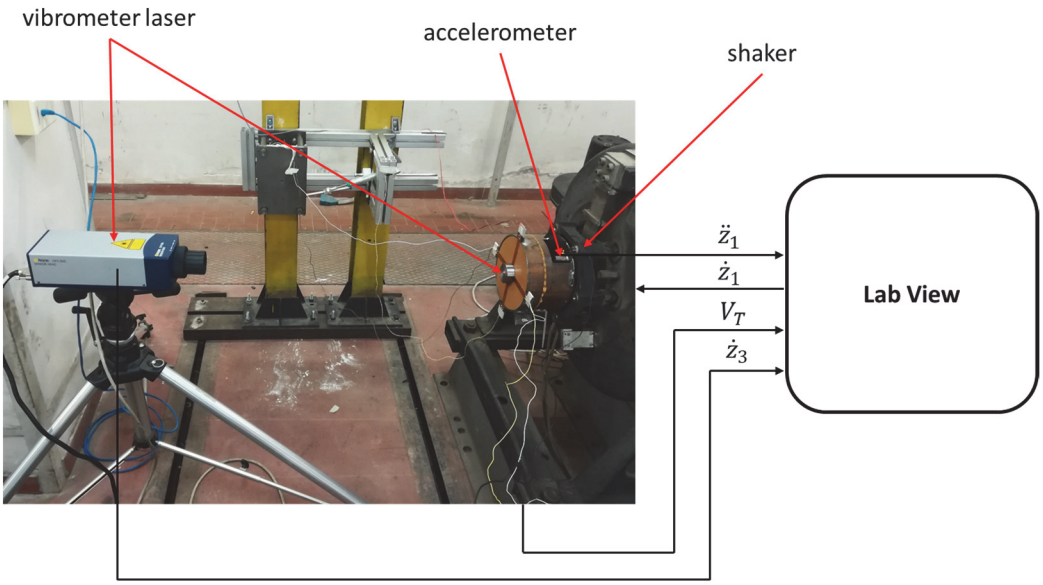

Figure 6.4 Experimental setup

Preliminary tests

A preliminary series of tests were conducted to ascertain the experimental setup. The mechanical properties of natural rubber FD and of the piezoelectric elements imply that the global stiffness of the assembly is strongly influenced by the transducer number. Therefore, two different configurations are considered for preliminary tests: the FD with a tuning mass of 61 g (without piezoelectric elements), and the FD with the four piezoelectric patches and a 120 g tuning mass. A constant base velocity amplitude sweeps in frequency are performed for both systems in order to qualitatively identify the vibration modes and frequency in the range of 0-50hz. Equations (6.1) is the function used to give the sweeps in frequency keeping constant the velocity amplitude *a.* Parameters are set to impose a sweep of frequency from 0 to 50 Hz and return in 120 seconds.

$$Sweep\ f = a * \sin(\omega t^2 \cdot 0.5\left(1 + \frac{60-t}{abs(60-t)}\right) + \omega(t-120)^2 \cdot 0.5(1 + \frac{t-60}{abs(t-60)})) \qquad (6.1)$$

After that, a deeper quantitative analysis is carried out applying a sinusoidal input at a different frequency around the resonance. The response velocity is measured in all tests in correspondence of the FD centre, that means in correspondence of the tuning mass.

Figure 6.5 show the result of the sweep-frequency test for the FD only and for a velocity input amplitude *a*=0.054 m/s.

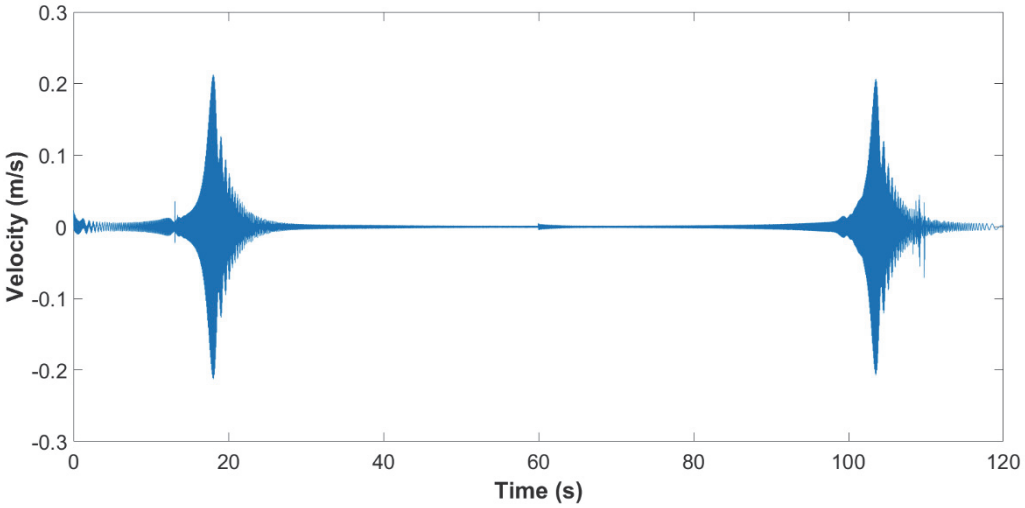

Figure 6.5 Preliminary test, sweep response for FD.

It is worth noting that, in the investigated range, only one natural frequency was found confirming the finite element study outlined in paragraph 4.1. This means that the proposed architecture has a relatively poor modal density, presenting a clear separation between the first natural frequency and the others.

Figure 6.6 depicts the frequency response of the FD with the four piezoelectric patches and a 120 g tuning mass, in terms of output (FD velocity)/input (base velocity) ratio.

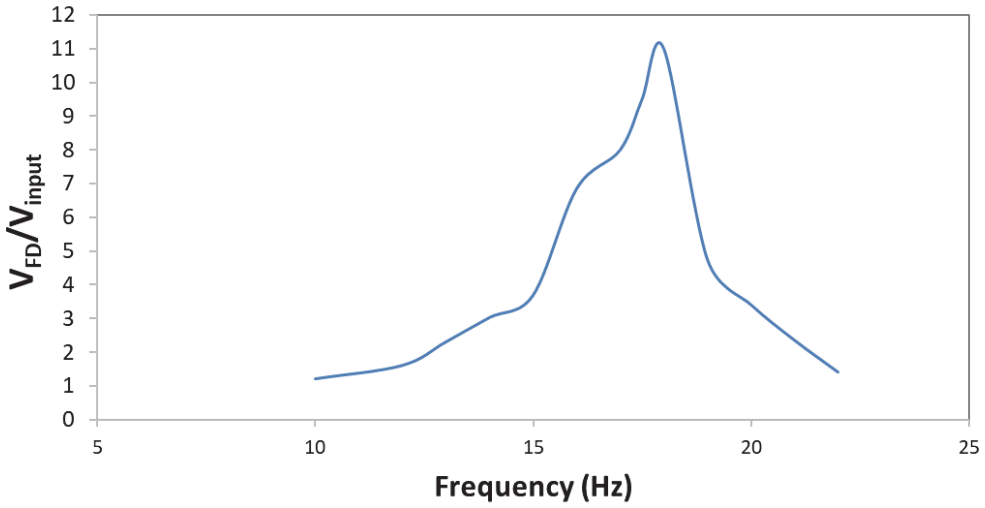

Figure 6.6 Preliminary test, frequency response.

The curve presents the main peak at about 18 Hz. Therefore, according to the equation (5.66), we calculate the overall stiffness of the system as:

$$K_m = nK_{p\_eq} + K_{FD} = (2\pi f)^2 * M = 1535 \ N/m \tag{6.2}$$

Where M is the tuning mass.

It should be remarked that generally, considering open and short-circuit conditions of the generator terminals, two different resonance frequencies exist. In open circuit current of the transducer i_t is null, and no energy is transferred to the electric domain. The stiffness of the system depends only on the mechanical proprieties:

$$K_{open\_c} = K_m \tag{6.3}$$

$$\omega_{open\_c} = \sqrt{\frac{K_{open\_c}}{M}} \tag{6.4}$$

Vice versa in short circuit it is possible to define a short-circuit stiffness that takes into account the electrical stiffness:

$$K_{short\_c} = K_{open\_c} + K_{el} \tag{6.5}$$

$$\omega_{short\_c} = \sqrt{\frac{K_{short\_c}}{M}} = \omega_{open\_c}\sqrt{1 + \frac{K_{el}}{K_{open\_c}}} \tag{6.6}$$

The preliminary experiments point out that K_{el} is negligible and that open and short-circuit natural frequency are practically the same. In other words, the diagram in figure 6.6 carried out for open and short circuit condition is the same. Thus, in the following we consider:

$$\omega_n = \omega_{open\_c} \cong \omega_{short\_c} = \sqrt{\frac{K_m}{M}} \tag{6.7}$$

For the EH scope we consider a prominent excitation frequency equal to 10 Hz (see chapter 2). Therefore, the device must be designed to have the natural frequency equal to this value. In order to set the device natural frequency at about 10 Hz a new tuning mass of 0.39 Kg was calculated inverting the relation (6.7). In this condition the static displacement of the membrane centre is about 2.5 mm.

The prototype with these features is reported in figure 6.3.

6.1.3 EH device testing and results

The prototype composed by the FD with the four piezoelectric patch and a 400 g tuning mass was investigated using the same testing procedure of the preliminary test. A constant base velocity amplitude sweeps in frequency is performed in order to identify qualitatively the vibration modes and frequency in the range of 0-50 Hz. The Sweep test confirms that the resonance frequency is 10 Hz and that there are no other natural frequencies. Then, several tests are conducted applying sinusoidal input at different frequencies around the resonance. Response velocity is measured in all tests in correspondence of FD centre, which is the tuning mass. Furthermore, the voltage generated by each piezoelectric element is measured connecting the piezoelectric terminal by means of a known resistor to evaluate the power generation. The measurements are conducted for two different electric impedances: 1 Mohm and 150 kohm.

In figure 6.7, 6.8 and 6.9 are reported the input sinusoidal velocity for 10 Hz test, the correspondent untreated signal of the FD centre velocity and their comparison in steady-state condition respectively.

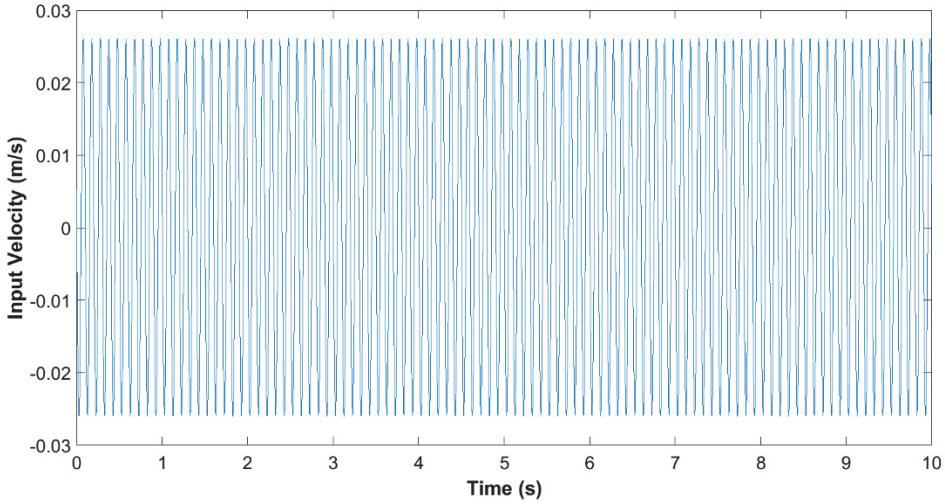

Figure 6.7 Input velocity signal for a 10 Hz base excitation.

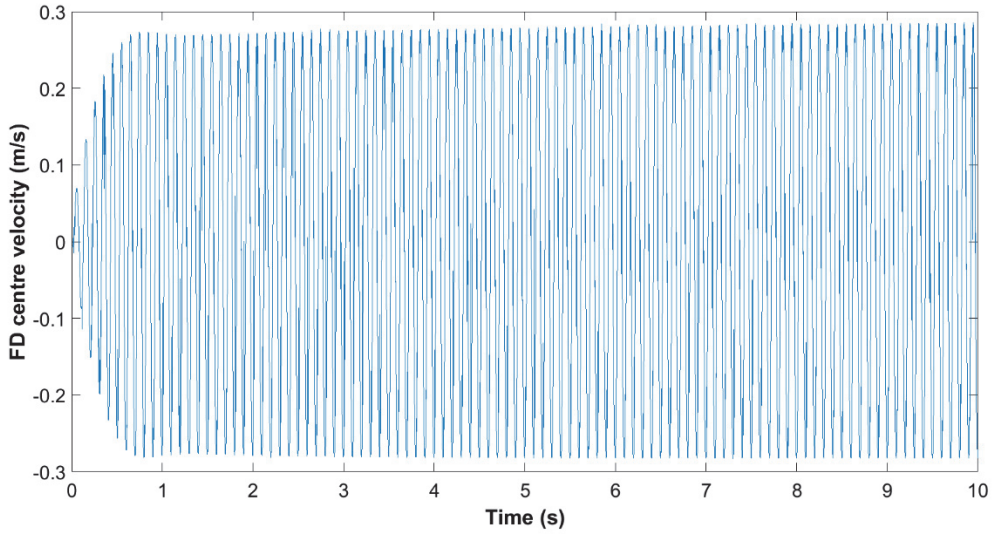

Figure 6.8 FD centre velocity for a 10 Hz sinusoidal base excitation.

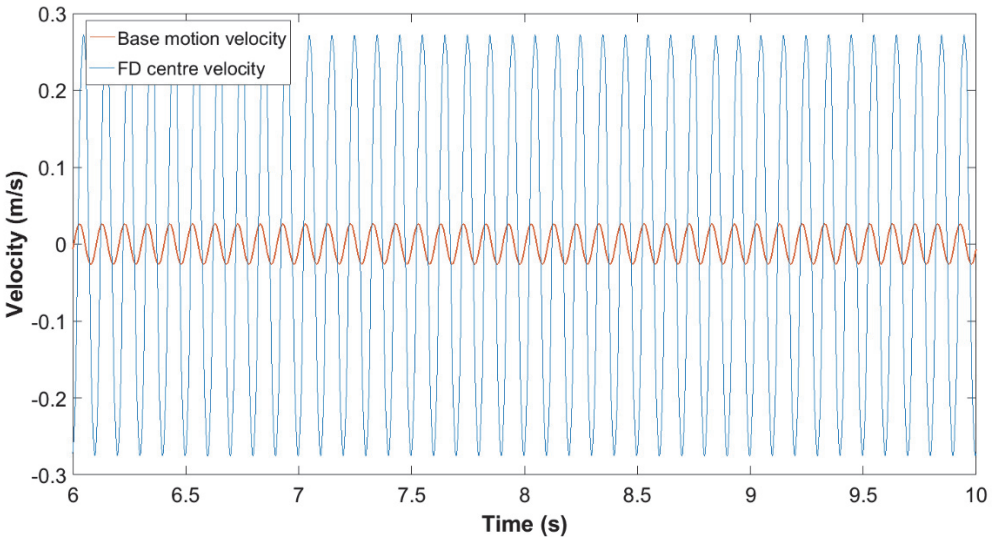

Figure 6.9 Comparison between input velocity and FD centre velocity for a 10 Hz base excitation.

From the velocity analysis, it is possible to note that after the transient the velocity amplitude of the tuning mass is about 11 times bigger then input velocity.

The frequency response in term of velocity ratio between the mass and the input is reported in figure 6.10. Which depicts that the resonance occurs at around 10 Hz.

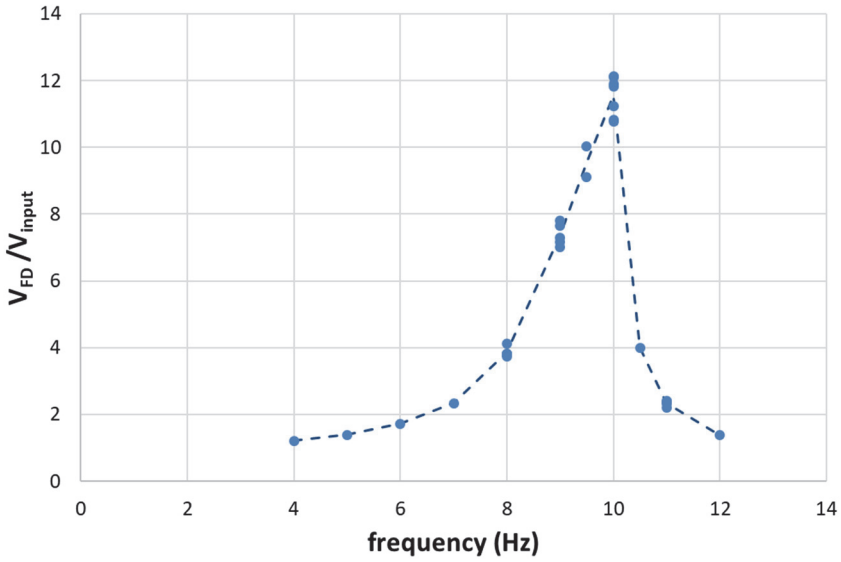

Figure 6.10 Prototype testing: frequency response in terms of velocity ratio.

The signal of the voltage generated by one piezoelectric element is reported in figure 6.11 an impedance R= 1Mohm.

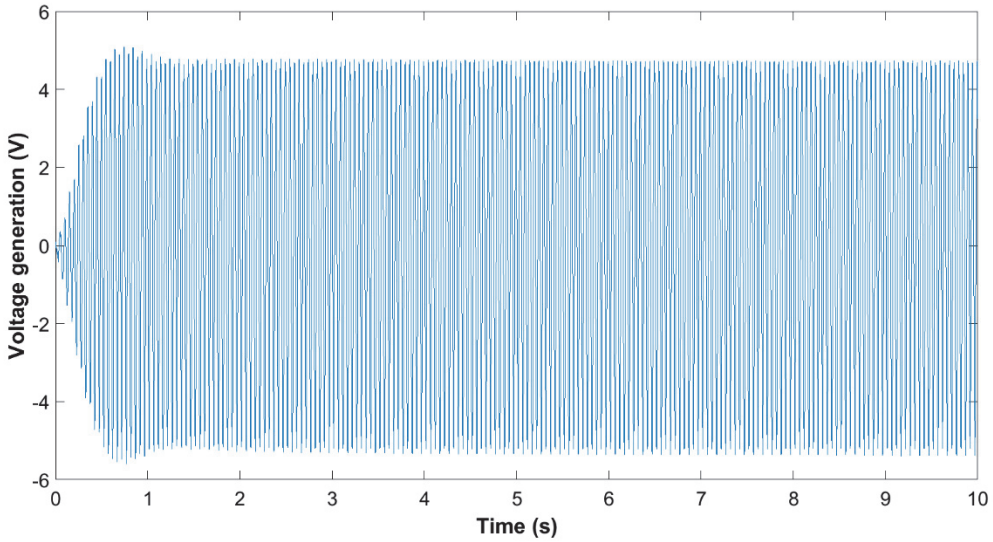

Figure 6.11 Voltage generated by one piezoelectric element for a 10 Hz sinusoidal base excitation.

It should be remarked that after the transient, about 1.3 seconds, a voltage is generated with frequency double that of the excitation. The active power generated by one piezoelectric element is calculated as:

$$P_a = \frac{V_{rms}^2}{R} \tag{6.8}$$

Where V_{rms} is the root mean square value of the voltage generation and R is the electric impedance. The frequency-domain response of the system in terms of active power generated by each transducer is reported in figure 6.12.

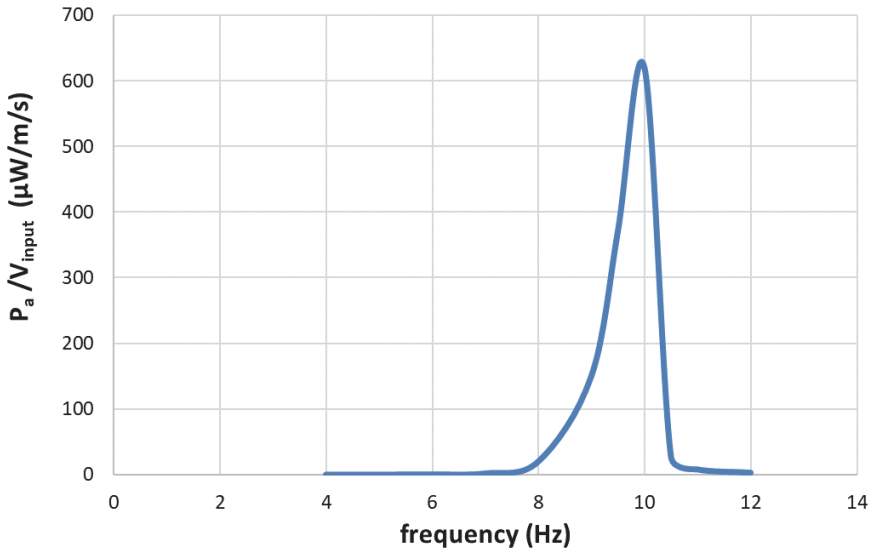

Figure 6.12 Prototype testing: frequency response in terms of power generation.

In order to evaluate if and how the gravity affects the results because of the shaker is placed to excite in horizontal direction rather than in vertical, tests results of each transducer are carried out placing them in every location 1,2,3,4 reported in figure 6.13.

No significative variations of voltage output level are related to the transducer position. In other words, for the same input, each piezoelectric element gives the same output independently of its location on FD.

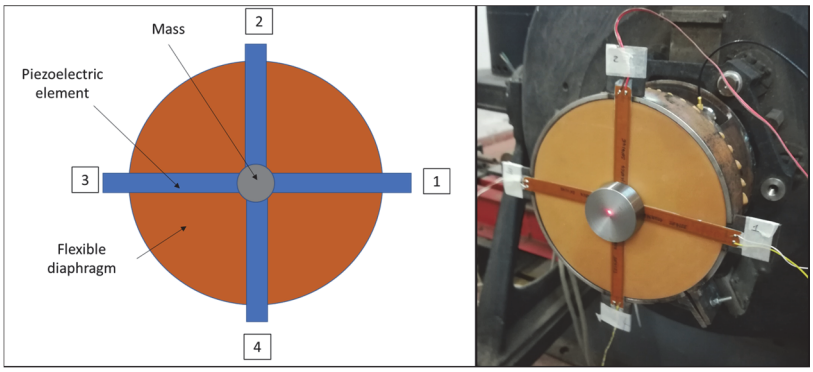

Figure 6.13 piezoelectric elements location during the shaker tests.

Model identification and results

In the following, experimental model identification, performed to identify the parameters of equations 5.65 (C_m, α, β, γ), is described. Due to the piezoelectric element employed and the geometry complexity, model parameters cannot be simply derived from geometrical and material properties. However, the structure still presents the features of the piezoelectric electromechanical device described in chapter 5.

The identification procedure was conducted by means the Simulink estimation parameter tool. The estimation was carried out giving as model input the acceleration measured by the accelerometer at the base cylindrical support and as output the voltage generated. The parameters C_m, α, β, γ were estimated for one test far from the resonance 6 Hz and for another in resonance at 10 Hz.

After the identification procedure, the simulation results are compared with experimental results of other tests.

It is worth noting that for this analysis, in the model equations 5.65 the term $(P_{bc} - P_{ac})\frac{\pi a^2}{4}$ is null since there are no closed volumes and the pressure on the both side of FD is considered the same.

The stiffness K_m of the assembly FD+transducers is calculated by equation 6.2, the piezoelectric main parameters are the ones reported in table 6.1, while the values of the other parameters of the model are reported in the table 6.2.

Table 6.2 Model parameters.

Parameter	description	value	
Piezoelectric elements geometry			
l_p	Piezoelectric length	0.07	m
b_p	Piezoelectric width	0.01	m
h_p	Piezoelectric thickness	0.0003	m
Flexible diaphragm			
a	Diaphragm radius	82	mm
M	Tuning mass	0.4	Kg
Electrical parameter			
R	Electrical load	1e+6	ohm

The results carried out from the identification procedure are summarized in table 6.3.

Table 6.3 Model identification parameter results.

Test	C_m (Ns/m)	α	β	γ
No resonance	0.8	5e-6	5e-6	0.008
resonance	2.3	5e-6	5e-6	0.002

It should be noted that the values of C_m and γ differ based on the resonance. This can be explained by considering the model proposed with constant coefficients. In the experimental case, when a resonance occurs, we are in the field of non-small displacement where nonlinearities are not negligible. Therefore, in real case C_m, α, β, γ and also K_m vary with the deformation. Nevertheless, as depicted in figure 6.12, the majority of the energy recovery happens when the excitation frequency coincides with the device natural one and, thus, the predictions made considering the proposed model with estimated parameter in resonance condition can give suitable results. In figure 6.14 the generated voltage obtained in simulation and by experimental test for 10 Hz sinusoidal excitation are compared. It is possible to note that the simulation results are in good agreement with the experimental test.

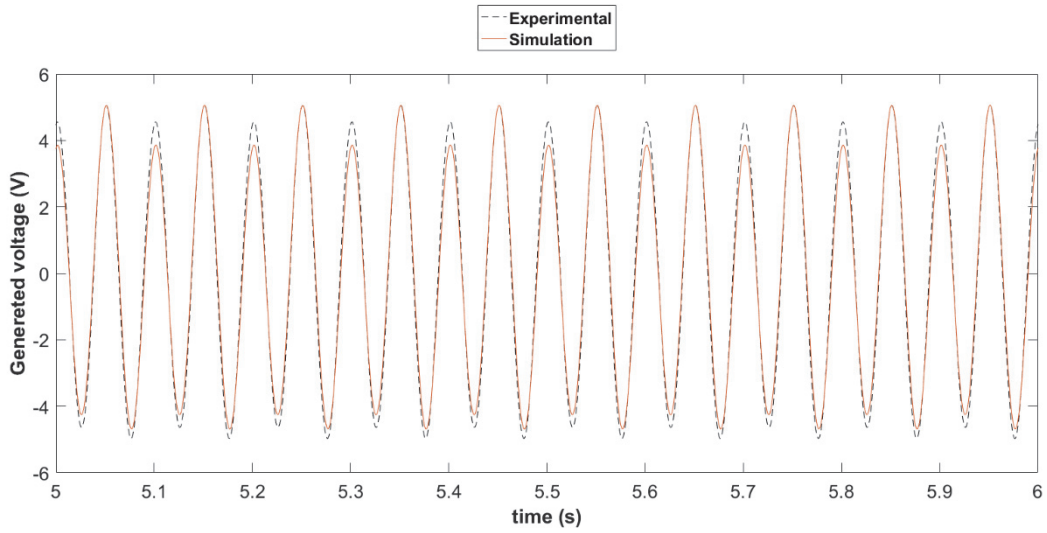

Figure 6.14 Generated voltage: experimental vs. simulation results.

In terms of active power generated, the model also returns good results. Using the equation (6.8), the simulated active power is 0.011mW, while the average results of all tests is 0.016 mW.

6.2 Full-scale testing activity

To perform the full-scale tests, two activities were carried out in parallel. On one hand the prototype built to modify a commercial air spring for a metro train; on the other, the design of a test-rig where tests were carried out. In the following the procedure to build the prototype is illustrated alongside an explanation of how the test rig was designed and built, finally the first results of the full-scale activity are showed.

6.2.1 EH system integrated in a pneumatic spring prototyping

The geometrical layout of the EH system to be embedded in the air spring is designed with the component analysis chosen as reference (see paragraph 3.3.4). In this phase of the study, we made the prototype by replacing the internal emergency bumper with the harvester as shown in figure 6.15. In a more complex solution, the bumper can integrate

the harvester, or the air spring lower plate can be designed to include both the harvester and the bumper. Another solution could be that of placing the emergency bumper externally to the pneumatic spring.

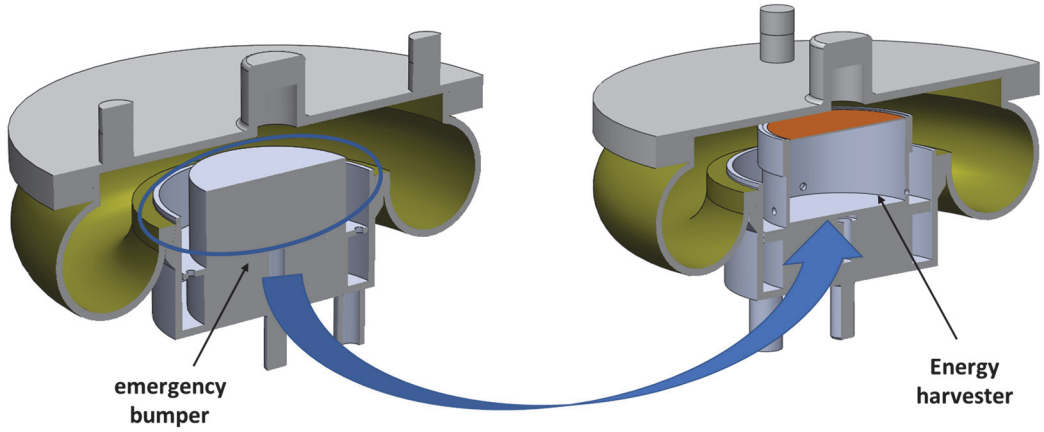

Figure 6.15 Project of full-scale prototype.

Figure 6.16 show the isometric view of the steel frame support cylinder for flexible diaphragm and its main dimensions.

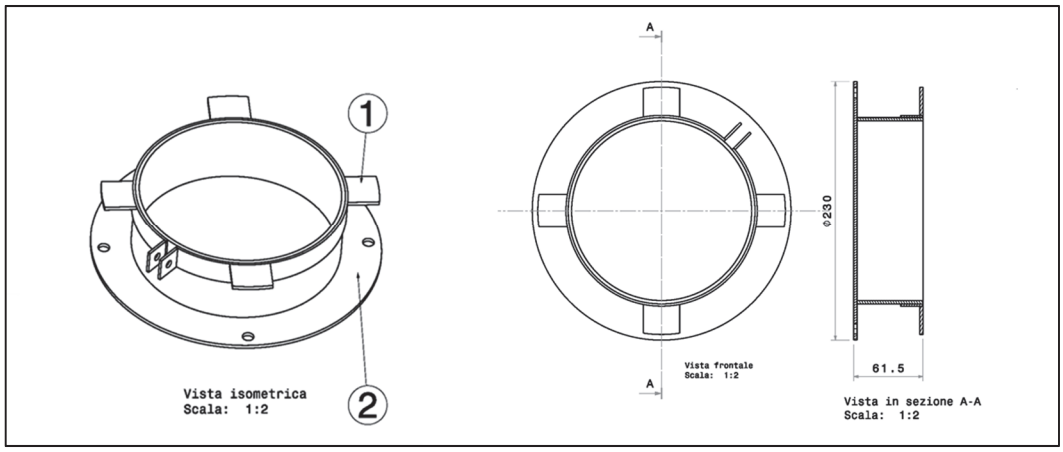

Figure 6.16 Cylindrical steel frame dimension.

Twelve threaded holes, 6mm in dimeter, were drilled on support lateral surface. These holes can be closed or open by bolts in order to test both the operational principle, base motion on its own (all holes are open) and the combination between base motion and

pressure-induced vibration (appropriate combination of open and closed holes). The FD is fixed and stretched on the cylinder by means of a steel ring (component 1 in figure 6.16). This ring has four cantilever supports, where each of them allows fixing one edge of the piezoelectric element, similarly to the first prototype. The remaining part of each piezoelectric patch is glued to the FD.

The procedure adopted to modify the pneumatic spring is summarised in figure 6.17. The air spring is open by removing the upper plate, then the emergency bumper is taken away and finally the harvester is fixed to the lower plate exploiting the same bolts connection of the bumper. In order to acquire the voltage generation, the wires connected to the piezoelectric terminal are brought out by a small hole on the upper plate. To avoid air leakage this hole is corked using an appropriate polymer.

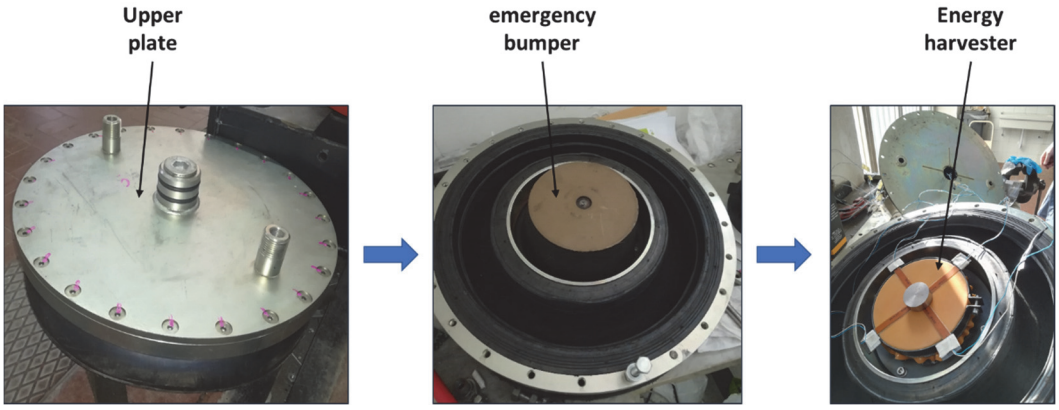

Figure 6.17 EH integrated in the air spring prototype.

6.2.2 Test rig design

In order to perform the experimental tests on the full-scale prototype, a new test rig was designed and built. More precisely, we built the structural modification of a seismic test rig available at the Department of Industrial Engineering. In the following the existing seismic test rig is briefly described and then the design and of its modification is shown.

The seismic test rig

The seismic test rig is a versatile system employed to characterise seismic isolators or structures [112], [113]. It (fig. 6.18 and 6.19) consists of movable and fixed parts made in structural steel. Particularly, it is constituted by:

- fixed base;
- hydraulically actuated sliding table with dimensions 1.8 m x 1.6 m;
- Hydraulic actuator.

The table motion is constrained to a single horizontal axis by means of recirculating ball-bearing linear guides.

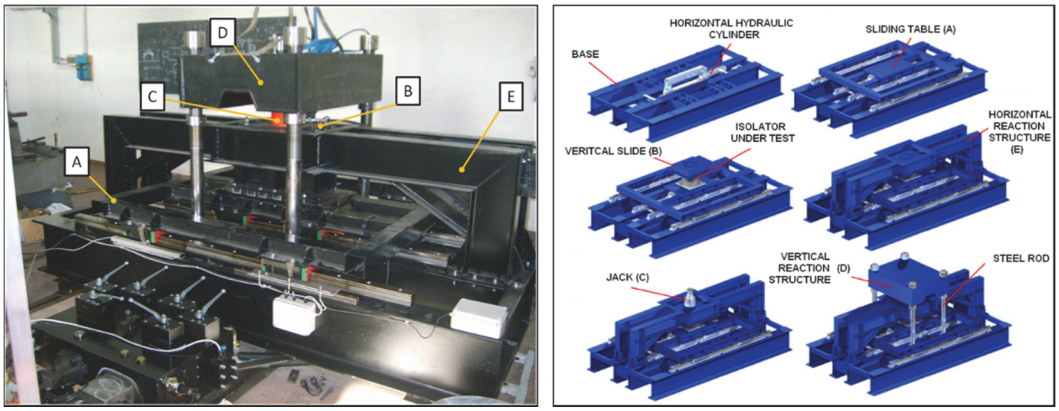

Figure 6.18 Existing seismic test rig [113].

The isolator under test is placed between the sliding table (A) and the vertical slide (B). The hydraulic jack (C) allows the isolator under test to be vertically loaded (max 850 kN). The vertical load is maintained constant by means of a hydraulic accumulator. The vertical (D) and horizontal (E) reaction structures respectively balance the jack load and the force acting on the table.

The hydraulic power unit consists of a variable displacement pump powered by a 75 kW AC electric motor and able to generate a maximum pressure of 210 bar and a maximum flow rate equal to 313 l/min. A pressure relief valve is located downstream of the pump.

The hydraulic circuit consists of a four way-three position proportional valve and a hydraulic cylinder. The cylinder is constituted by two equal parts separated by a diaphragm and contains two pistons which rods are connected to the base; so, the actuator is characterized by a mobile barrel and fixed pistons. The maximum horizontal force is 190kN, the maximum speed 2.2m/s and the maximum stroke 0.4 m (± 0.2 m).

The test rig re-design

In order to exploit the existing hydraulic actuation system for the experimental activities on the modified air spring, a test rig re-design was necessary. All the component above

to the sliding table are disassembled (figure 6.19) to create a new interface between fixed and moving part adapted to railway air springs interface. Moreover, a new sliding table was designed to reduce its weight and to avoid excessive inertial load during the dynamic tests.

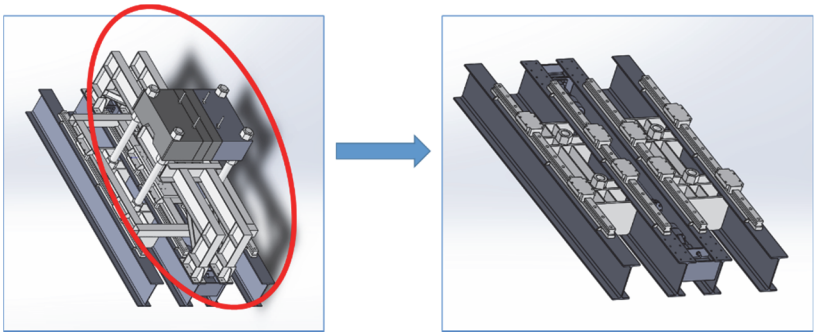

Figure 6.19 Seismic test rig removed parts.

Four steel structures were designed (figure 6.20):

- A reduced sliding table
- A moving reaction structure, integral with the sliding table and where the lower plate must be connected
- A fixed reaction structure
- An interface between the air spring upper plate and the reaction structure.

Figure 6.21 shows the lateral view of the new test rig with the main dimensions. A load cell is inserted in series with the interface component and the reaction structure by means a knuckle joint to measure the force component direct along the horizontal axis only. It is worth noting that in this configuration the air spring is rotate of 90 degree respect to its normal working condition and, thus, the horizontal test rig direction represent the air spring vertical direction.

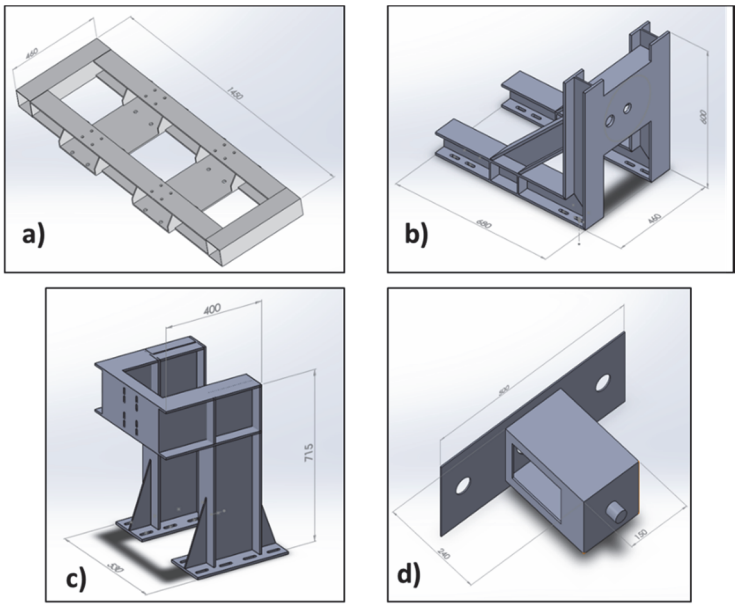

Figure 6.20 Test rig designed component: a) sliding table, b) moving support, c) reaction structure, d) interface.

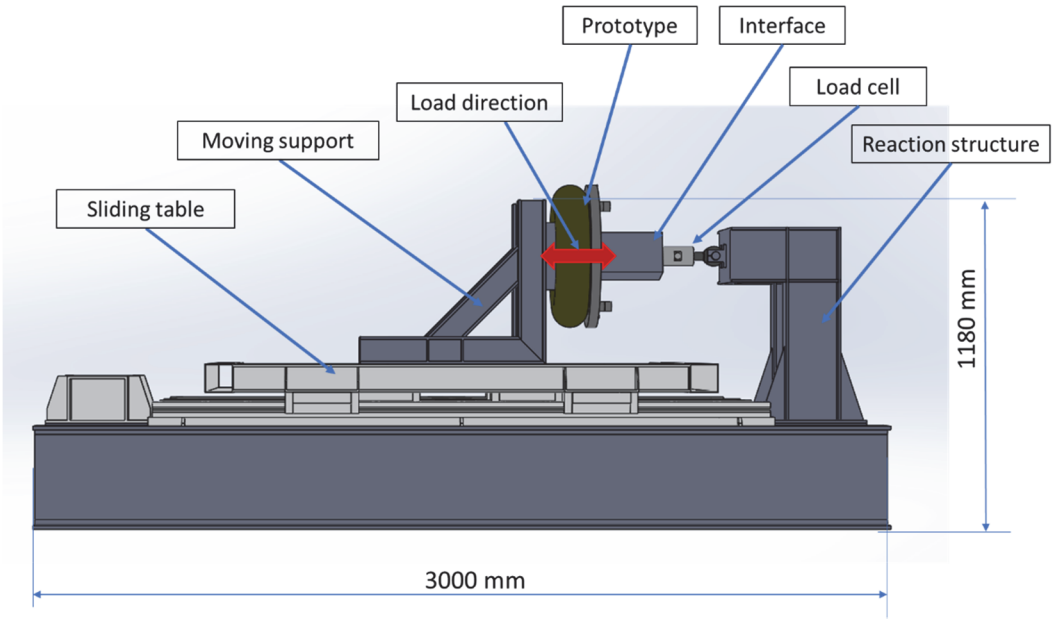

Figure 6.21 Re-designed test rig assembly.

All components are designed to guarantee in correspondence of a horizontal load of 85 kN, applied along the spring axis, both the structural integrity and a maximum deformation in the load direction of less than 2 mm. The design load was determined building on the maximum expected operational load plus a security overload. The final configurations were achieved after an iterative process of structural verification by mean of finite element studies.

For explanatory purpose, in figure 6.21 and 6.22 are reported the load conditions and the results in terms of displacements for the moving support and for the reaction structure respectively.

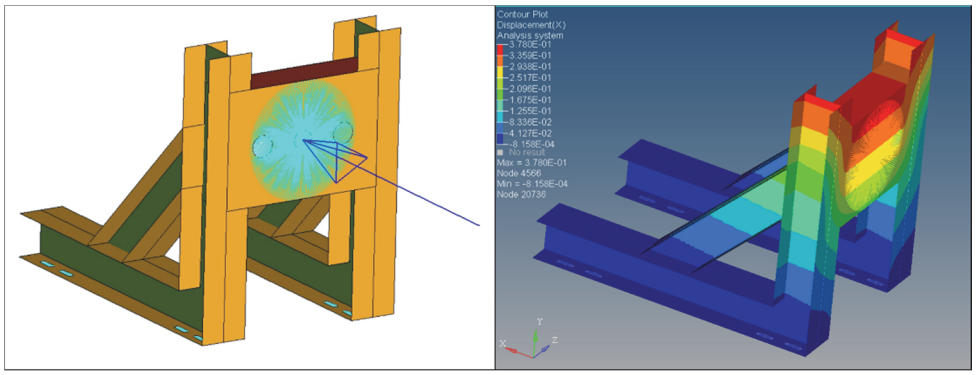

Figure 6.22 Moving support finite element analysis.

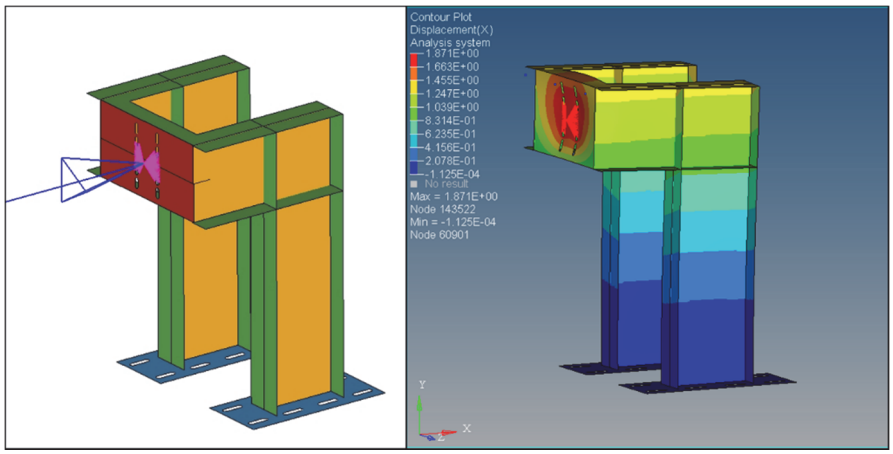

Figure 6.23 Reaction fixed structure finite element analysis.

Table 6.4 Finite element main results for the reaction structures.

component	Max displacement along load direction (mm)	Max Von Mises stress (MPa)
Moving support	0.49	208
Fixed reaction structure	1.3	309

Table 6.4 summarizes the finite element main results for the reaction structures.

Therefore, the final test rig configuration was realized as showed in figure 6.24. It is able to perform one-directional dynamic tests on different air springs size, for loads up to 85 kN. A pressure sensor, an LVDT transducer and a compressor to inflate the bellow, completes the test bench layout.

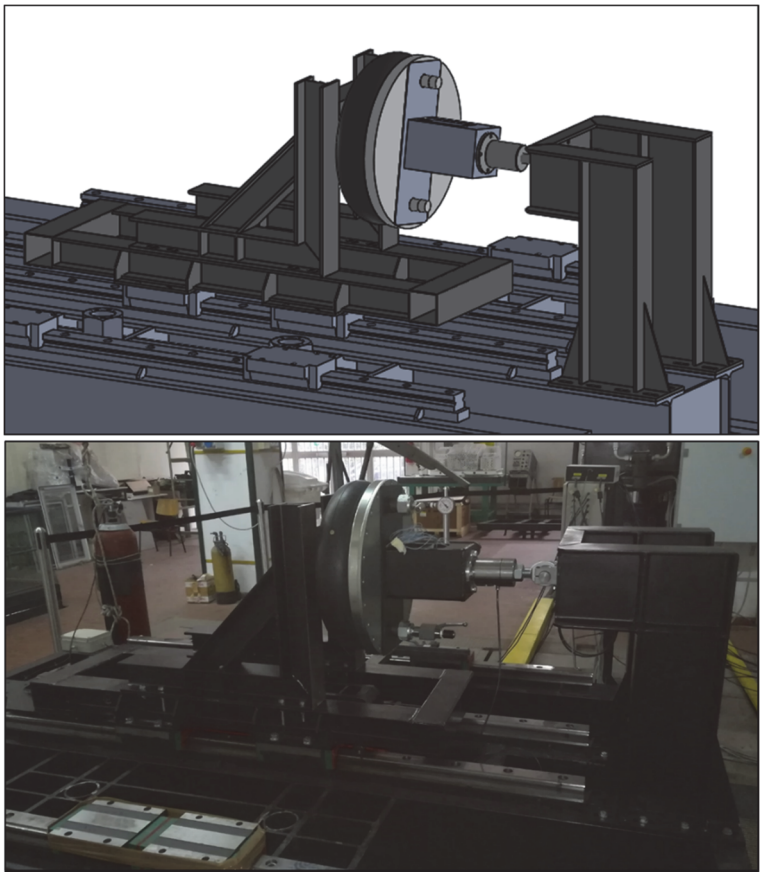

Figure 6.24 Air spring test rig: design and construction.

6.2.3 Experimental setup and testing procedure

Experimental setup

The experimental setup used for the air spring test rig management is based on a real-time system. The test rig is displacement controlled. It needs a suitable controller able to guarantee the desired table displacement in presence of unknown reaction force of the device under test. The hardware part of the measurement and management system consists of the DS1103 processing board. The DS1103 control board is a fast prototyping board produced by the German company dSPACE, designed and used mainly for the development of high-speed multi-variable digital controllers and real-time simulations in various fields. The system is equipped with an appropriate software package that allows generating the real-time code directly from a Matlab/Simulink model.

This system can perform the real time control and management of the hydraulic system (and thus of the sliding table displacement) and, at the same time, it allows to acquire the desired output. For the full-scale tests, the following quantities are measured:

- The pressure inside the bellow
- The displacement of lower plate
- The reaction force of the air spring
- The voltage carried out by the four generators of EH system for a resistive load of 10 Mohm

Several tests are conducted applying a sinusoidal input at different frequencies, from 1 Hz until to over the EH device resonance. The first series of tests are performed for the following device layout: the hole on the FD cylindrical support are all open, thus it is possible to assume that the pressure in the spring chamber and the auxiliary chamber is the same at all times (see pharagraph 3.3). In such case, the FD moves only due to inertial load and therefore the energy of the only base motion excitation flows to the harvester. It is worth noting that this layout is very similar to the one tested on the shaker and detailed in the paragraph 6.1, except for some device geometric dimensions.

Testing procedure

In figure 6.25 is reported an example of the typical displacement input for the tests. Each test is performed in seven steps and they are:

1) *Inflation* – the pneumatic spring is held in test bench zero position to inflate the air in the spring until it reaches the desired pressure. The step duration depends on the desired pressure level.

2) *Approach to working condition* – Ramp approach to the air spring nominal working condition.
3) *Period of adjustment* – It is a retain phase to allow the end of transitory phenomena
4) *Loading* – the system is loaded at the desired frequency
5) *Period of adjustment* – It is a second retain phase to allow the end of transitory phenomena after the load.
6) *Return to zero* – Ramp approach to the test bench zero position.
7) *Deflation* – the pneumatic spring is deflating to avoid load on the test rig when it is not controlled.

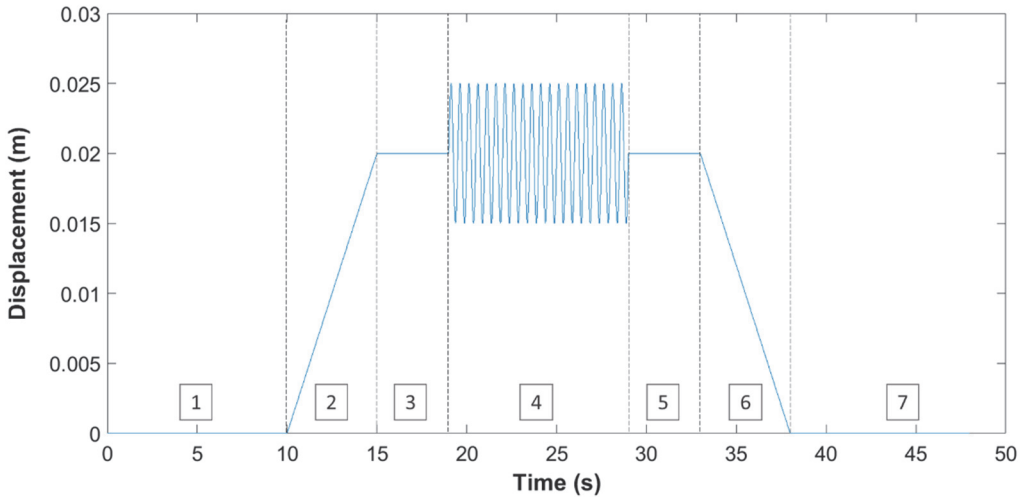

Figure 6.25 Testing procedure for the full-scale tests.

6.2.4 Results and discussion

The measured reaction force of the air spring for a 9 Hz displacement sinusoidal input of 5 mm in amplitude is reported. In particular, figure 6.27 shows the force measured during all the testing procedure and a zoom on the loading part. In accordance to what is expected the reaction force increase during the inflation step. Then, when the air spring height is set to the nominal working condition it decrease. This is because at test rig zero condition corresponds a bellow height smaller than the nominal one. Therefore, during

the second step the air spring height increases as well as its volume and, thus, air pressure decreases and in turn so does the reaction force. In the third and five steps (retain), the reaction force is constant, while during the loading step it varies with a sinusoidal law. In the step six, force increases as the suspension height decreases and finally, during deflation, the force decreases until equilibrium is reached.

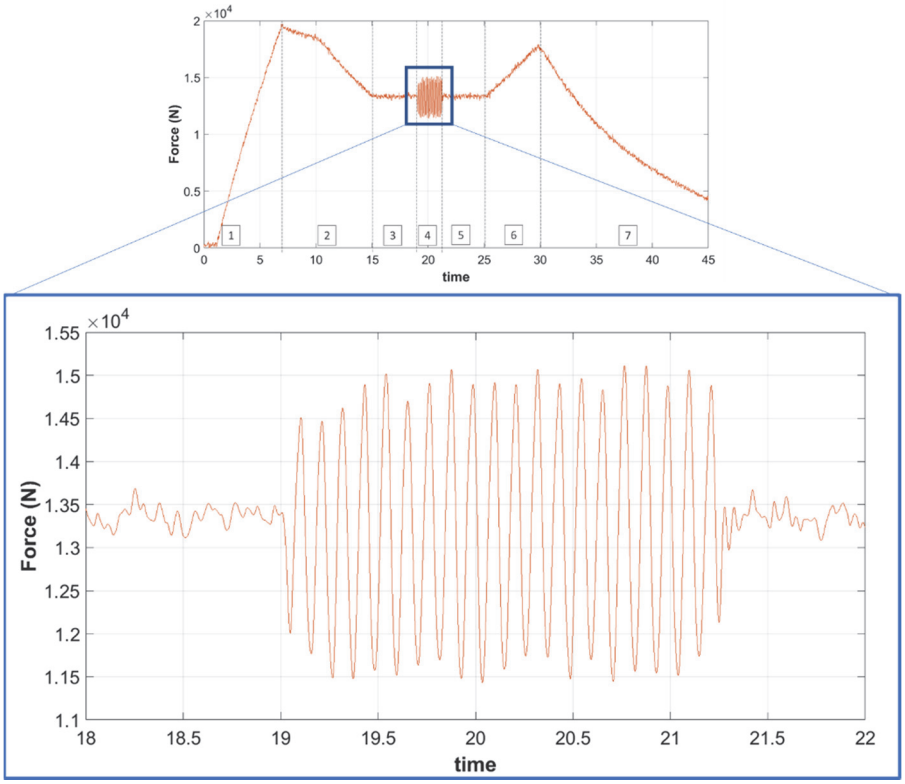

Figure 6.26 Measured reaction force for a 9 Hz sinusoidal excitation.

For the same test the relative pressure inside the bellow, and the voltage carried out by one transducer are reported in figure 6.27 and 6.28 respectively. Here, it should be noted that both the reaction force and pressure inside the spring vary with a sinusoidal law in accordance to the applied load.

It should be noted that, in accordance to finite element study and the experimental activity on the shaker, the voltage is generated with frequency double that of the excitation.

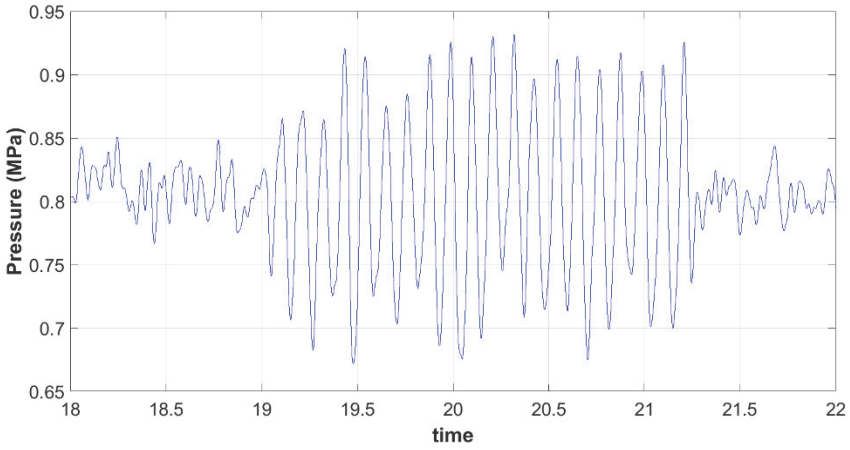

Figure 6.27 Measured reaction force for a 9 Hz sinusoidal excitation.

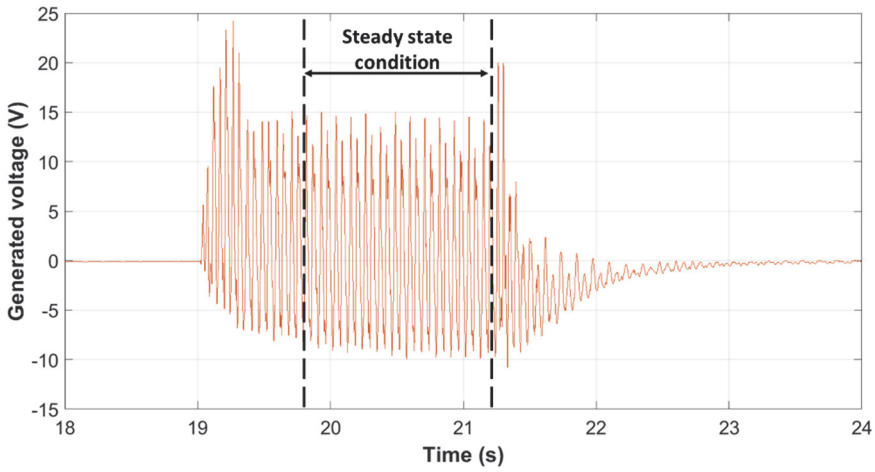

Figure 6.28 Generated voltage for a 9 Hz sinusoidal excitation.

The active power generated by each piezoelectric element is calculated considering the steady state vibration conditions using equation 6.8.

Performing tests at different excitation frequencies, the frequency-domain response of the system is carried out. Figure 6.29 shows the trend of the ratio between the average active power of the four transducers and input displacement in function of the frequency excitation. The value of active power considered is the average between the four transducers.

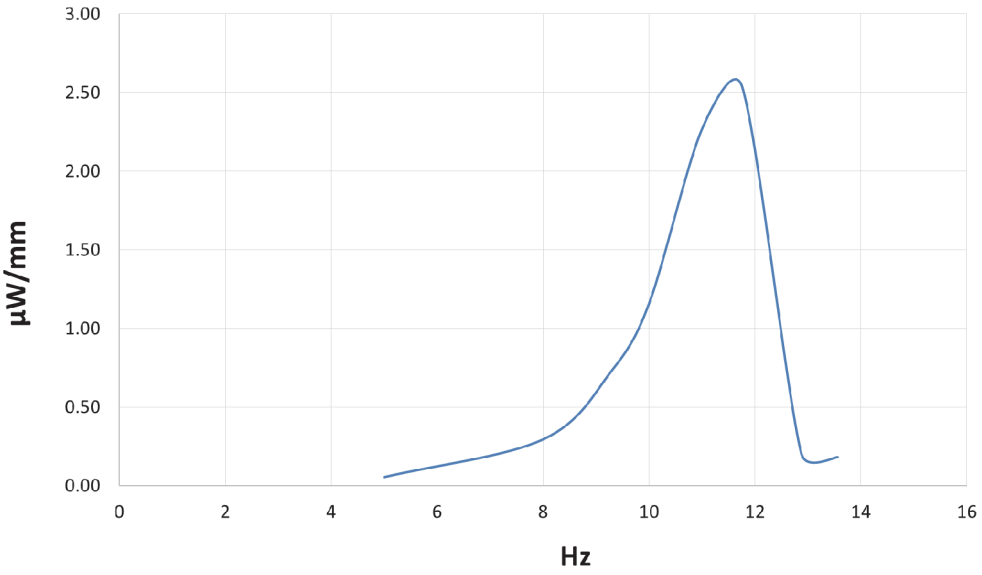

Figure 6.29 Full-scale testing frequency response in terms of power generation.

Results show the resonance and thus the max power generated occurs between 11 and 12 Hz. At this frequency, every piezoelectric element generates 2.6 µW for every millimetre of air spring lower plate displacement. The generated output voltage in correspondence of resonant condition is reported for one piezoelectric element in figure 6.30.

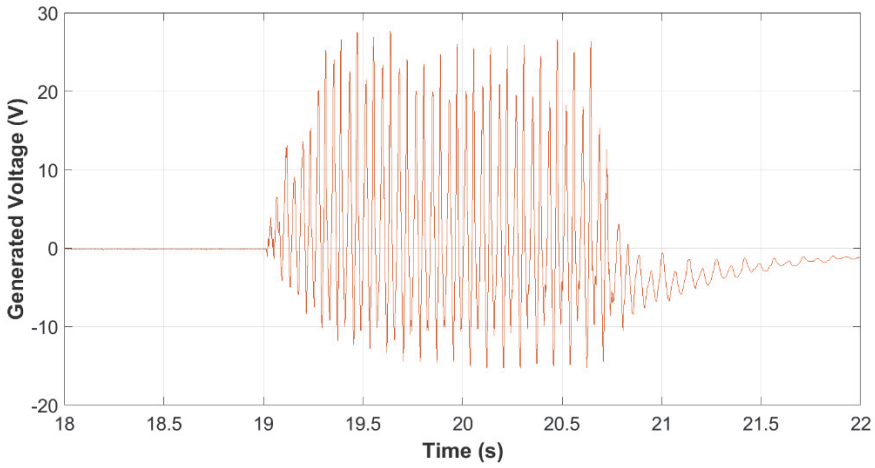

Figure 6.30 Generated voltage for a 12 Hz sinusoidal excitation.

Conclusions and future developments

The research effort in energy harvesting from both academic and private sector has increased exponentially due to an increase of possible applications. The development of autonomous wireless electronics, employed to gather information on a specific environment and powered by the surrounding environment energy, is driving the interest to power small-scale autonomous electronic devices.

This PhD thesis is targeted to investigate an energy harvesting system to be integrated in a railway pneumatic spring to recovery otherwise wasted energy source from suspension vibration. The final vision is to create an autonomous and smart air spring capable of collecting information for the monitoring and diagnostics of the vehicle or its subsystems. The piezoelectric technology is investigated to convert the mechanical energy into an electrical one for the energy harvesting system to design and develop functional prototypes. The research project focuses on the energy conversion chain starting from energy source analysis, passing to the mechanical structure for the energy extraction, up to the transduction mechanism for the conversion and to the electric load.

In order to analyse the piezoelectric energy harvesting capability, an accurate study of the excitation mechanism has been conducted. Building on that study, a complete piezoelectric EH system embedded in an air spring has been designed, analysed and tested, realizing an ad-hoc test rig for the full-scale testing activities.

For the design phase, being the dynamic of the harvester strictly influenced by the air spring type and working condition, two models have been developed: a finite element model to preliminary study the dynamic behaviour of the assembly; a multi-physical model for piezoelectric energy harvesting suitable as design tool. The developed device performs mechanical energy extraction and conversion exploiting both the oscillation of a mass placed at centre of a FD with a piezoelectric patch bonded on the upper surface. Mass oscillation are generated by a double mechanism: excitation deriving from the bogie during train operations; excitation due to a pressure difference appropriately generated between the two chambers divided by the FD.

The prototyping and testing activities were conducted in two steps adopting commercial available piezoelectric transducers. A first mock-up was prototyped and tested on a shaker, to develop the device and to tune the numerical model against experimental evidence. Building on the resulting outcomes, the analytical models are applied to a full-scale prototype of an air spring with the EH system in the second step. To test the full-scale component, the design of a new test bench was carried out. Finally, a first series of

tests on the air spring integrating the EH device was performed, and models were validated.

Piezoelectric energy harvesting has demonstrated to be a suitable solution for energy recovery from low frequency vibration. Experimental analysis highlighted encouraging results showing that at resonance frequency every piezoelectric element generates 2.6 μW for every millimetre of air spring lower plate displacement. This amount of power can be considered satisfactory for the proposed application considering that an optimization of the whole system including the electronics will be performed and that the monitoring is achievable also by performing intermittent measurement during train operation.

Next step of the activity should be the implementation of the electric part of the system that allows the current rectification with an AC/DC converter, the regulation of the DC voltage to make it compliant to the storage element or the electric load requirements and the connection between the different piezoelectric patches. Furthermore, a deeper and wider experimental analysis is still necessary to investigate the effects of pressure difference on the power generation when the number and the size of the holes vary. This kind of study can be easily conducted having available a full-scale prototype and an ad-hoc test bench. About the modelling activity, future improvements should focus on the implementation in the multi-physical model of the nonlinearities of the stiffness and the damping as well as the electrical circuit.

A further step regarding the harvester could be the design of an ad-hoc piezoelectric patch that is optimized to make the most of the characteristics of the system and to maximise the energy conversion.

Finally, it might be interesting to evaluate the integration of the air spring, which embeds the EH system, in the rail vehicle and its effects on the train vertical dynamics when varying EH parameters, such as orifices and FD dimension.

References

[1] A. Genovese, M. Russo, and S. Strano, “Mechanical characterization and modeling of an innovative composite material for railway applications,” *Proc. Inst. Mech. Eng. Part L J. Mater. Des. Appl.*, vol. 231, no. 1–2, pp. 122–130, Feb. 2017.

[2] A. GENOVESE, M. GRASSO, and S. STRANO, “A composite sandwich shock absorber mounting for an innovative rail vehicle end: design, computational analysis and fabrication,” in *IAENG Transactions on Engineering Sciences*, 2016, pp. 404–417.

[3] A. Genovese, S. Strano, and M. Terzo, “Model-based study of a resonant system in a railway air spring secondary suspension for energy harvesting applications,” *ACM Int. Conf. Proceeding Ser.*, vol. 2018–Febru, pp. 45–51, 2018.

[4] A. Genovese, G. P. Pucillo, M. Russo, and S. Strano, “Numerical and experimental investigation of innovative composite sandwich shock absorber mountings for metro railway applications,” in *2016 International Conference on Electrical Systems for Aircraft, Railway, Ship Propulsion and Road Vehicles and International Transportation Electrification Conference, ESARS-ITEC 2016*, 2017.

[5] A. Genovese and S. Strano, “Structural behaviour and vibro-acoustic analysis of a composite rail vehicle car body roof,” in *Lecture Notes in Engineering and Computer Science*, 2016, vol. 2224.

[6] M. Grasso *et al.*, “Design of composite sandwich shock absorber mounting for an innovative rail vehicle end,” in *Lecture Notes in Engineering and Computer Science*, 2015, vol. 2218.

[7] M. Grasso *et al.*, “Composite material design for rail vehicle innovative lightweight components,” in *Lecture Notes in Engineering and Computer Science*, 2015, vol. 2218.

[8] M. (Texas I. Raju, “ULP meets energy harvesting: A game-changing combination for design engineers,” *White Pap.*, p. 5, 2008.

[9] “Yole Développement, MEMS, Compound Semiconductors, Advanced Packaging, PV, 3D-IC, LED, Optoelectronics, Power Electronics, Microfluidic, Imaging, CMOS image sensors, CIS, technology market research technology analysis strategy consulting firm - HOME.” [Online]. Available: http://www.yole.fr/index.aspx. [Accessed: 07-Sep-2018].

[10] M. T. Penella and M. Gasulla, “A Review of Commercial Energy Harvesters for Autonomous Sensors,” in *2007 IEEE Instrumentation & Measurement Technology Conference IMTC 2007*, 2007, pp. 1–5.

[11] S. Roundy *et al.*, “Improving power output for vibration-based energy scavengers,” *IEEE Pervasive Computing*, vol. 4, no. 1. pp. 28–36, Jan-2005.

[12] S. R. Anton and H. A. Sodano, “A review of power harvesting using piezoelectric materials (2003-2006),” *Smart Mater. Struct.*, vol. 16, no. 3, 2007.

[13] A. Bilbao, D. Hoover, J. Rice, and J. Chapman, “Ultra-low power wireless sensing for long-term structural health monitoring,” 2011, vol. 7981, p. 798109.

[14] K. A. Cook-Chennault, N. Thambi, and A. M. Sastry, “Powering MEMS portable devices - A review of non-regenerative and regenerative power supply systems with special emphasis on piezoelectric energy harvesting systems,” *Smart Mater. Struct.*, vol. 17, no. 4, 2008.

[15] L. Mateu and F. Moll, “Review of Energy Harvesting Techniques and Applications for Microelectronics,” in *VLSI Circuits and Systems II*, 2005, vol. 5837, pp. 359–373.

[16] A. Harb, “Energy harvesting: State-of-the-art,” *Renew. Energy*, vol. 36, no. 10, pp. 2641–2654, 2011.

[17] J. P. Thomas, M. A. Qidwai, and J. C. Kellogg, “Energy scavenging for small-scale unmanned systems,” *J. Power Sources*, vol. 159, no. 2, pp. 1494–1509, 2006.

[18] W. Guo *et al.*, “Energy Harvesting with Single-Ion-Selective Nanopores: A Concentration-Gradient-Driven Nanofluidic Power Source,” *Adv. Funct. Mater.*, vol. 20, no. 8, pp. 1339–1344, Apr. 2010.

[19] W. Jia, G. Valdés-Ramírez, A. J. Bandodkar, J. R. Windmiller, and J. Wang, “Epidermal biofuel cells: Energy harvesting from human perspiration,” *Angew. Chemie - Int. Ed.*, vol. 52, no. 28, pp. 7233–7236, 2013.

[20] P. M.-Y. Fan, O.-Y. Wong, M.-J. Chung, T.-Y. Su, X. Zhang, and P.-H. Chen, “Energy harvesting techniques: Energy sources, power management and conversion,” in *2015 European Conference on Circuit Theory and Design (ECCTD)*, 2015, pp. 1–4.

[21] X. Tang and L. Zuo, “Towards Meso and Macro Scale Energy Harvesting of Vibration,” *ASME 2009 Int. Mech. Eng. Congr. Expo.*, pp. 885–896, Jan. 2009.

[22] R. Ahmed, F. Mir, and S. Banerjee, “A review on energy harvesting approaches for renewable energies from ambient vibrations and acoustic waves using piezoelectricity,” *Smart Mater. Struct.*, vol. 26, no. 8, p. 085031, 2017.

[23] C. Ó. Mathúna, T. O’Donnell, R. V. Martinez-Catala, J. Rohan, and B. O’Flynn, “Energy scavenging for long-term deployable wireless sensor networks,” *Talanta*, vol. 75, no. 3. pp. 613–623, 2008.

[24] S. Chalasani and J. Conrad, “A survey of energy harvesting sources for embedded systems,” *Southeastcon, 2008. IEEE*, pp. 442–447, 2008.

[25] J. Paradiso and T. Starner, “Human- Generated Power for Mobile Electronics,” in *Low-Power Electronics Design*, C. Piguet, Ed. CRC Press, 2004, pp. 45-1-45–35.

[26] J. A. Paradiso and T. Starner, “Energy scavenging for mobile and wireless electronics,” *IEEE Pervasive Computing*, vol. 4, no. 1. pp. 18–27, 2005.

[27] J. M. Gilbert and F. Balouchi, “Comparison of energy harvesting systems for wireless sensor networks,” *Int. J. Autom. Comput.*, vol. 5, no. 4, pp. 334–347, 2008.

[28] C. Wei and X. Jing, “A comprehensive review on vibration energy harvesting: Modelling and realization,” *Renew. Sustain. Energy Rev.*, vol. 74, no. February, pp. 1–18, 2017.

[29] D. N. Fry, D. E. Holcomb, J. K. Munro, L. C. Oakses, and M. J. Maston, “Compact Portable Electric Power Sources,” Oak Ridge National Laboratory, TN, Feb. 1997.

[30] S. J. Kim, J. H. We, and B. J. Cho, “A wearable thermoelectric generator fabricated on a glass fabric,” *Energy Environ. Sci.*, vol. 7, no. 6, pp. 1959–1965, May 2014.

[31] J. P. Fleurial *et al.*, “Miniaturized Thermoelectric Power Sources,” *34th Intersoc. Energy Convers. Eng. Conf. Proc.*, vol. 992569, 1999.

[32] A. W. Culp, *Principles of energy conversion*. McGraw-Hill, 1991.

[33] A. Cuadras, M. Gasulla, and V. Ferrari, “Thermal energy harvesting through pyroelectricity,” *Sensors Actuators A Phys.*, vol. 158, no. 1, pp. 132–139, Mar. 2010.

[34] V. Raghunathan, A. Kansal, J. Hsu, J. Friedman, and M. B. Srivastava, “Design considerations for solar energy harvesting wireless embedded systems,” in *Information Processing in Sensor Networks, 2005. IPSN 2005. Fourth International Symposium on*, 2005, pp. 457–462.

[35] J. W. Kimball, B. T. Kuhn, R. S. Balog, and J. W. Kimball, “A System Design Approach for Unattended Solar Energy Harvesting Supply,” *IEEE Trans. Power Electron.*, vol. 24, no. 4, pp. 952–962, 2009.

[36] J. M. Gordon and International Solar Energy Society., *Solar energy : the state of the art : ISES position papers*. James & James, 2001.

[37] J. P. Thomas, M. A. Qidwai, and J. C. Kellogg, “Energy scavenging for small-scale unmanned systems,” *J. Power Sources*, vol. 159, no. 2, pp. 1494–1509, Sep. 2006.

[38] L.-G. Tran, H.-K. Cha, and W.-T. Park, “RF power harvesting: a review on designing methodologies and applications,” *Micro Nano Syst. Lett.*, vol. 5, no. 1, p. 14, 2017.

[39] H. Nishimoto, Y. Kawahara, and T. Asami, “Prototype implementation of ambient RF energy harvesting wireless sensor networks,” *2010 IEEE Sensors*, pp. 1282–1287, 2010.

[40] X. Lu, P. Wang, D. Niyato, D. I. Kim, and Z. Han, “Wireless Charging Technologies: Fundamentals, Standards, and Network Applications,” *IEEE Commun. Surv. Tutorials*, vol. 18, no. 2, pp. 1413–1452, 2016.

[41] P. D. Mitcheson, E. M. Yeatman, G. K. Rao, A. S. Holmes, and T. C. Green, “Energy harvesting from human and machine motion for wireless electronic devices,” *Proc. IEEE*, vol. 96, no. 9, pp. 1457–1486, 2008.

[42] N. Manca, “Functional modelling and prototyping of electronic integrated kinetic energy harvesters,” 2017.

[43] D. A. Howey, A. Bansal, and A. S. Holmes, “Design and performance of a centimetre-scale shrouded wind turbine for energy harvesting,” *Smart Mater. Struct.*, vol. 20, no. 8, 2011.

[44] D. Carli, D. Brunelli, D. Bertozzi, and L. Benini, “A high-efficiency wind-flow energy harvester using micro turbine,” in *SPEEDAM 2010 - International Symposium on Power Electronics, Electrical Drives, Automation and Motion*, 2010, pp. 778–783.

[45] S. Roundy, P. K. Wright, and J. Rabaey, “A study of low level vibrations as a power source for wireless sensor nodes,” *Computer Communications*, vol. 26, no. 11. pp. 1131–1144, 2003.

[46] M. E. Bob O’Neil *et al.*, “First Draft of Standard on Vibration Energy Harvesting.” 2007.

[47] T. Ikeda, *Fundamentals of piezoelectricity*. Oxford University Press, 1996.

[48] J. Feenstra, J. Granstrom, and H. Sodano, “Mechanical Systems and Signal Processing

Energy harvesting through a backpack employing a mechanically amplified piezoelectric stack," *Mech. Syst. Signal Process.*, vol. 22, pp. 721–734, 2008.

[49] L. Xie and M. Cai, "Increased energy harvesting and reduced accelerative load for backpacks via frequency tuning," 2015.

[50] E. Bonisoli, M. Repetto, N. Manca, and A. Gasparini, "Electromechanical and Electronic Integrated Harvester for Shoes Application," *IEEE/ASME Trans. Mechatronics*, vol. 22, no. 5, pp. 1921–1932, Oct. 2017.

[51] L. Zuo and P.-S. Zhang, "Energy Harvesting, Ride Comfort, and Road Handling of Regenerative Vehicle Suspensions," *J. Vib. Acoust.*, vol. 135, no. 1, p. 011002, 2013.

[52] S. Tornincasa, M. Repetto, E. Bonisoli, and F. Di Monaco, "Energy harvester for vehicle tires: Nonlinear dynamics and experimental outcomes," *J. Intell. Mater. Syst. Struct.*, vol. 23, no. 1, pp. 3–13, Jan. 2012.

[53] X. Jiang, Y. Li, J. Li, J. Wang, and J. Yao, "Piezoelectric energy harvesting from traffic-induced pavement vibrations," *J. Renew. Sustain. Energy*, vol. 6, no. 4, 2014.

[54] M. R. Pearson, M. J. Eaton, R. Pullin, C. A. Featherston, and K. M. Holford, "Energy harvesting for aerospace structural health monitoring systems," in *Journal of Physics: Conference Series*, 2012, vol. 382, no. 1.

[55] "Kinetron - Smart Micro Energy Harvesting Systems." [Online]. Available: https://www.kinetron.eu/. [Accessed: 06-Sep-2018].

[56] "perpetuum." [Online]. Available: https://perpetuum.com/. [Accessed: 06-Sep-2018].

[57] "Ferro Solutions." [Online]. Available: http://www.ferrosi.com/. [Accessed: 06-Sep-2018].

[58] J. C. Samin, · O Brüls, · J F Collard, · L Sass, and · P Fisette, "Multiphysics modeling and optimization of mechatronic multibody systems," *Multibody Syst Dyn*, vol. 18, pp. 345–373, 2007.

[59] N. Docquier, "Multiphysics Modelling of Multibody Systems : Application to Railway Pneumatic Suspensions," 2010.

[60] "EU Regulation No 851/2006." 2006.

[61] S. Bruni, R. Goodall, T. X. Mei, and H. Tsunashima, "Control and monitoring for railway vehicle dynamics," *Veh. Syst. Dyn.*, vol. 45, no. 7–8, pp. 743–779, 2007.

[62] C. Roberts and R. M. Goodall, "Strategies and techniques for safety and performance monitoring on railways," *IFAC Proc. Vol.*, vol. 42, no. 8, pp. 746–755, 2009.

[63] R. W. Ngigi, C. Pislaru, A. Ball, and F. Gu, "Modern techniques for condition monitoring of railway vehicle dynamics," *J. Phys. Conf. Ser.*, vol. 364, no. 1, 2012.

[64] C. P. Ward *et al.*, "Condition Monitoring Opportunities Using Vehicle-Based Sensors," *Proc. Inst. Mech. Eng. Part F J. Rail Rapid Transit*, vol. 225, no. 2, pp. 202–218, Mar. 2011.

[65] G. Gatti, M. J. Brennan, M. G. Tehrani, and D. J. Thompson, "Harvesting energy from the vibration of a passing train using a single-degree-of-freedom oscillator," *Mech. Syst. Signal Process.*, vol. 66–67, pp. 785–792, 2016.

[66] Y. Tianchen, Y. Jian, S. Ruigang, and L. Xiaowei, "Vibration energy harvesting system for

railroad safety based on running vehicles," *Smart Mater. Struct.*, vol. 23, no. 12, p. 125046, Dec. 2014.

[67] J. J. Wang, G. P. Penamalli, and L. Zuo, "Electromagnetic energy harvesting from train induced railway track vibrations," in *Proceedings of 2012 IEEE/ASME 8th IEEE/ASME International Conference on Mechatronic and Embedded Systems and Applications*, 2012, pp. 29–34.

[68] C. A. Nelson, S. R. Platt, D. Albrecht, V. Kamarajugadda, and M. Fateh, "Power harvesting for railroad track health monitoring using piezoelectric and inductive devices," 2008, vol. 6928, p. 69280R.

[69] M. Gao, J. Lu, Y. Wang, P. Wang, and L. Wang, "Smart monitoring of underground railway by local energy generation," *Undergr. Sp.*, vol. 2, no. 4, pp. 210–219, Dec. 2017.

[70] D. Socie and C. Barkan, "High-Speed Rail IDEA Program Smart Sensor System for Monitoring Railcar Braking Systems Final Report for High-Speed Rail IDEA Project 51," 2008.

[71] G. De Pasquale, A. Somà, and F. Fraccarollo, "Piezoelectric energy harvesting for autonomous sensors network on safety-improved railway vehicles," *Proc. Inst. Mech. Eng. Part C J. Mech. Eng. Sci.*, vol. 226, no. 4, pp. 1107–1117, Apr. 2012.

[72] G. De Pasquale, A. Somà, and N. Zampieri, "Design, Simulation, and Testing of Energy Harvesters With Magnetic Suspensions for the Generation of Electricity From Freight Train Vibrations," *J. Comput. Nonlinear Dyn.*, vol. 7, no. 4, p. 041011, Oct. 2012.

[73] S. Bradai, S. Naifar, C. Viehweger, and O. Kanoun, "Electromagnetic Vibration Energy Harvesting for Railway Applications."

[74] S. Iwnicki, Ed., *Handbook of Railway Vehicle Dynamics*. CRC Press, 2006.

[75] A. C. Zolotas and R. M. Goodall, "Modelling and control of railway vehicle suspensions," in *Lecture Notes in Control and Information Sciences*, 2007, vol. 367, pp. 373–411.

[76] J. Zhou, R. Goodall, L. Ren, and H. Zhang, "Influences of car body vertical flexibility on ride quality of passenger railway vehicles," *Proc. Inst. Mech. Eng. Part F J. Rail Rapid Transit*, vol. 223, no. 5, pp. 461–471, 2009.

[77] D. Gong, J. S. Zhou, and W. J. Sun, "On the resonant vibration of a flexible railway car body and its suppression with a dynamic vibration absorber," *JVC/Journal Vib. Control*, vol. 19, no. 5, pp. 649–657, 2013.

[78] W. Zhai, P. Liu, J. Lin, and K. Wang, "Experimental investigation on vibration behavior of a CRH train at speed of 350 km/h," *Int. J. Rail Transp.*, vol. 3, no. 1, pp. 1–16, 2015.

[79] F. Cheli and R. Corradi, "On rail vehicle vibrations induced by track unevenness: Analysis of the excitation mechanism," *J. Sound Vib.*, vol. 330, pp. 3744–3765, 2011.

[80] M. Dumitriu, "Analysis of the Dynamic Response in the Railway Vehicles to the Track Vertical Irregularities. Part I: The Theoretical Model and the Vehicle Response Functions," *J. Eng. Sci. Technol. Rev.*, vol. 8, no. 4, pp. 24–31, 2015.

[81] T.-C. I. Aravanis, J. S. Sakellariou, and S. D. Fassois, "Railway Vertical Random Vibration Analysis Under Normal Operating Conditions," in *23rd International Congress on Sound*

and Vibration (ICSV23), 2016, pp. 1–8.

[82] D. Gong, W. Sun, J. Zhou, and X. Xiea, “Analysis on the Vertical Coupled Vibration between Bogies and Metro Car Body,” *Procedia Eng.*, vol. 16, pp. 825–831, 2011.

[83] M. Dumitriu, “Analysis of the dynamic response in the railway vehicles to the track vertical irregularities. Part II: The numerical analysis,” *J. Eng. Sci. Technol. Rev.*, vol. 8, no. 4, pp. 32–39, 2015.

[84] A. R. Guido and L. Della Pietra, *Lezioni di meccanica delle macchine vol.1*. CUEN, 1999.

[85] V. K. Garg and R. V. Dukkipati, *Dynamics of railway vehicle systems*. Academic Press, 1984.

[86] S. Bruni, J. Vinolas, M. Berg, O. Polach, and S. Stichel, “Modelling of suspension components in a rail vehicle dynamics context,” in *Vehicle System Dynamics*, 2011, vol. 49, no. 7, pp. 1021–1072.

[87] T. Nakajima, Y. Shimokawa, M. Mizuno, and H. Sugiyama, “Air Suspension System Model Coupled With Leveling and Differential Pressure Valves for Railroad Vehicle Dynamics Simulation,” *J. Comput. Nonlinear Dyn.*, vol. 9, no. 3, p. 031006, Feb. 2014.

[88] A. Facchinetti, L. Mazzola, S. Alfi, and S. Bruni, “Vehicle System Dynamics Mathematical modelling of the secondary airspring suspension in railway vehicles and its effect on safety and ride comfort Mathematical modelling of the secondary airspring suspension in railway vehicles and its effect on safety and ride comfort,” *Veh. Syst. Dyn.*, vol. 48, pp. 429–449, 2010.

[89] N. ODA and S. NISHIMURA, “Vibration of Air Suspension Bogies and Their Design,” *Bull. JSME*, vol. 13, no. 55, pp. 43–50, 1970.

[90] M. Berg, “A THREE-DIMENSIONAL AIRSPRING MODEL WITH FRICTION AND ORIFICE DAMPING,” 2000.

[91] G. Quaglia and M. Sorli, “Air Suspension Dimensionless Analysis and Design Procedure,” *Veh. Syst. Dyn.*, vol. 35, no. 6, pp. 443–475, 2001.

[92] N. Docquier, P. Fisette, and H. Jeanmart, “Multiphysic modelling of railway vehicles equipped with pneumatic suspensions,” *User Model. User-adapt. Interact.*, vol. 45, no. 6, pp. 505–524, 2007.

[93] N. Docquier, P. Fisette, and H. Jeanmart, “Model-based evaluation of railway pneumatic suspensions,” in *Vehicle System Dynamics*, 2008, vol. 46, no. SUPPL.1, pp. 481–493.

[94] A. J. Nieto, A. L. Morales, A. Gonzaíez, J. M. Chicharro, and P. Pintado, “An analytical model of pneumatic suspensions based on an experimental characterization,” *J. Sound Vib.*, vol. 313, pp. 290–307, 2008.

[95] Zhu Sihong, Wang Jiasheng, and Zhang Ying, “Research on theoretical calculation model for dynamic stiffness of air spring with auxiliary chamber,” in *2008 IEEE Vehicle Power and Propulsion Conference*, 2008, pp. 1–6.

[96] C. Erin, B. Wilson, and J. Zapfe, “AN IMPROVED MODEL OF A PNEUMATIC VIBRATION ISOLATOR: THEORY AND EXPERIMENT,” *J. Sound Vib.*, vol. 218, no. 1, pp. 81–101, Nov. 1998.

[97] J.-H. Lee and K.-J. Kim, “Modeling of nonlinear complex stiffness of dual-chamber

pneumatic spring for precision vibration isolations," *J. Sound Vib.*, vol. 301, no. 3–5, pp. 909–926, Apr. 2007.

[98] ISO, "Pneumatic fluid power -- Determination of flow-rate characteristics of components using compressible fluids -- Part 3: Method for calculating steady-state flow-rate characteristics of systems," 2014.

[99] D. J. Erturk, A.; Inman, *Piezoelectric energy harvesting*. John Wiley and Sons, 2011.

[100] H. Vocca and F. Cottone, "Kinetic Energy Harvesting," in *ICT - Energy - Concepts Towards Zero - Power Information and Communication Technology*, InTech, 2014.

[101] C. B. Williams and R. B. Yates, "Analysis of a micro-electric generator for microsystems," *Sensors Actuators A Phys.*, vol. 52, no. 1–3, pp. 8–11, Mar. 1996.

[102] S. Timoshenko and S. Woinowsky-Krieger, *Theory of plates and shells*. McGraw-Hill, 1959.

[103] N. G. Stephen, "On energy harvesting from ambient vibration," *J. Sound Vib.*, vol. 293, no. 1–2, pp. 409–425, May 2006.

[104] B. Jaffe, W. R. Cook, and H. Jaffe, *Piezoelectric ceramics.*, vol. 3. Academic Press, 1971.

[105] IEEE, "IEEE Standard on Piezoelectricity," *ANSI/IEEE Std 176-1987*. p. 0_1, 1988.

[106] T. Hehn and Y. Manoli, "Piezoelectricity and Energy Harvester Modelling," Springer, Dordrecht, 2015, pp. 21–40.

[107] M. Renaud, K. Karakaya, T. Sterken, P. Fiorini, C. Van Hoof, and R. Puers, "Fabrication, modelling and characterization of MEMS piezoelectric vibration harvesters," *Sensors Actuators A*, pp. 380–386, 2008.

[108] E. Arroyo and A. Badel, "Electromagnetic vibration energy harvesting device optimization by synchronous energy extraction," *Sensors Actuators A. Phys.*, vol. 171, pp. 266–273, 2011.

[109] P. D. Mitcheson and T. T. Toh, "Power Management Electronics," in *Energy Harvesting for Autonomous Systems*, 2010, pp. 1–58.

[110] P. D. Mitcheson, E. K. Reilly, T. Toh, P. K. Wright, and E. M. Yeatman, "Performance limits of the three MEMS inertial energy generator transduction types," in *Journal of Micromechanics and Microengineering*, 2007, vol. 17, no. 9, pp. 211–216.

[111] "Piezo Ceramic Technology, Piezo Actuators & Piezo Components from PI Ceramic." [Online]. Available: https://www.piceramic.com/en/. [Accessed: 31-Oct-2018].

[112] S. Pagano, M. Russo, S. Strano, and M. Terzo, "A mixed approach for the control of a testing equipment employed for earthquake isolation systems," *Proc. Inst. Mech. Eng. Part C J. Mech. Eng. Sci.*, vol. 228, no. 2, pp. 246–261, Feb. 2014.

[113] S. Strano and M. Terzo, "A multi-purpose seismic test rig control via a sliding mode approach," *Struct. Control Heal. Monit.*, vol. 21, no. 8, pp. 1193–1207, Aug. 2014.

Appendix A

An in-house made instrument for non-disruptive viscoelastic characterisation: V-ELA

The development of V-ELA started during this PhD work at the laboratory of the DII (Industrial Engineering Department), at the University of Naples “Federico II”. This instrument has the main aim in determination of materials viscoelastic properties, especially for tyre application.

The most important innovation that this instrument wants to introduce is the possibility to characterise the rubber compound thanks to non-disruptive tests, therefore using it directly on the tyre. It is proposed as an alternative way to dynamic mechanical analysis (DMA) to get viscoelastic moduli. The DMA is the common procedure used for rubber characterization: a small deformation is applied to a sample in a cyclic manner. This allows the materials response to stress, temperature, frequency and other values to be studied. The limitation of the DMA test can be related to the fact that it can give a very reliable picture of the compound behaviour (at different temperatures and frequencies) by analysing a rubber block: DMA works by applying a sinusoidal deformation to a sample of known geometry.

Therefore, a different kind of test, based on indentation approach, has been considered and the first prototype of the portable instrument has been carried out, to give the opportunity to evaluate tyre tread conditions and try to get out closer results directly during test sessions at proving ground.

V-ELA operational principle is based on the indentation test. It is one of the most widely used techniques for measuring the mechanical properties of a material. The instrumented indentation test is based upon successively recording the loading force and the penetration depth throughout the entire process of the testing period.

The instrument consists of a fixed part, connected to the ground/sample (the external cylinder), and of a moving part. The moving part allows the measurement of the force and displacement by means of a load cell and a LVDT transducer. An analogue-digital card for data acquisition completes the instrument layout.

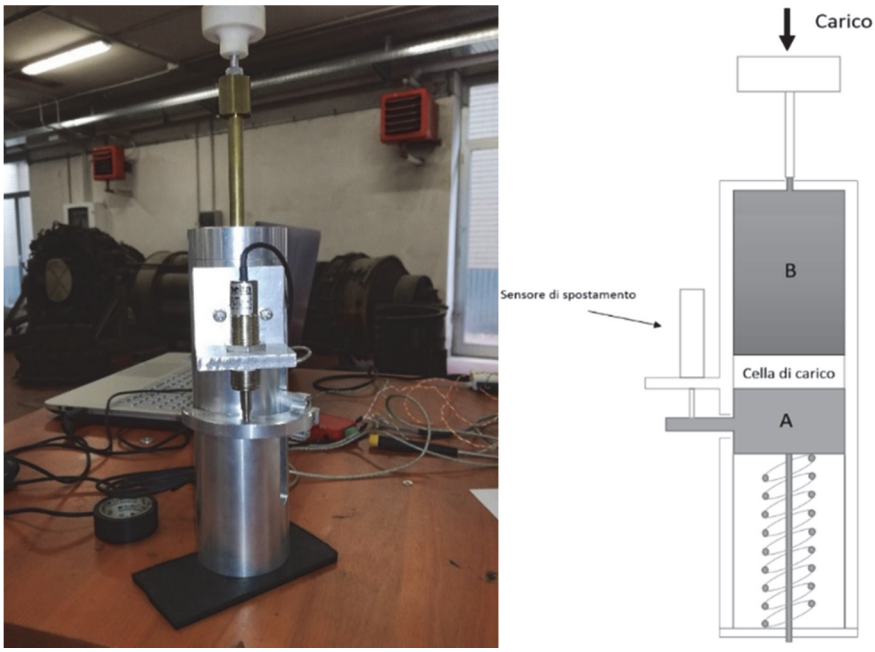

Figure A.0.1 V-ELA instrument

The instrument is composed by following main component:

Loading rod. The component transmits the force to the sample. The rod can penetrate the sample, moving from the cylinder through a hole.

Booster Spring. Allows the ascent of the cylinder A.

Cylinder A. It allows the transmission of the force coming from the reaction of the sample on the load cell. At the same time, it allows to measure the deformation of the sample.

Cylinder B. It is bound to the upper piston, from which it receives the forcing, and deals with the transmission of the latter to the load cell, from which it will then come through the cylinder A to the sample.

Load cell. It is the transducer used to measure the force applied.

LVDT Transducer. An Inductive displacement transducer is the device used to measure the loading road displacement.